

AD A 123497



①

~~77-1023~~

COMBUSTION OF A LIQUID METAL FROM A WICK

Technical Report

Sponsored by

Advanced Research Projects Agency
ARPA Order No. 2150
Program Code No. 2N10
Contract No. N00600-74-C-0033

Prepared by

T. R. Blakeslee III and G. M. Faeth

The Pennsylvania State University
College of Engineering
Department of Mechanical Engineering
University Park, Pennsylvania

May 1977

FILE COPY

JAN 18 1983

UNCLASSIFIED

SECURITY CLASSIFICATION OF THIS PAGE (When Data Entered)

REPORT DOCUMENTATION PAGE		READ INSTRUCTIONS BEFORE COMPLETING FORM
1. REPORT NUMBER	2. GOVT ACCESSION NO.	3. RECIPIENT'S CATALOG NUMBER
	AD-A123497	
4. TITLE (and Subtitle)		5. TYPE OF REPORT & PERIOD COVERED
Combustion of a Liquid Metal from a Wick		Interim Sept. 73 to Feb. 77
		6. PERFORMING ORG. REPORT NUMBER
7. AUTHOR(s)		8. CONTRACT OR GRANT NUMBER(s)
T. R. Blakeslee III Gerard M. Faeth		N00600-74-C-0033
9. PERFORMING ORGANIZATION NAME AND ADDRESS		10. PROGRAM ELEMENT, PROJECT, TASK AREA & WORK UNIT NUMBERS
Department of Mechanical Engineering The Pennsylvania State University University Park, Penna. 16802		62105E, 2N10 Other DOD-ARPA, 274-510-50
11. CONTROLLING OFFICE NAME AND ADDRESS		12. REPORT DATE
Defense Advanced Research Projects Agency 1400 Wilson Blvd., Arlington, Va. 22209		May, 1977
		13. NUMBER OF PAGES
		137
14. MONITORING AGENCY NAME & ADDRESS (if different from Controlling Office)		15. SECURITY CLASS. (of this report)
David W. Taylor Naval Ship R&D Center Annapolis, Maryland 21402		U
		15a. DECLASSIFICATION/DOWNGRADING SCHEDULE
16. DISTRIBUTION STATEMENT (of this Report)		
Approved for Public Release; distribution unlimited.		
17. DISTRIBUTION STATEMENT (of the abstract entered in Block 20, if different from Report)		
18. SUPPLEMENTARY NOTES		
A Ph.D. Thesis in Mechanical Engineering, directed by Gerard M. Faeth		
19. KEY WORDS (Continue on reverse side if necessary and identify by block number)		
Liquid Metal Combustor; Liquid Metal Reactor		
20. ABSTRACT (Continue on reverse side if necessary and identify by block number)		
Over		

DD FORM 1473

1 JAN 73

EDITION OF 1 NOV 65 IS OBSOLETE
S/N 0102-014-6601

Unclassified

SECURITY CLASSIFICATION OF THIS PAGE (When Data Entered)

UNCLASSIFIED

SECURITY CLASSIFICATION OF THIS PAGE (When Data Entered)

ABSTRACT: An experimental and analytical study of laminar, free-convective combustion of a liquid metal from a wick was performed, using lithium and sulfur hexafluoride as the reactant combination. Observations of the combustion process indicate a vapor-phase reaction with products condensing on the fuel surface and in the vapor phase, but not in the flame. Data were obtained for the lithium burning rate in sulfur hexafluoride as a function of: wick length, ambient pressure, and concentration of inert diluent in the ambient gas. Data were also obtained for the relationship between wick surface temperature and ambient pressure. Two theoretical models using a film-theory approximation were developed. The effect of natural convection shown by the variation of burning rate with wick length is well described by the approach developed by Spalding. The no-condensation model, which neglects condensation, predicts a weaker dependence of burning rate on pressure than exhibited by the data; however, the effect of the inert diluent in the ambient gas is predicted quite well, indicating an effect on the condensation process by the presence of the noncondensable gas. The condensation-front model, which allows condensation of the products at two fronts within the boundary layer, predicts a stronger dependence of burning rate on pressure than the no-condensation model, yet still weaker than seen in the data. The experimentally-observed flame position is predicted reasonably well.

Accession For	
DTIC GRA&I	<input checked="" type="checkbox"/>
DTIC T B	<input type="checkbox"/>
Unannounced	<input type="checkbox"/>
Justification	
By	
Distribution/	
Availability Codes	
Availability/or	
Dist	Special
A	

DTIC
COPY
INSPECTED
2

UNCLASSIFIED

SECURITY CLASSIFICATION OF THIS PAGE (When Data Entered)

COMBUSTION OF A LIQUID METAL FROM A WICK

Technical Report

May 1977

Sponsored by
Advanced Research Projects Agency
ARPA Order No. 2150
Program Code No. 2N10
Contract No. N00600-74-C-0033

The views and conclusions contained in this document are those of the authors and should not be interpreted as necessarily representing the official policies, either expressed or implied, of the Advanced Research Projects Agency of the U. S. Government.

Prepared by

T. R. Blakeslee III
G. M. Faeth; Telephone (814) 865-3743

Mechanical Engineering Department
The Pennsylvania State University
University Park, Pennsylvania 16802

ACKNOWLEDGMENT

This research was supported by David W. Taylor Naval Ship Research and Development Center, Annapolis Laboratory, as Technical Agent for Defense Advanced Research Projects Agency, under contract number NO0600-74-C-0033.

TABLE OF CONTENTS

	<u>Page</u>
ACKNOWLEDGMENTS	11
LIST OF TABLES	vi
LIST OF FIGURES	vii
NOMENCLATURE	x
ABSTRACT	xii
I. INTRODUCTION	1
1.1 General Statement of the Problem	1
1.2 Previous Related Studies	5
1.3 Specific Statement of the Problem	10
II. APPARATUS AND PROCEDURE FOR OBSERVATION OF LITHIUM COMBUSTION AND BURNING RATES	12
2.1 Preliminary Tests--Combustion of Lithium Droplets	12
2.1.1 Apparatus	12
2.1.2 Procedure	14
2.2 Lithium Burning Rate Tests	15
2.2.1 Test Sample	15
2.2.2 Vacuum Chamber	17
2.2.3 Gas Supply System	21
2.2.4 Instrumentation	23
2.2.5 Reactants	23
2.2.6 Procedure	24
2.2.6.1 Preparation of Test Samples	24
2.2.6.2 Test Procedure	25
III. RESULTS OF LITHIUM COMBUSTION AND BURNING RATE TESTS	28
3.1 Observation of the Lithium Combustion Process	28
3.2 Lithium Burning Rates in Sulfur Hexafluoride	39
3.3 Lithium Burning Rates in Argon-Sulfur Hexafluoride Mixtures	41
IV. APPARATUS AND PROCEDURE FOR WICK-TYPE COMBUSTOR TESTS	45

TABLE OF CONTENTS (CONTINUED)

	<u>Page</u>
4.1 Apparatus.	45
4.1.1 Wick-Type Combustor	45
4.1.2 Gas Supply System	52
4.1.3 Instrumentation	54
4.1.3.1 Flow Measurement	54
4.1.3.2 Temperature Measurement.	54
4.1.3.3 Pressure Measurement	55
4.1.4 Reactants	55
4.2 Procedure.	56
4.2.1 Combustor Preparation	56
4.2.2 Test Procedure.	57
4.2.3 Post-Test Procedure	58
V. RESULTS OF THE WICK-TYPE COMBUSTOR TESTS.	60
VI. THEORETICAL CONSIDERATIONS.	70
6.1 Introduction	70
6.2 No-Condensation Model.	77
6.2.1 Description and Assumptions	77
6.2.2 Analysis.	80
6.2.3 Results	82
6.3 Condensation-Front Model	91
6.3.1 Description and Assumptions	91
6.3.2 Analysis.	95
6.3.3 Results	101
6.4 Discussion and Comparison of Theoretical Models.	103
VII. SUMMARY AND CONCLUSIONS	117
7.1 Summary.	117
7.2 Conclusions.	119
7.3 Recommendations for Further Study.	120
REFERENCES	121
APPENDIX A: DETERMINATION OF UNBURNED LITHIUM FOR LITHIUM BURNING RATE TESTS.	126

TABLE OF CONTENTS (CONTINUED)

	<u>Page</u>
APPENDIX B: EXPERIMENTAL DATA FROM LITHIUM BURNING RATE TESTS.	130
APPENDIX C: SUMMARY OF DATA OBTAINED DURING WICK-TYPE COMBUSTOR TESTS	133

LIST OF TABLES

<u>Table</u>	<u>Title</u>	<u>Page</u>
1	Summary of Surface Area Covered by Product.	34
2	Design Summary of Preliminary Wick-Type Combustor . .	49
3	Design Summary of Long Length-to-Diameter Wick-Type Combustor.	50
4	Design Summary of Large Wick-Type Combustor	51
5	Comparison of Predicted Vapor Pressure of Delimiting Conditions at Wick Surface.	65
6	Adiabatic Flame Temperature of Lithium-Sulfur Hexafluoride Combustion	74
7	Effect of Wick Temperature on Wick Conditions at a Total Pressure of 13300 Pa.	88
8	Comparison of Temperatures Predicted by Groff with Data Obtained from the Wick-Type Combustor Test . .	115
9	Summary of Lithium Burning Rate Tests in Sulfur Hexafluoride.	130
10	Summary of Lithium Burning Rate Tests in Argon-Sulfur Hexafluoride Mixtures at a Constant Total Pressure of 13300 Pa.	132

LIST OF FIGURES

<u>Figure</u>	<u>Caption</u>	<u>Page</u>
1	Wick-Type Combustor.	4
2	Schematic of Apparatus for Observation of Lithium Droplet Combustion	13
3	Schematic of Test Sample for Lithium Burning Rate Tests	16
4	Vacuum Chamber	18
5	Schematic of Apparatus to Determine Lithium- Sulfur Hexafluoride Burning Rates.	19
6	Photograph of the Test Apparatus Inside Vacuum Chamber.	20
7	Gas Supply System for Lithium Burning Rate Tests .	22
8	Combustion of a Lithium Droplet in Sulfur Hexafluoride	29
9	Product Accumulation on Support Rod After Combustion of Lithium Droplet in Sulfur Hexafluoride	30
10	Combustion of Lithium from a Wick in Sulfur Hexafluoride	32
11	Combustion of Lithium from a Wick in Argon- Sulfur Hexafluoride Mixtures	33
12	Flame Stand-Off Distance for Combustion of Lithium from a Wick in Sulfur Hexafluoride	37
13	Luminous Zone Thickness for Combustion of Lithium from a Wick in Sulfur Hexafluoride	38
14	Effect of Pressure on Lithium Burning Rate in Sulfur Hexafluoride for a Constant Wick Length (30 mm).	40
15	Effect of Wick Length on Lithium Burning Rate in Sulfur Hexafluoride for a Constant Pressure (10750 Pa)	42
16	Effect of Argon Mass Fraction on Burning Rate at a Constant Pressure of 13300 Pa.	44

LIST OF FIGURES (CONTINUED)

<u>Figure</u>	<u>Caption</u>	<u>Page</u>
17	Schematic of Preliminary Wick-Type Combustor . . .	46
18	Schematic of Long Length-to-Diameter Wick-Type Combustor.	47
19	Schematic of Large Wick-Type Combustor	48
20	Schematic of Gas Supply System for Wick-Type Combustor Tests.	53
21	Data from Typical Wick-Type Combustor Test	61
22	Combustor Pressure Versus Wick Surface Temperature.	
23	Schematic of Possible Flame Structures for Lithium-Sulfur Hexafluoride Combustion	
24	Schematic Diagram of No-Condensation Model	78
25	Prediction of the No-Condensation Model for the Effect of Pressure on the Lithium Burning Rate in Sulfur Hexafluoride for a Constant Wick Length (30 mm)	84
26	Prediction of the No-Condensation Model for the Effect of Wick Length on the Lithium Burning Rate in Sulfur Hexafluoride for a Constant Pressure (10750 Pa).	85
27	Measured Wall Temperature as a Function of Mass Fraction of Ambient Argon at a Constant Total Pressure (13300 Pa).	87
28	Prediction of the No-Condensation Model for the Effect of Ambient Argon Concentration on the Lithium Burning Rate in Sulfur Hexafluoride for Constant Wick Length (30 mm) and Constant Total Pressure (13300 Pa).	90
29	Schematic Diagram of Condensation-Front Model. . .	92
30	Schematic Diagram of the Tangency Condition at the Outer Condensation Front	94
31	Vapor Pressure of Stoichiometric Products of Lithium-Sulfur Hexafluoride Combustion	100

LIST OF FIGURES (CONTINUED)

<u>Figure</u>	<u>Caption</u>	<u>Page</u>
32	Prediction of the Condensation-Front Model for the Effect of Pressure on the Lithium Burning Rate in Sulfur Hexafluoride for a Constant Wick Length (30 mm)	102
33	Temperature and Concentration Profiles in the No-Condensation Model at 8000 Pa	105
34	Temperature and Concentration Profiles in the Condensation-Front Model at 8000 Pa.	106
35	Prediction of the No-Condensation Model for the Effect of Noncondensable Contaminants Using Experimental Data to Specify Wick Conditions . . .	114

NOMENCLATURE

C	Specific Heat (J/kg-K)
D	Coefficient of Diffusion (m^2/s)
G	Mass Flux ($\text{kg}/\text{m}^2\text{s}$)
g	Gravitational Acceleration (m/s^2)
Gr	Grashof Number
L	Wick Length (m)
P	Pressure (Pa)
PR	Prandtl Number
q''	Heat Flux (W/m^2)
r	Stoichiometric Mass Ratio (kg ox/kg metal)
T	Temperature (K)
V	Molar Volume ($\text{cm}^3/\text{gm-mole}$)
X	Mole Fraction
x	Vertical Distance Along Wick Surface as Measured from Bottom Edge (m)
Y	Mass Fraction
y	Co-ordinate Perpendicular to Fuel Surface (m)
δ	Specific Values of y Co-ordinate (m)
λ	Thermal Conductivity ($\text{W}/\text{m-K}$)
ν	Kinematic Viscosity (m^2/s)
ρ	Mass Density (kg/m^3)
$\sigma, \epsilon/K$	Lennard-Jones Parameters

Subscripts

a	Argon
af	Adiabatic Flame
b	Boiling Point

NOMENCLATURE (CONTINUED)

CF	Condensation-Front Model
e	Boundary Layer Edge
eq	Equilibrium
f	Flame
i	Inner Condensation Front
lum	Luminous Zone
k	Species k
NC	No-Condensation Model
m	Metal
o	Outer Condensation Front
ox	Oxidizer
p	Product
sat	Saturated Vapor
w	Wick Surface
y	In the y-direction
1,2	Regions 1 and 2
1a, 1b, 2a, 2b	Regions 1a, 1b, 2a, and 2b

Superscript

o	Unenhanced Vaporization
---	-------------------------

CHAPTER I

INTRODUCTION

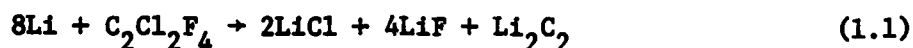
1.1 General Statement of the Problem

Increased activity in oceanographic study has resulted in a surge of interest in power systems that are independent of their environment. A completely closed power system, independent of the ambient sea pressure and having a constant buoyancy, has significant advantages for submersible vehicle applications. Power systems that use hydrocarbon fuels have several disadvantages associated with their gaseous products of combustion. The standard procedure for dealing with the combustion products is to exhaust them overboard. For a submersible vehicle this requires either operating the combustion chamber at the ambient sea pressure or compressing the product gases to the ambient sea pressure before they are exhausted (1); either approach involves increased complexity, volume, and weight for the power system.

One proposal to overcome this problem is the liquid metal combustor, since the products of combustion are condensable. The combustion products of liquid metals reacted with halogenated gases (typical oxidizer choices) are salts, usually in the liquid or solid state, depending on the temperature range of the combustor. The volume of the salts produced by the reaction must be approximately the same as the volume occupied by the liquid fuel in the combustor if the fuel-oxidizer combination is to be usable. Since the products can be stored in the same volume previously occupied by the fuel, this

eliminates the problem of product disposal while underwater. In addition, liquid metal combustors have a very high energy density, allowing a compact design for the thermal energy source.

Several fuel-oxidizer combinations that have products with less volume than the fuel have been tested as heat sources for thermodynamic power cycles, such as the Stirling engine (1-5). Some early work involved combustion of lithium with Freon-114* (3), with a stoichiometric equation:



Recent work, however, has concentrated on the reaction of lithium with sulfur hexafluoride (4-6), with a stoichiometric equation:



Using such criteria as energy density, cost, toxicity, and materials compatibility, van der Sluijs has shown that the lithium-sulfur hexafluoride combustion system is the best choice for a submersible vehicle (4).

In order to provide strength and durability, liquid metal combustors are usually fabricated from stainless steel or nickel superalloys. The temperatures normally encountered in a liquid metal combustor (above 1100 K) are in the range where these materials would be rapidly attacked by the oxidizer (7). Several techniques are presently employed to overcome this problem: (a) inject the oxidizer

*Registered Trademark, E. I. duPont de Nemours and Company.

below the surface of the liquid metal bath; (b) maintain combustor temperatures sufficiently low to preclude corrosion; (c) protect the combustor walls with a coating of fuel. When the oxidizer is injected below the bath surface level, reaction rates are large enough so that no oxidizer leaves the bath and contacts the combustor body (8). Running at low combustor temperatures eliminates the corrosion problem, but other difficulties are encountered, such as unstable ignition and irregular injector performance (6, 8). Covering the combustor walls with a coating of fuel prevents the oxidizer from coming into direct contact with the heated walls. The simplest, and most effective means of coating the walls is to line the inside of the combustor with a wick.

A simple configuration of a wick-type combustor can be seen in Figure 1. A supply of fuel is melted into the bottom of the combustor, and the temperature is raised until the fuel wets the wick by capillary action (about 1100 K for lithium). The oxidizer is introduced into the gas phase and the reaction proceeds as the lithium evaporates from the wick. The fuel supply to the wick is maintained by the capillary pumping of the wick structure. The combustion products condense and settle to the bottom of the fuel reservoir.

The combustion process of the submerged oxidizer jet, used in most of the liquid metal combustors to date, is fairly well defined (9, 10). However, as noted earlier, in a wick-type combustor the oxidizer is injected above the liquid surface. The result is a combustion phenomenon that may include any, or all, of the following: condensation of products; diffusion and convection of fuel, products,

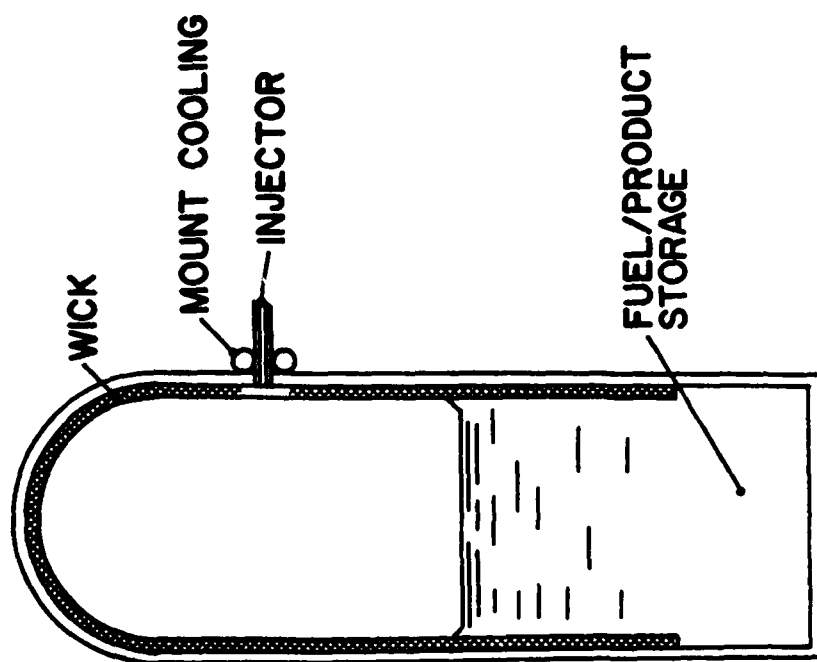


Figure 1 Wick-Type Combustor

and oxidizer; dissolution of products in the fuel; and non-dilute mixtures of fuel, products, and oxidizer. In addition, natural convection must also be considered because of the relatively quiescent nature of the gas phase.

The details of the wick combustion process are not well understood at this time. Therefore, rational design procedures for wick-type combustors are not available and present designs are obtained by trial and error. The over-all objective of the present investigation is to improve the understanding of the process and develop a theoretical model capable of predicting wick combustion characteristics for liquid metals in contact with halogenated gases.

1.2 Previous Related Studies

A search of the literature revealed few studies involving condensable combustion products in a laminar free-convective flow. The previous work can be divided into three general categories: film-theory models of enhanced vaporization from plane surfaces; film-theory models of droplet (or particle) combustion; and experimental studies.

Turkdogan, Grieveson, and Darken (11) investigated the problem of a metal film evaporating into an isothermal environment of an inert gas. They were able to show that the introduction of small amounts of oxidizer into the environment could increase the vaporization rate of the metal to values approaching the theoretical maximum in vacuo. Turkdogan, et al., (11) developed a simple theory based only on diffusion processes to predict this behavior. The important assumptions made for the analysis were: (a) the metal vapor and the oxidizer reacted according to a diffusion flame mechanism; (b) the

reaction products condensed entirely, and immediately, in the flame upon their formation; (c) the existence of the condensed products did not affect the reaction mechanism; (d) the thickness of the concentration boundary layer was equal to the aerodynamic boundary layer of the ambient gas; (e) all flow parallel to the surface of the fuel was neglected; (f) the partial pressures of both the oxidizer and the metal vapor were small compared to the inert gas; (g) mass transport of the metal vapor and the oxidizer was sufficiently slow to neglect the bulk flow induced by diffusion (i.e., mass convection); (h) and the heat release caused by the chemical reaction and condensation at the flame did not affect the temperature profile, which was assumed to be constant throughout the boundary layer. The important conclusion reached from this study was that reaction within the concentration boundary serves to steepen the concentration gradients and, hence, "enhance" the vaporization rate of a metal from a surface.

Rosner (12) extended the film model to the case of non-dilute oxidizer and metal vapor concentrations, analyzing the problem of a one-step, metal-oxidizer reaction in a thin diffusion flame in the presence of an inert gas. The model included both diffusion and the bulk flow induced by diffusion (convection) of the metal and oxidizer toward the flame. Except for the non-dilute mixtures and the inclusion of diffusion-induced mass transfer, Rosner's assumptions were the same as made by Turkdogan, et al. As a consequence of assuming that all the product condensed in the flame, Rosner neglected the presence of any condensed product at all other points. While Rosner does not solve the energy equation, the assumed behavior of the

products limits his model to cases where the flame temperature is not greater than the boiling point of the combustion products. A second major drawback of the Rosner model is that it predicts an infinite burning rate for the case of pure ambient oxidizer.

The problem of droplet combustion has received somewhat more theoretical attention than the film-theory model. Brzustowski and Glassman (13) analyzed the combustion of magnesium and aluminum droplets in oxygen-inert gas environments. The model included heat transfer away from the flame by radiation and conduction to both the droplet and the environment. Convective mass transport of the gases was neglected and the diffusive fluxes were limited to the flow of oxidizer and fuel toward the flame and the flow of vaporized product from the flame to the environment. The condensed product produced in the flame was assumed to be convected outward with the bulk motion in the outer region. No product was assumed to flow toward the droplet. From known thermodynamic behavior of metal-oxygen reactions (14), the flame temperature was restricted to be no greater than the boiling point of the metal oxide product. Consequently, at least some of the product was assumed to condense in the flame. The primary weaknesses of this model were the failure to include convective transport of the gases and the omission of product flow toward the droplet.

Kuehl and Zwillenberg (15) removed the restriction on the flow of vaporized product, allowing product vapor to flow both to the fuel surface and to infinity. The product was considered to condense at the fuel surface such that its vapor pressure was zero at the fuel surface. As in the work of Reference (13), all convective mass transport, except that of the condensed product formed in the flame, was neglected.

In addition, Kuehl and Zwillenberg assumed that the fraction of product vaporized in the flame was unaffected by the existence of a product flux toward the fuel surface.

Klyachko (16) approached the problem in a slightly different manner. All mass transport was considered to be by diffusion only with no convection and the flow of the condensed product was neglected. As in Reference (15), the flame temperature was limited to the boiling point of the products, and condensation of the products was limited to three locations: at infinity, in the flame, and at the fuel surface. However, Klyachko chose not to specify the fraction of products which were vaporized in the flame. Rather, he chose to specify the fraction of vaporized products which would flow inward to the fuel surface. Using intuitive arguments, Klyachko concluded that half the vaporized product would flow toward the droplet and half would flow to infinity. It should be emphasized that the actual value chosen for this parameter is unimportant, the significant point is that some constant value must be assumed in order to arrive at a solution.

Recent work by Law (17) is the most general analysis of combustion with condensable products to date. A general model was first developed in which the flame temperature was specified to be equal to the boiling point of the products. Mass transport of all gaseous species (metal vapor, oxidizer, and product vapor) was considered to be by both diffusion and convection. Transport of condensed product was assumed to be by convection only. Condensation of the products was assumed to occur at one, or more, of the following locations: flame zone, fuel surface, and infinity. Heat transfer was by convection and conduction only. Three special cases of the model were then

developed: no condensation of the products at the fuel surface (similar to Reference [15]); dilute oxidizer concentrations--such that the flame temperature falls below the boiling point of the products and all condensation occurs in the flame zone (similar to Reference [13]); and enriched oxidizer concentrations--such that the flame temperature exceeds the boiling point of the products and no condensation occurs in the flame.

The last of these special cases represents a significant improvement over the previous work; flame temperatures were no longer limited and condensation of products in the flame was not forced by the model. While it appears that the development of this model permits the analysis of all combustion conditions, there is one important exception. It can be shown that the mass flux equations for the metal vapor and the product vapor in the region between the fuel surface and flame are not independent if the following conditions are satisfied: (a) no product condenses in the flame; (b) condensation of products flowing toward the fuel occurs only at the fuel surface; (c) no inert gas is present--such that only metal vapor and product vapor exist at the fuel surface.

Law and Williams (18) have extended the work of Reference (17) to allow condensation of the products outside the flame to occur at a finite distance from the flame, rather than at infinity. The flame temperature was limited to values above the boiling point of the products. Condensation of the products was permitted to occur only at the droplet surface and at the outer condensation front. The temperature at the outer condensation front was specified as the boiling point temperature of the products. The model predicts

an infinite burning rate for the case of pure ambient oxidizer.

A great deal of experimental work has been performed concerning combustion of metals. Like the theories, however, the work has concentrated on metal-oxygen reactions, generally with an inert diluent gas present (see for example, References [19-22]). No data directly applicable to the present study were found.

1.3 Specific Statement of the Problem

As indicated by the previous discussion, existing theoretical models all contain flaws that preclude their use for any practical combustion problem in the absence of an inert gas. The models are either singular for pure oxidizer or are not well-posed, requiring that the behavior of one of the unknowns be specified. In addition, the solubility of the products in the metal is neglected.

Secondly, experimental work to date has concentrated on metal-oxygen reactant combinations. Little information exists on the combustion characteristics of other combinations, particularly alkali metals reacting with halogenated gases. Burning rate data on these other combinations are needed to verify any new combustion model and to examine the applicability of existing models to this class of reactions. As indicated previously, the lithium-sulfur hexafluoride combination is especially interesting because of its technological importance.

With this in mind, the specific objectives of the present study are as follows:

- (1) Determine the nature of lithium-sulfur hexafluoride combustion by visual observation.

- (2) Obtain data on lithium burning rates from a wick surface as a function of three parameters: ambient pressure, wick length, and concentration of inert diluent in the ambient gas.
- (3) Develop a film-theory model of combustion of a liquid metal from a plane surface, including:
 - (a) pure oxidizer as the ambient gas;
 - (b) condensation of products occurring at fronts not restricted to being located at infinity, the flame, or the fuel surface; and
 - (c) solubility of the products in the molten fuel.
- (4) Compare the model with burning rate data.

CHAPTER II

APPARATUS AND PROCEDURE FOR OBSERVATION OF LITHIUM COMBUSTION AND BURNING RATES

Two series of tests were performed to observe the nature of lithium combustion and to obtain lithium burning rates. Lithium droplets were burned in sulfur hexafluoride to observe the qualitative characteristics of lithium combustion. Larger samples of lithium were burned from a wick in sulfur hexafluoride and mixtures of argon and sulfur hexafluoride to obtain burning rate data. Photographs of the larger samples were used to obtain a clearer understanding of the lithium-sulfur hexafluoride combustion process. The information gained from the photographs of the combustion process was necessary before a proper mathematical model could be chosen.

2.1 Preliminary Tests--Combustion of Lithium Droplets

2.1.1 Apparatus

The apparatus used to observe combustion of lithium droplets consisted of a glass bell jar, a gas supply system, an ignition circuit, a camera, and the lithium droplet mounted on a thin support rod. A schematic of the test apparatus is shown in Figure 2.

The test samples consisted of small lithium shot about 2-3 mm in diameter mechanically mounted on a nickel support rod. A primer, made from two strands of 28 gauge Ni-Chrome wire about 3-4 mm long, was inserted into the lithium shot.

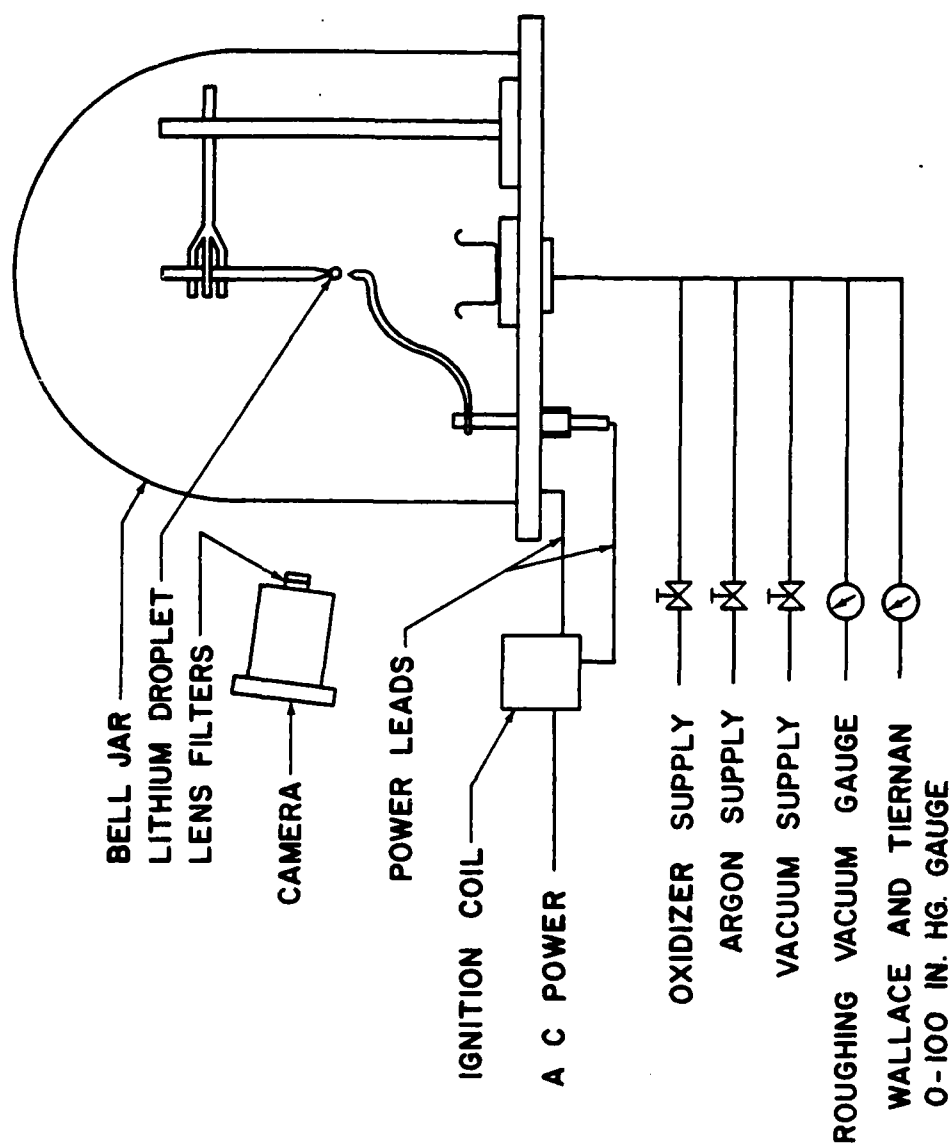


Figure 2 Schematic of Apparatus for Observation of Lithium Droplet Combustion

Photographs of each test were taken with a 4 inch x 5 inch Graflex Super Graphic fitted with a 135 mm Optar lens. Polaroid Type 57 black and white film (ASA 3000) was used.

The spark ignitor was powered by a General Electric ignition transformer, Model 56 G 9, with 10000 volt output at 23 milliamps. The hot side of the circuit was run through a pointed copper lead, and the circuit was grounded through the base of the bell jar. The spark gap was formed between the tip of the copper lead and the primer inserted into the lithium shot.

The glass bell jar provided a means by which the combustion process could be observed, as well as a means to control the combustion conditions. The gas and vacuum supply system was connected to the inside of the bell jar as shown in Figure 2. The system was designed primarily to set the pressure of the sulfur hexafluoride inside the bell jar for each test. The argon line was provided to be able to backfill the bell jar after a test was completed. The pressure in the bell jar was measured with a Wallace and Tiernan Model FA-129, 0-340 kPa (0-100 in. Hg) absolute pressure gauge with ± 340 Pa (0.1 in. Hg) accuracy. A roughing gauge was provided as a back-up to the Wallace and Tiernan gauge.

2.1.2 Procedure

The test samples were assembled in a vacuum/glove box under an argon atmosphere in order to protect against contamination of the lithium shot. A completed sample, consisting of the support rod, the lithium shot, and the Ni-Chrome primer, was placed in a glass jar and sealed under argon until it was needed for a test.

After the camera was adjusted, the sample was removed from the jar and placed on the bell jar base. The space between the copper ignition lead and the Ni-Chrome primer was set to about 3 mm. The bell jar was placed over the sample, and the system was evacuated. The system was then back-filled with sulfur hexafluoride to about 20250 Pa. The spark was activated until ignition occurred. (The spark concentrated on the Ni-Chrome primer, heating the primer to where it would ignite in the sulfur hexafluoride. The heat released by this reaction was sufficient to ignite the lithium.) When ignition was confirmed, the spark was turned off and the photograph was taken. Because of the light intensity of the flame, welder's goggles were worn to allow direct observation.

2.2 Lithium Burning Rate Tests

The apparatus used for the lithium burning rate tests consisted of a test sample, a vacuum chamber, a gas supply system, and instrumentation.

2.2.1 Test Sample

A schematic of a typical test sample for the lithium burning rate tests shown in Figure 3. The flame position is included to indicate the orientation of the sample during the tests and the general shape of the boundary layer during combustion. The ends of the cylinders were 0.94 mm Type 316 stainless steel sheet with the side made of Type 316 stainless steel woven wire cloth, 3937 wires per meter and 0.1143 mm diameter wire. The cylinders were about 31 mm in diameter and 14 mm to 60 mm high, with 4 mm to 10 mm extending below the bottom disk. The extended section was backed by a strip of

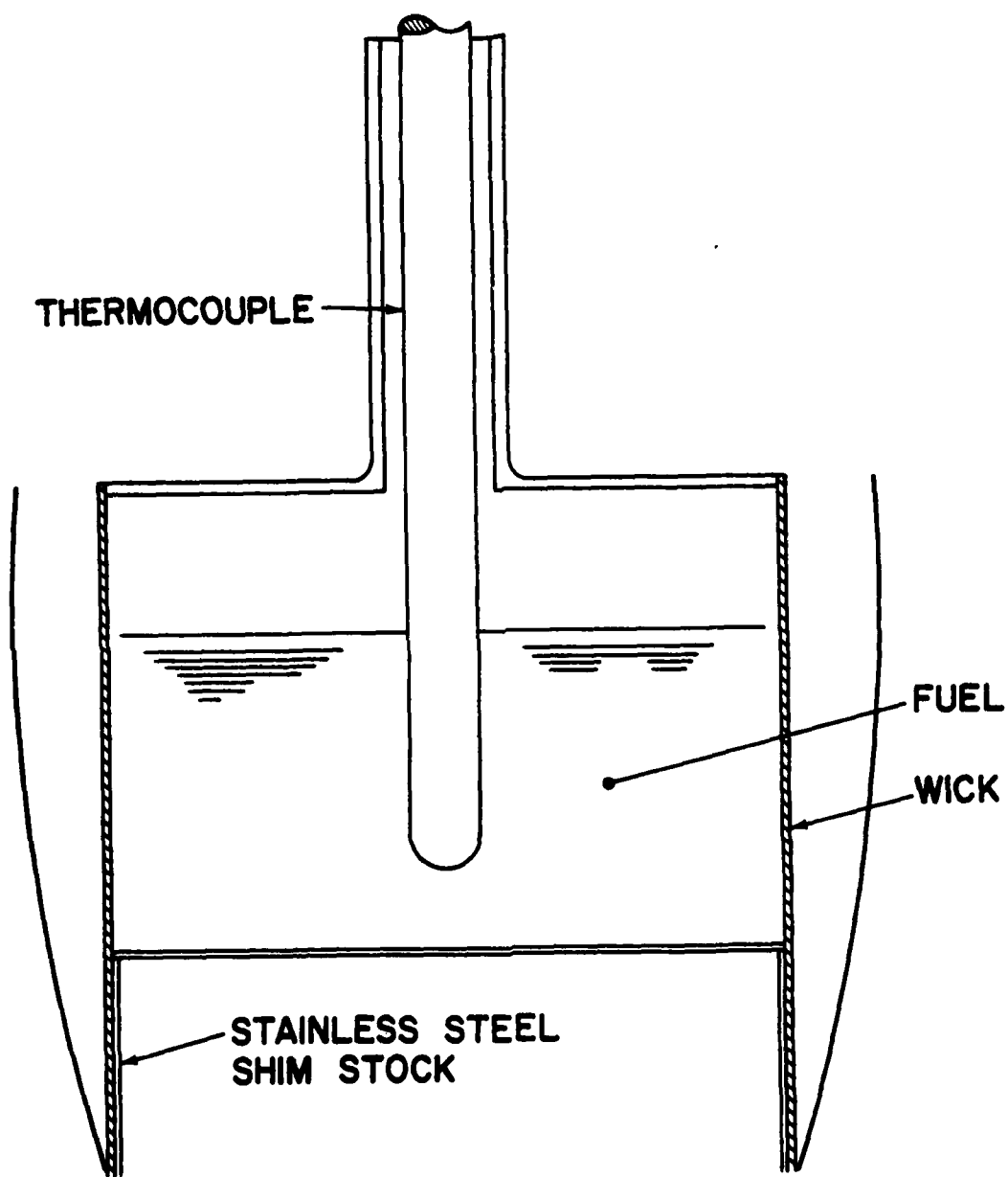


Figure 3 Schematic of Test Sample for Lithium Burning Rate Tests

stainless steel shim stock. The extension served to prevent lithium from wicking along the bottom of the sample cylinder. The wick was spotwelded to the edge of the disks. The top disk was similar to the bottom disk, except for a 6.4 mm hole drilled in the center. A 6.4 mm O.D. tube about 10 mm to 50 mm long was welded into the hole.

During combustion, the lithium inside the sample would wet the wick, including the extended section, and maintain a supply of fuel to the wick by means of capillary action. When the lithium was consumed, the wick dried off, and combustion ceased (much like a kerosene lamp that has burned all the fuel).

2.2.2 Vacuum Chamber

The lithium burning rate tests were performed inside the vacuum chamber shown in Figure 4. The chamber, a VAC Model HE-133-5, manufactured by the Vacuum Atmospheres Corporation, is a truncated cylinder approximately 0.65 m in diameter and 0.91 m long. The interior volume is approximately 0.35 cubic meters.

The arrangement of the apparatus inside the vacuum chamber is shown schematically in Figure 5. Figure 6 is a photograph of a test sample set in place, showing the heater coil, the ignition lead, and the thermocouple in the foreground, and the collapsible bag in the background.

As can be seen in Figure 5, the stainless steel tube in the top of the test cylinder was connected to the collapsible bag. A chromel-alumel thermocouple was used to monitor the temperature of the lithium inside the test sample. A collar of stainless steel shim stock was placed above the sample to protect the thermocouple from thermal radiation.

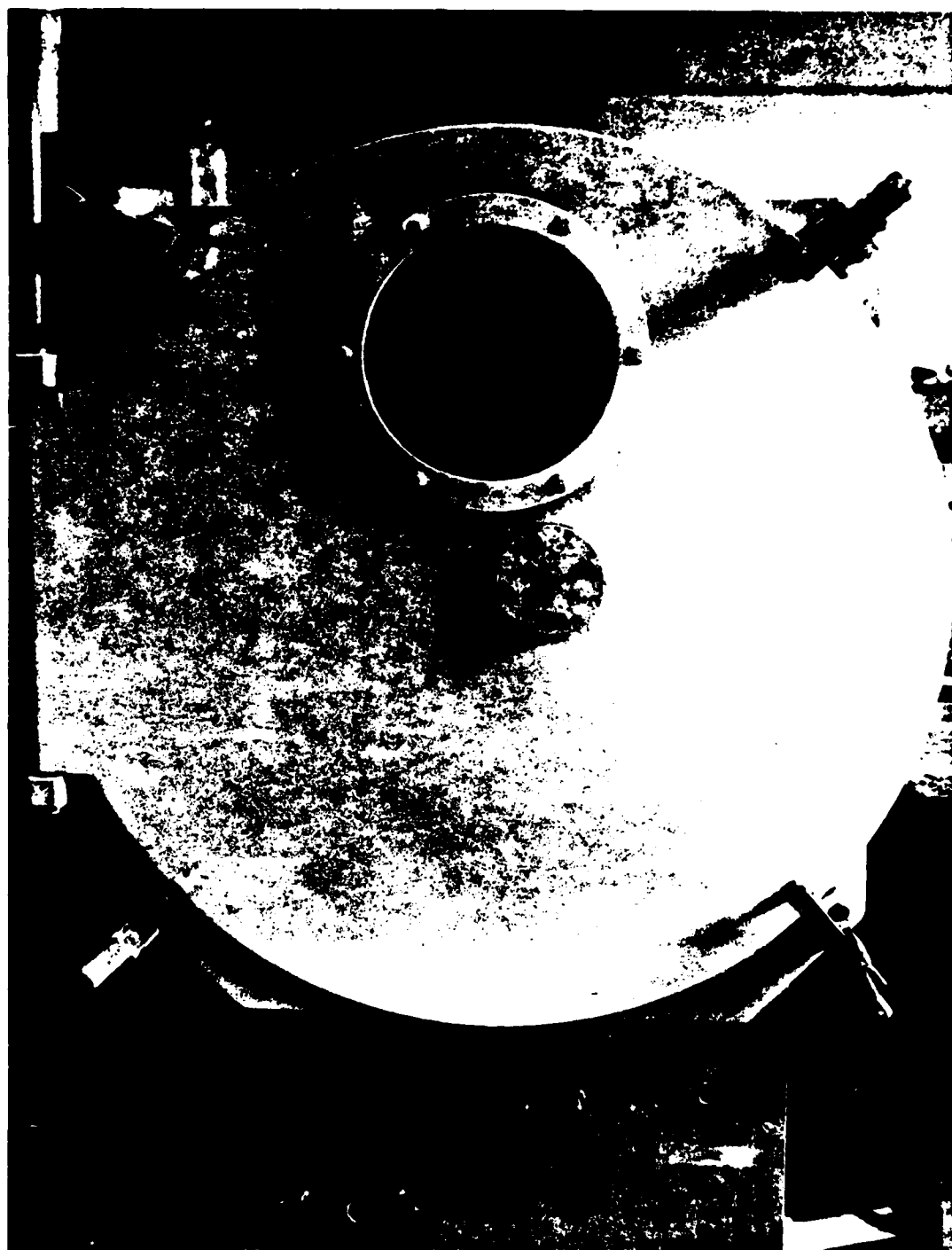


Figure 4 Vacuum Chamber

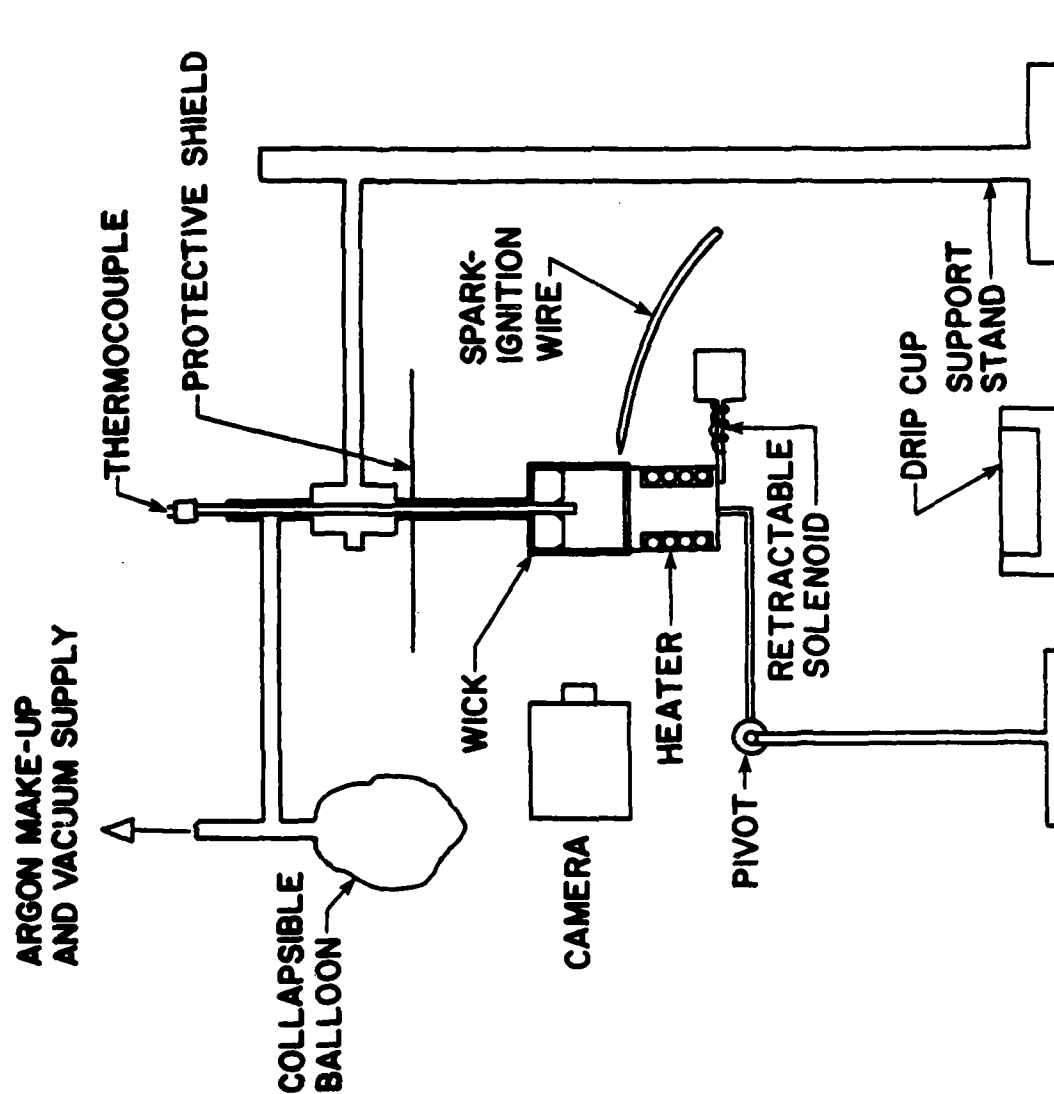


Figure 5 Schematic of Apparatus to Determine Lithium-Sulfur Hexafluoride Burning Rates



Figure 6 Photograph of the Test Apparatus Inside Vacuum Chamber

A small heater coil wrapped around a copper core was used to raise the test sample to ignition temperature. The heater coil was made from a shortened section of 1500 W. Ni-Chrome beaded heater, manufactured by the Cole-Parmer Instrument Company (P/N 3116-40). The current through the heater was controlled by a Type W20MT3A Metered Variac Autotransformer, manufactured by the General Radio Company. The heater coil was held in contact with the test sample by means of a retractable solenoid. The ignition circuit was the same as used for the lithium droplet combustion tests.

Since it was necessary to prevent oxidizer from reaching the interior of the test sample and reacting, this region was filled with argon. The argon also served to protect the thermocouple from corrosion by the oxidizer. The collapsible bag was required in order to keep the gas pressures on the two sides of the wick in balance as the test sample heated and the fuel was consumed.

2.2.3 Gas Supply System

The gas supply system illustrated in Figure 7 was used to set the desired test conditions in the vacuum chamber. The system was arranged to allow the oxidizer and the argon to be fed into the chamber independently, while only argon could be fed to the inside of the collapsible bag. A vacuum could be drawn on each part of the system, independent of all other parts. The vacuum pump was a Duo-Seal Model 1397, manufactured by the Welch Scientific Company. A manually operated vacuum by-pass was provided to the chamber interior in the event that the solenoid failed.

2.2.4 Instrumentation

Pressure measurements were made using a Miriam absolute pressure mercury manometer graduated in millimeters. The lithium temperature was measured using a Conax grounded chromel-alumel thermocouple encased in a 3.17 mm diameter Type 316 stainless steel sheath. The thermocouple output was recorded on a Leeds and Northrup Speedomax H Type S Multipoint Recorder. The recorder was set for single point operation, allowing a temperature to be read every 1.5 seconds. The extension leads and recorder were calibrated with a Leeds and Northrup Model 8686 millivolt potentiometer. The temperature-to-millivolt conversions were taken from the National Bureau of Standards tables.

Burning times were measured with two Heuer stopwatches with 0.2 second divisions. The Speedomax was used to provide a back-up timing system. The times recorded agreed to about $\pm 3\%$ between the hand-timing and the times obtained from the Speedomax charts.

Photographs during each test were taken using the same method as used for the lithium droplet photographs.

2.2.5 Reactants

The lithium fuel used for the tests was obtained from the Lithium Corporation of America. The fuel was packed in cans in two-pound lots and sealed under argon. The lithium is guaranteed as 99.9% pure with the major impurity being sodium.

The sulfur hexafluoride was obtained from Matheson Gas Products. The gas is contained in a cylinder as a liquid under its own vapor pressure (2200 kPa at 294 K). The gas used was certified purity grade--minimum of 99.8% pure.

The argon used was obtained from AIRCO and was Commercial Grade--99.9998% pure.

2.2.6 Procedure

2.2.6.1 Preparation of Test Samples

Test samples were made in a four-step process designed to reduce the occurrence of contamination of the lithium. The first step of the preparation was to weigh a small sample of lithium inside a vacuum/glove box under an argon atmosphere. The amount of lithium used in the samples ranged from about 2 to 12 grams, depending on the cylinder height to be tested. After the fuel was weighed, the lithium was placed in a glass jar and sealed under argon.

The second step was the fabrication of the bottom and sides of the sample cylinder. The cup-like part was made as described in Section 2.2.2 and rinsed in reagent grade methanol. All this was done before the lithium was removed from the jar and exposed to the air.

The third step was to attach the top to the sample cylinder. The test sample was completed by removing the lithium from the jar and placing the fuel in the bottom part of the cylinder. The top was then spot-welded in place. To avoid undue contamination of the lithium, the completed test sample was returned to the vacuum/glove box as quickly as possible.

The final step of the preparation of the test samples was to pre-wet the wick and install the primer. The samples were heated to 700-750 K to pre-wet the wick. Experience has shown that lithium will wet a wick in this temperature range if the wick is below the liquid surface. By sloshing the sample a little, it was possible to wet most,

or all, of the wick surface. After the sample cooled, a small globule of lithium (about 0.02 gm) was mechanically attached to the outside of the wick surface. A primer about 4 mm long, made from four strands of 28 gauge N-Chrome wire twisted together, was then inserted into the globule of lithium and allowed to stick out past the surface. The assembled sample can be seen in Figure 6. As before, this step was performed in a vacuum/glove box under argon.

2.2.6.2 Test Procedures

The sample was placed in a sealed glass jar and moved to the vacuum chamber. Before the sample was removed from the jar all the components inside the vacuum chamber were positioned for the test. The sample was removed from the jar and fastened to the support. The tip of the copper ignition lead was placed about 1 mm away from the primer. A quick test of the ignition circuit was made and the door of the chamber was sealed. Another test of the ignition circuit was made in case the apparatus had moved while the door was being sealed.

The vacuum line to the collapsible bag was opened, and, several seconds later, the solenoid valve to the chamber was opened. Both gas supply lines were evacuated back to the regulators and the entire system was allowed to pump. Two or three hours was usually sufficient to evacuate the system, although many samples were allowed to pump overnight. When the system was totally evacuated, the heater coil was turned on at a power level of about 100 W. The thermocouple was used to monitor the temperature of the lithium. When the fuel temperature reached about 670 K, the vacuum was shut off. A small amount of argon

was back-filled into the collapsible bag until it was partially inflated. The gases were then introduced into the vacuum chamber to obtain the desired test condition. In any test where argon was mixed with the sulfur hexafluoride, the argon was introduced into the chamber first.

When the test conditions were set, the heater was turned off. The support solenoid was activated, causing the support to retract and the heater to swing out of the way. The ignition circuit was fired, starting an arc to the Ni-Chrome primer. The primer burned in the oxidizing atmosphere and ignited the small globule of lithium attached to the outside of the wick. Almost immediately (less than one second) the flame could be seen to spread rapidly over the entire wick surface. The observance of this rapid spread was defined as the ignition point. The ignition circuit was de-energized soon after ignition. A photograph was taken about five to ten seconds after ignition occurred. Combustion continued very evenly over the wick until the fuel was exhausted. The flame would die about as quickly as it spread (about one second). Burning times were stopped when this rapid decay was seen.

As soon as the test was over, the chamber was evacuated to remove the oxidizer. Experience showed that the stainless steel pieces of the test sample had a tendency to react with the oxidizer if the pressure was high enough (about 10000 Pa). When the sample had cooled, the chamber was backfilled with argon to atmospheric pressure.

The amount of lithium which had not burned during the test was determined according to the technique described in Appendix A. Most of the unburned lithium found after a test had dripped off of the sample

during the burning time. These droplets were usually easily distinguished from the droplets of product which dropped off during the test.

The lithium burning rate was then calculated from the amount of lithium burned, the surface area of the wick, and the measured burning time.

CHAPTER III

RESULTS OF LITHIUM COMBUSTION AND BURNING RATE TESTS

3.1 Observation of the Lithium Combustion Process

Figure 8a and its enlargement, Figure 8b, show a lithium droplet burning in sulfur hexafluoride at a pressure of 20200 Pa. Image size in Figure 8a is about one-third larger than actual size. Several important preliminary observations can be made about the lithium-sulfur hexafluoride combustion process from this photograph. The liquid surface appears to be smooth and surrounded by a glowing region in the gas phase. The liquid fuel droplet appeared to decrease in size as combustion proceeded, in a manner similar to an oil droplet combustion process. The darker areas seen on the fuel surface are believed to be small droplets of condensed combustion products.

Significant amounts of condensed combustion products were seen in the gas phase. The products were convected upward and tended to condense on any adjacent cool surfaces, particularly the nickel support rod. Figure 9 is a photograph of the rod after combustion has ended. A large droplet of solidified product can be seen part-way up the rod, above the position of the fuel droplet. Small globules of product are also evident at the tip of the support rod. These may correspond to the product which condenses on the fuel surface as suggested by the darker areas seen in Figure 8. The amount of product which condenses on the fuel surface is small compared to the amount present in the gas phase.



(a)



(b)

Figure 8 Combustion of a Lithium Droplet in Sulfur Hexafluoride

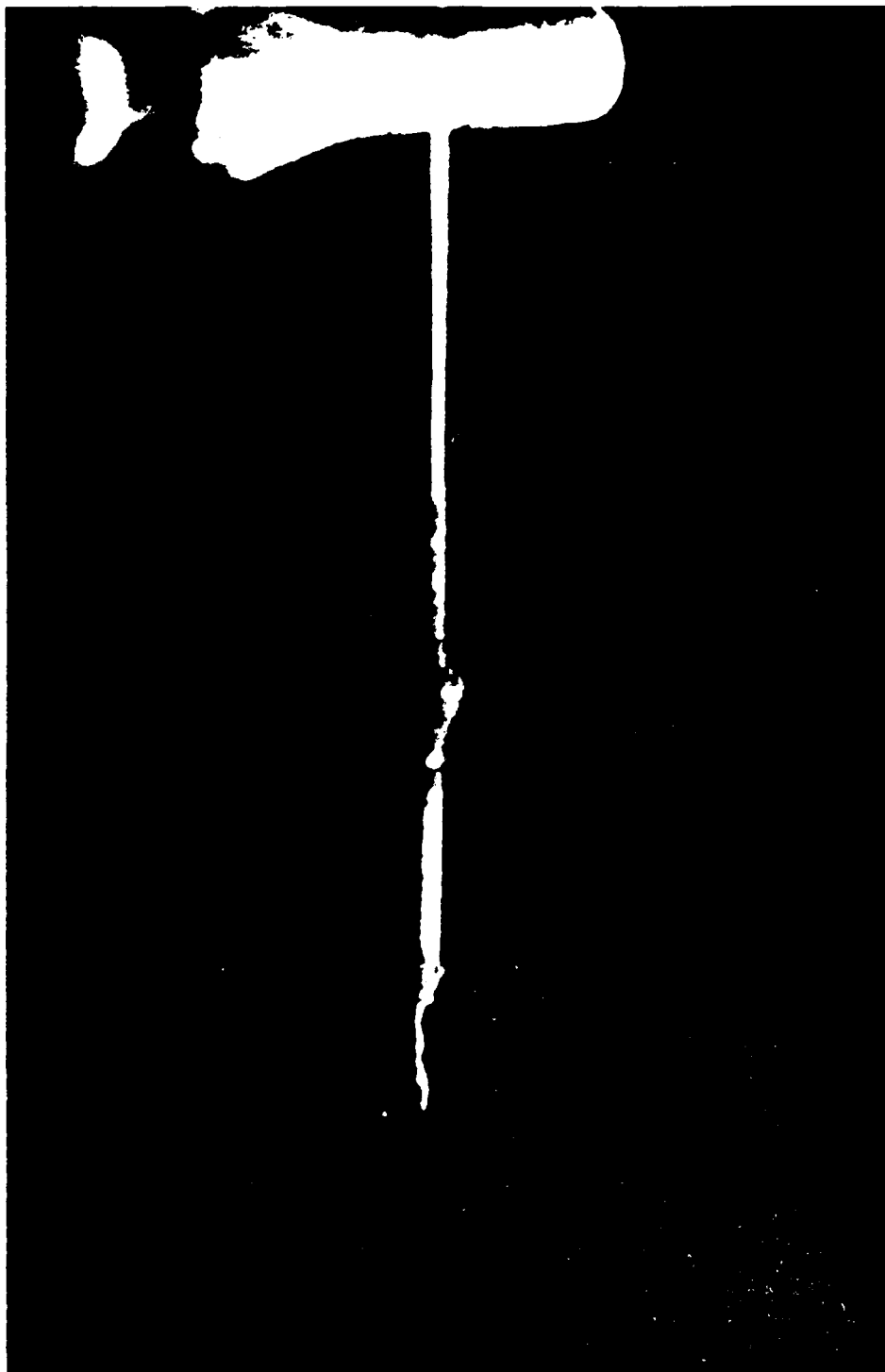
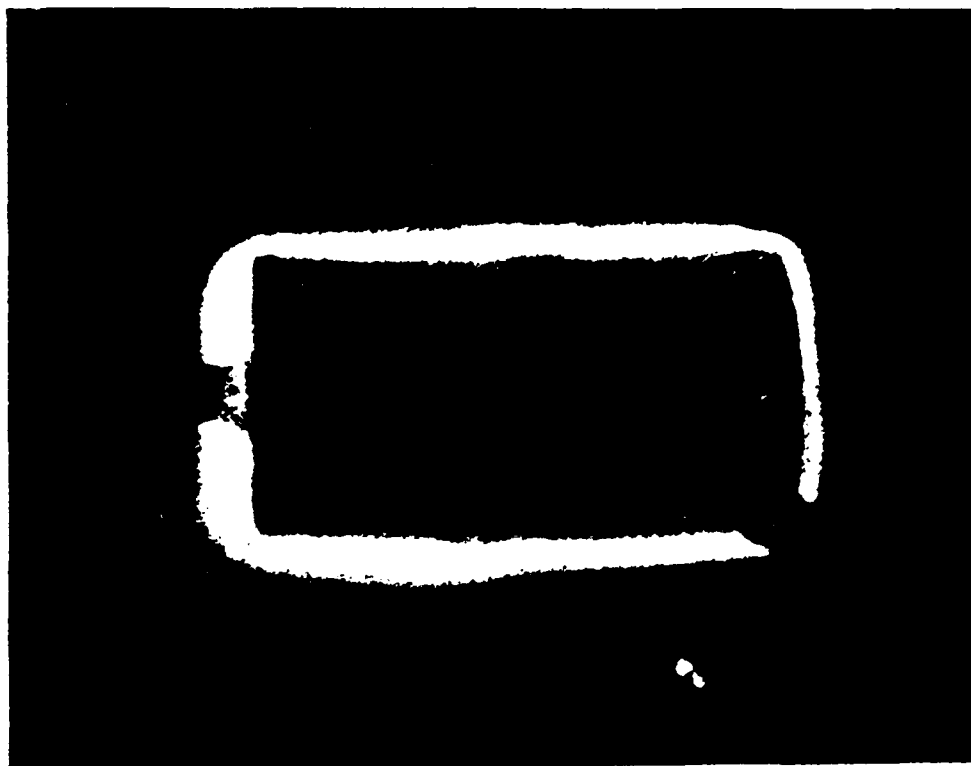


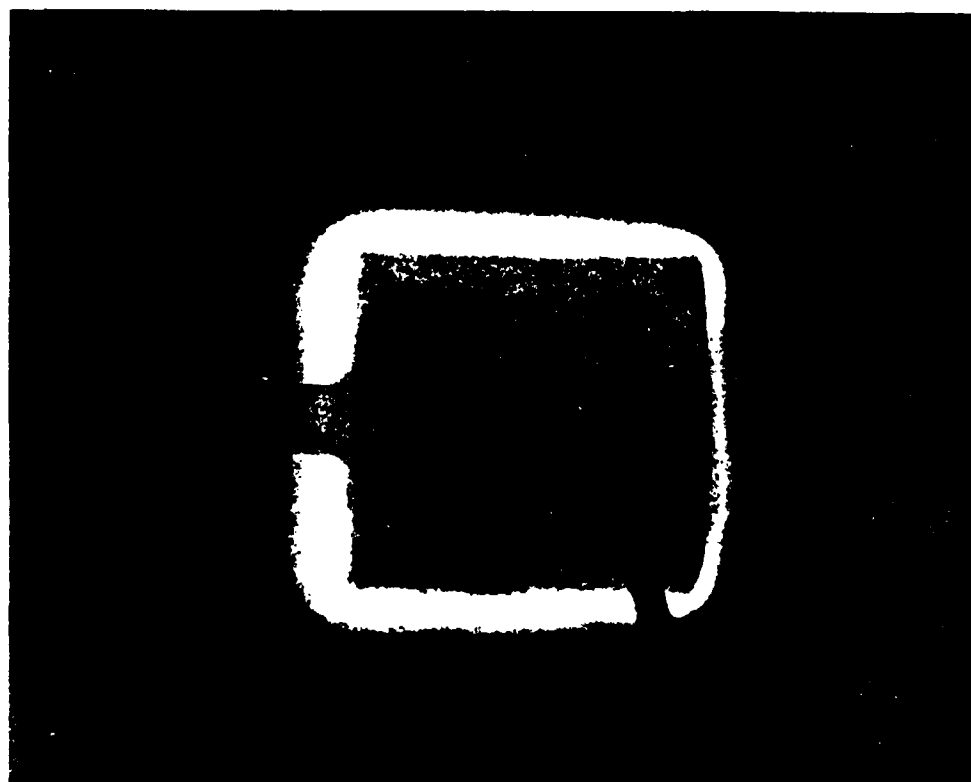
Figure 9 Product Accumulation on Support Rod After
Combustion of Lithium Droplet in Sulfur
Hexafluoride

Because of the amount of condensed product particles present in the gas phase, the glowing region surrounding the fuel droplet cannot be labeled a "flame zone." The glowing region is more likely defined by an isothermal boundary beyond which the particles no longer radiate at frequencies in the visual range. Since the high temperature levels can only be maintained by the reaction, it can be inferred that the actual flame zone lies within the glowing region, but a precise position cannot be identified from the photographs of the droplet combustion.

Much more definitive information can be obtained from the photographs of lithium combustion from a wick, seen in Figure 10 and Figure 11. Figure 10 shows two typical tests of lithium burning in sulfur hexafluoride; Figure 11 shows two typical tests of lithium burning in argon-sulfur hexafluoride mixtures. All the photographs exhibit the same general characteristics as the photographs of the droplet combustion. The wick surface is smooth and partially covered by condensed product, which is much more visible in these pictures. The behavior of the product condensed on the fuel surface was quite consistent over all conditions tested. Small droplets of product would form on the wick surface as seen in Figure 10a. The droplets flowed down the surface under gravitational influence and agglomerated as they fell. Figure 10b shows the agglomerated product about halfway down the wick. The product continued to flow to the bottom of the wick. When a sufficiently large droplet formed at the bottom of the wick, the product would drip off. As can be seen in both Figure 10 and Figure 11, the product covers a fairly small amount of the wick surface. Table 1 summarizes the amount of wick surface

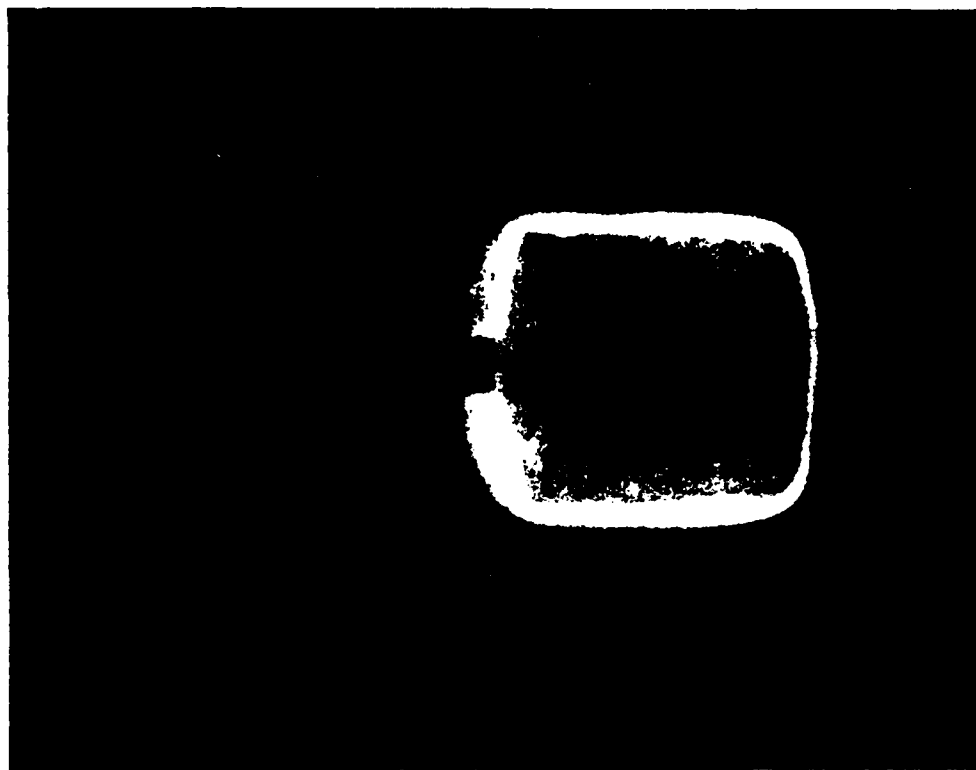
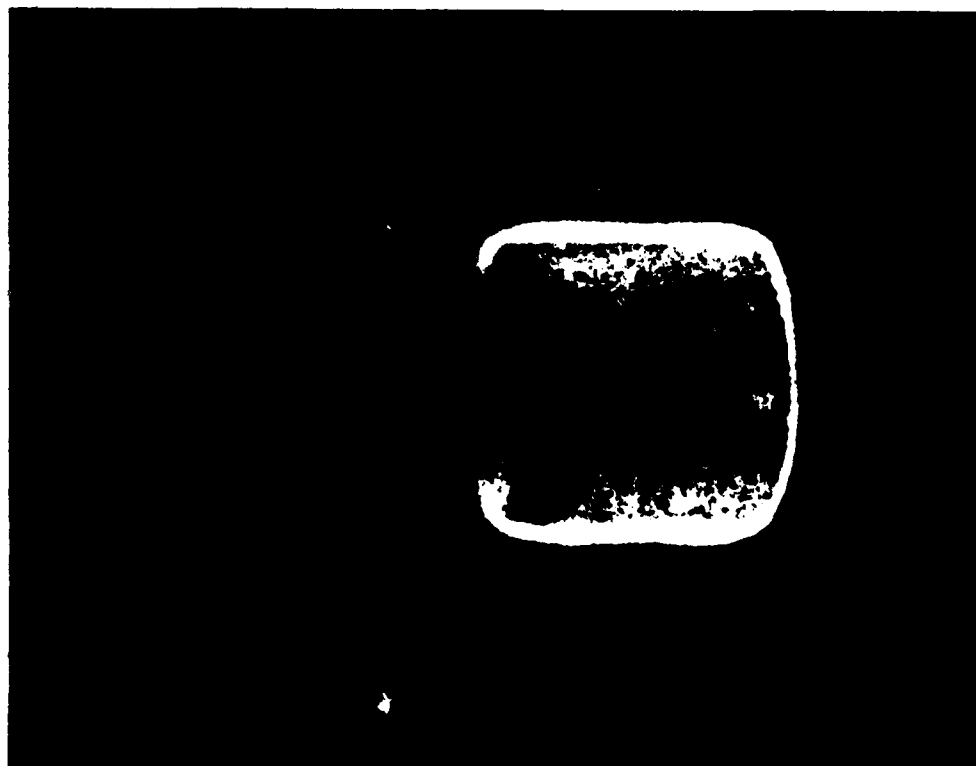


(b)



(a)

Figure 10 Combustion of Lithium from a Wick in Sulfur Hexafluoride



(a) (b)
Figure 11 Combustion of Lithium from a Wick in Argon-Sulfur Hexafluoride Mixtures

Table 1

Summary of Surface Area Covered by Product

Test	Length mm	Pressure Pa	Argon Mass Fraction	A_p/A_{tot} (%)
6	3.0	7900	0.0	10
8	3.0	13600	0.0	8
11	3.2	5250	0.0	3
14	3.25	10750	0.0	10
17	3.0	15950	0.0	9
34	6.0	10750	0.0	15
36	5.95	8050	0.0	2
38	5.9	10750	0.0	13
45	2.9	13300	0.0	0
47	1.42	10750	0.0	0
52	1.62	10750	0.0	4
53	1.52	10750	0.0	4
54	1.65	10750	0.0	30
31	3.0	13300	0.002755	13
39	2.9	13300	0.004707	5
40	3.05	13300	0.00668	6
46	2.9	13300	0.00137	20
48	3.05	13300	0.00583	4
49	3.05	13300	0.00165	13
51	2.97	13300	0.00137	9

covered by condensed product in each of the photographs obtained. The dark silhouette seen in Figure 10 is the ignition wire described in Section 2.2.2.

The percentage of wick surface covered by product was determined by analyzing the photographs as follows: (a) the vertical centerline was located on the sample; (b) parallel lines were drawn on each side of the centerline at a distance equal to one-half the radius; (c) the surface area covered by the product (the darker areas) inside this rectangle was measured; (d) the area covered by the product was divided by the area of the rectangle; (neglecting the curvature of the wick surface). This value was assumed to be representative of the conditions on the entire wick surface.

There is no correlation between the amount of surface area covered by condensed product and pressure or argon mass fraction. The amount of surface area covered by product seemed to be related to the time the picture was taken. If a drop of product had just fallen off the sample, the percentage of surface area covered was low. If the product were almost ready to drop off, the covered area was somewhat larger. No attempt was made to take the photographs at a particular condition. It is likely that the results obtained represent a fairly random sample of conditions. If this is true, then the results obtained lead to the conclusion that the average amount of wick surface covered by condensed product is on the order of 10% of the wick surface.

The luminous zone seen in the photographs of droplet combustion can also be seen in the photographs of combustion from a wick. One significant addition can be seen in the latter photographs. A second

zone, more intense than the outer envelope, can be seen along the surface of the wick. This brighter zone extends out from the surface about 1 mm in the photographs, ending at a thin, somewhat darker region. The darker region is believed to be the location of the flame. The flame temperature should be high enough (see Section 6.1) so that no products can condense in the flame. Consequently, there will be no particles in the flame to emit radiation. It follows, therefore, that the intensity of light emitted from the flame will be the lowest of the high-temperature regions of the boundary layer.

The light zones at the top and bottom of the samples are caused by the fact that the camera was "looking" through a hollow cylinder of luminescent material. The photographs recorded the near and far sides of the cylindrical flame, causing these areas to seem more intense than they actually were.

The photographs were analyzed to obtain the dimensions of the two zones. Figure 12 is a plot of the thickness of the flame zone versus the modified Grashof number suggested by Spalding (23) for combustion of a liquid fuel under natural convection conditions. The thickness of the luminous envelope plotted versus the same Grashof number is shown in Figure 13. Both the plots are for the data obtained from the photographs of lithium combustion in sulfur hexafluoride with no argon present. A least-squares linear regression of the data yields the following results:

$$\delta_f/x \propto Gr^{-.249}$$

$$\delta_{lum}/x \propto Gr^{-.234}$$

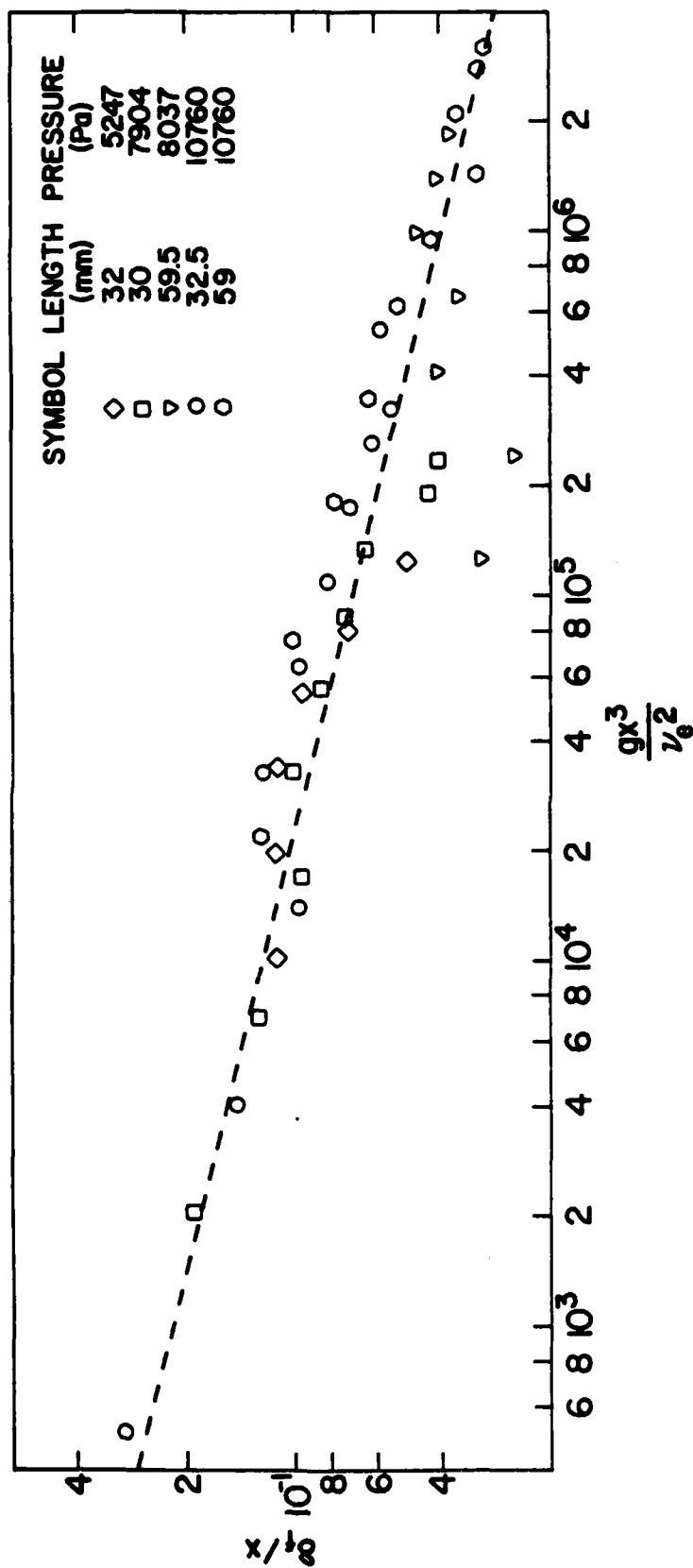


Figure 12 Flame Stand-Off Distance for Combustion of Lithium from a Wick in Sulfur Hexafluoride

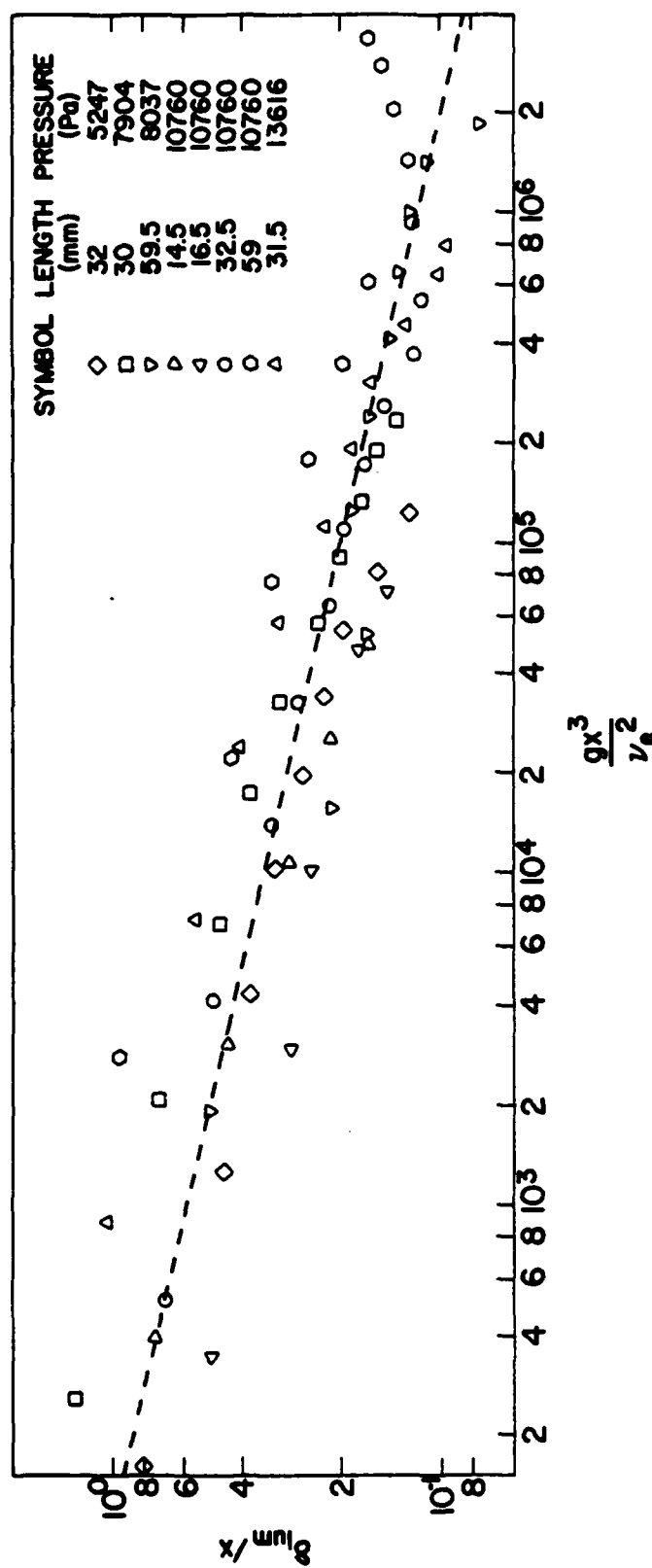


Figure 13 Luminous Zone Thickness for Combustion of Lithium from a Wick in Sulfur Hexafluoride

It is worth noting that these results are close to what would be expected for laminar natural convection from a vertical plane surface, where the relationship for boundary layer thickness is (23, 24):

$$\delta/x \propto Gr^{-.25}$$

The results seen in Figures 12 and 13 indicate that laminar natural convection was occurring during the lithium burning rate tests. The maximum local Grashof number during the tests was approximately 3×10^6 , which is less than the value of 10^8 where transition to turbulent flow normally occurs during combustion under natural convection conditions (24). In addition, the slope of the data is quite close to the theoretical value for laminar natural convection.

3.2 Lithium Burning Rates in Sulfur Hexafluoride

Table 9 in Appendix B is a summary of the data obtained for lithium burning in sulfur hexafluoride. Two series of tests were run in the sulfur hexafluoride. One series was to determine the effect of oxidizer pressure for a constant wick length. The other series was to determine the effect of wick length for a constant oxidizer pressure.

Figure 14 shows the effect of oxidizer pressure of the lithium burning rate for a constant wick length (nominally 30 mm). A least-squares linear regression of the data shows the lithium burning rate to be approximately proportional to oxidizer pressure to the 3/4 power:

$$G_m \propto p^{.77}$$

The results at pressures greater than 8000 Pa, indicate an even stronger pressure dependence. In comparison to natural convection

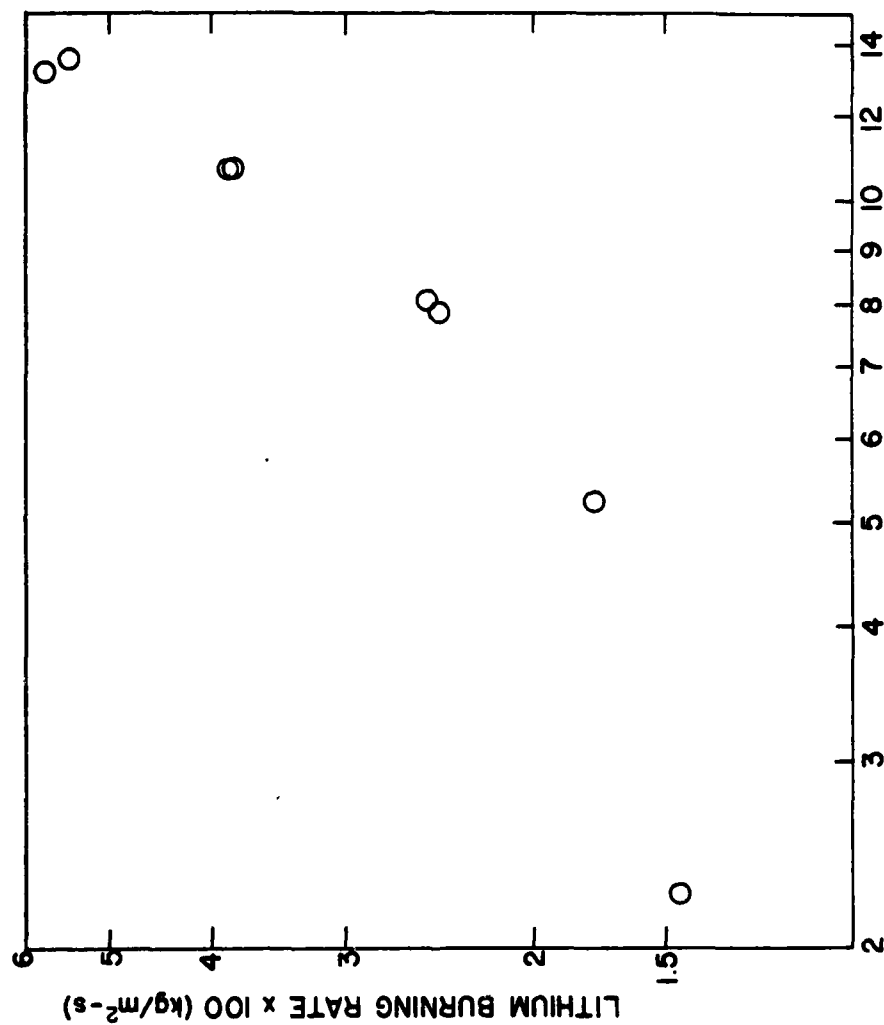


Figure 14 Effect of Pressure on Lithium Burning Rate in Sulfur Hexafluoride for a Constant Wick Length (30 mm)

processes, this result is somewhat startling. The more expected results would be that burning rate is proportional to the square root of oxidizer pressure (24).

Figure 15 shows the effect of wick length on the burning rate for a constant oxidizer pressure (10750 Pa). A least-squares linear regression of these data points shows the burning rate to be approximately proportional to the fourth root of wick length:

$$G_m \propto L^{-.252}$$

This result is what would be expected in the case of laminar free convective combustion (24).

The results obtained to this point appear to indicate that a laminar natural convection process is occurring, at least for the conditions studied. The relationships seen for the flame thickness and the luminous zone thickness versus the Grashof number, combined with the effect of wick length, point to linear free convection. The one result that does not agree with results of earlier work (24), the effect of pressure, apparently indicates some other process or processes at work. Consequently, any mathematical model chosen must be able to account for this behavior.

3.3 Lithium Burning Rates in Argon-Sulfur Hexafluoride Mixtures

Table 10 in Appendix B is a summary of the data obtained for lithium burning in argon-sulfur hexafluoride mixtures. The tests were run at a constant total pressure of 13300 Pa. Argon mole fractions varied from 0.0% to 2.4%, corresponding to a variation in argon mass fraction from 0.0% to 0.668%. Difficulties in igniting the sample prevented testing for burning rates at higher concentrations of argon.

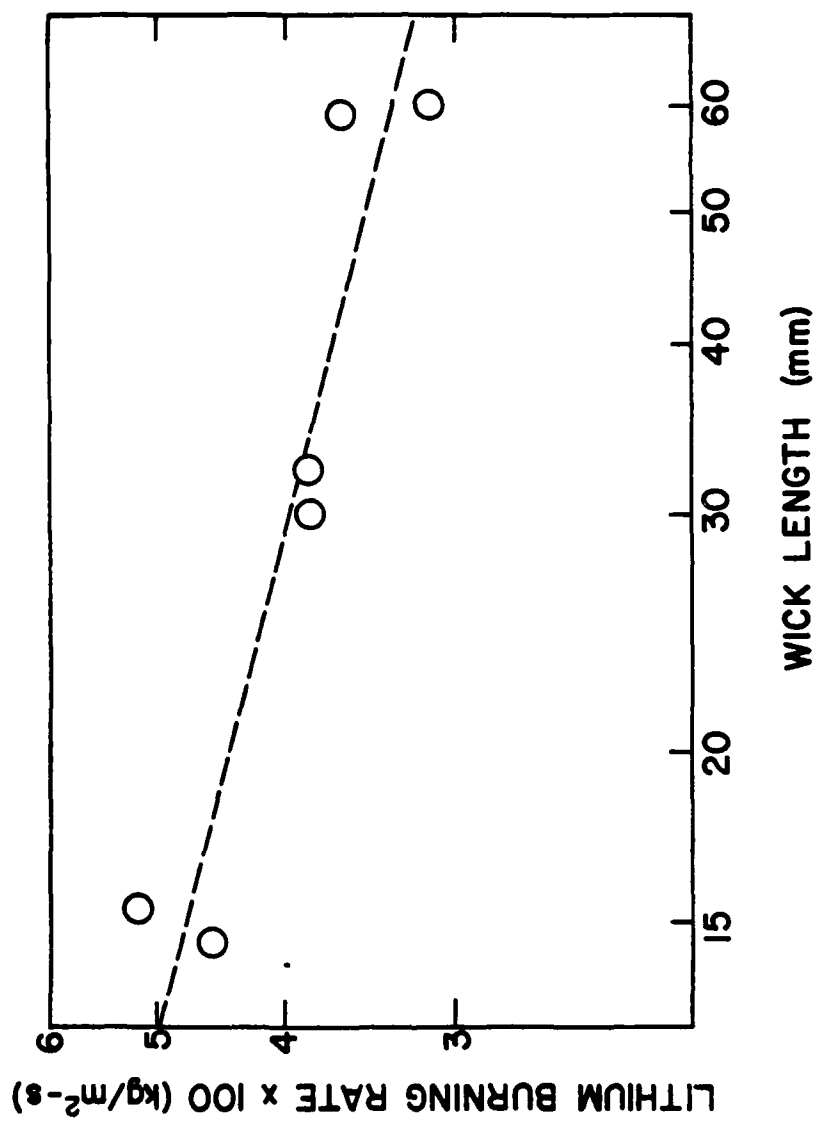


Figure 15 Effect of Wick Length on Lithium Burning Rate in Sulfur Hexafluoride for a Constant Pressure (10750 Pa)

As noted earlier, the presence of argon had no noticeable effect on the amount of wick surface covered by condensed product. However, the argon did have a significant effect on the lithium burning rate. Figure 16 is a plot of the lithium burning rate versus the ambient mass fraction of argon at a constant total pressure. A value of argon mass fraction of 0.668% causes a decrease in lithium burning rate of over 45% as compared to the lithium burning rate for no argon present.

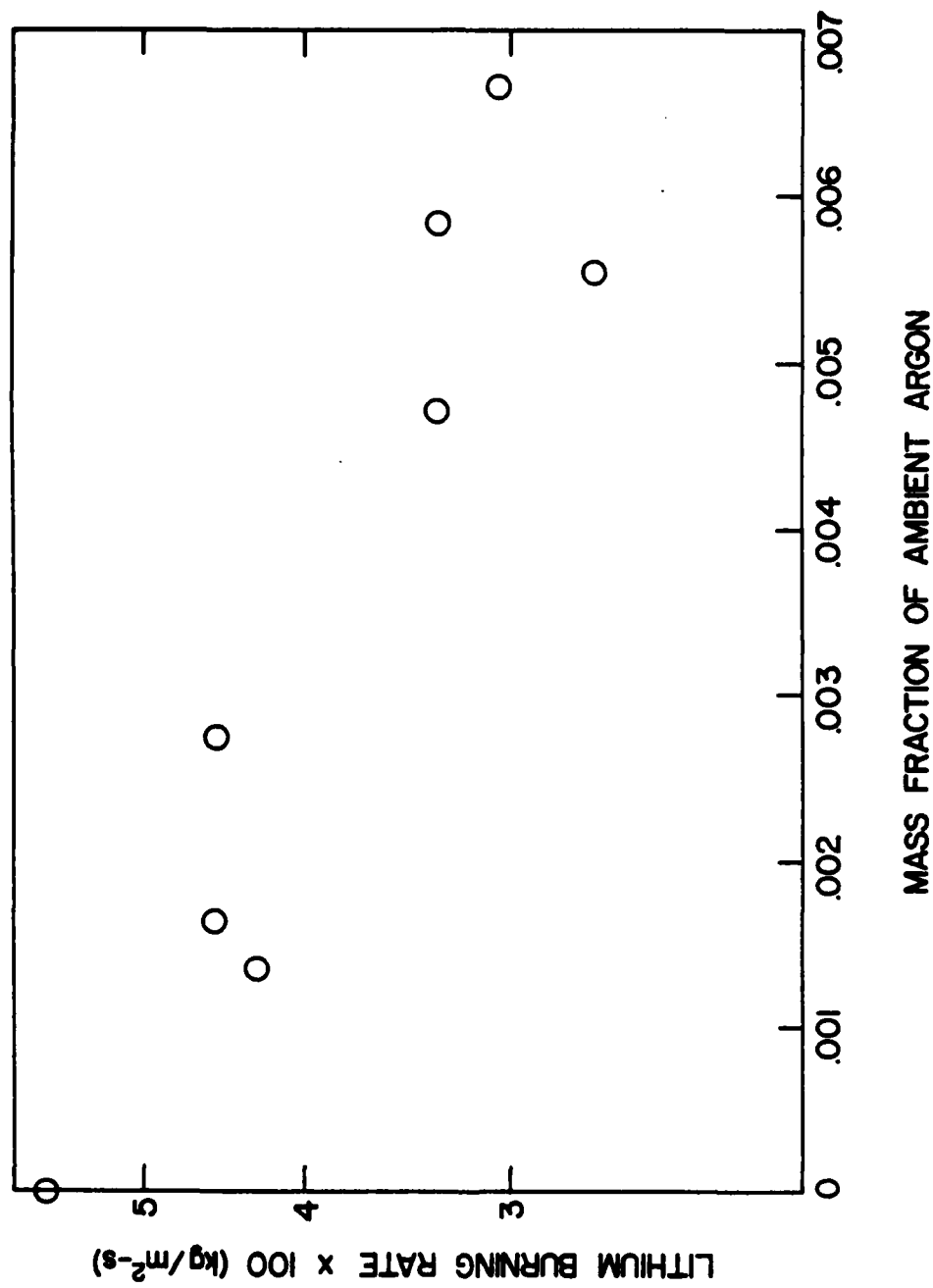


Figure 16 Effect of Argon Mass Fraction on Burning Rate at a
Constant Pressure of 13300 Pa

CHAPTER IV

APPARATUS AND PROCEDURE FOR WICK-TYPE COMBUSTOR TESTS

A series of tests was run in laboratory-size wick-type combustors to obtain more information about the combustion characteristics. The tests were specifically designed to determine the relationship between wick surface temperature and the pressure in the gas phase adjacent to the wick. Three combustor configurations were tested to analyze the effect of combustor length-to-diameter ratio and the effect of varying heat flux through the wick.

4.1 Apparatus

4.1.1 Wick-Type Combustor

The three combustors used for the wick-type combustor tests are shown schematically in Figures 17, 18 and 19. Tables 2, 3 and 4 summarize the designs of each of the combustors. Standard heat pipe design procedures (25, 26) were used to choose wire mesh sizes which would support enough capillary rise of lithium to ensure no chance of wick dry-off for each of the combustor configurations. The wick designs chosen were theoretically capable of pumping one to two orders of magnitude more fuel than the maximum flow rates required in these combustors. The wick was installed along the combustor wall and spot-welded in place. As in standard heat-pipe practice, the finer mesh (see Table 2) was placed away from the wall, with the coarser mesh next to the wall. This yields maximum capillary rise from the finer mesh while reducing the flow resistance by use of the coarser mesh.

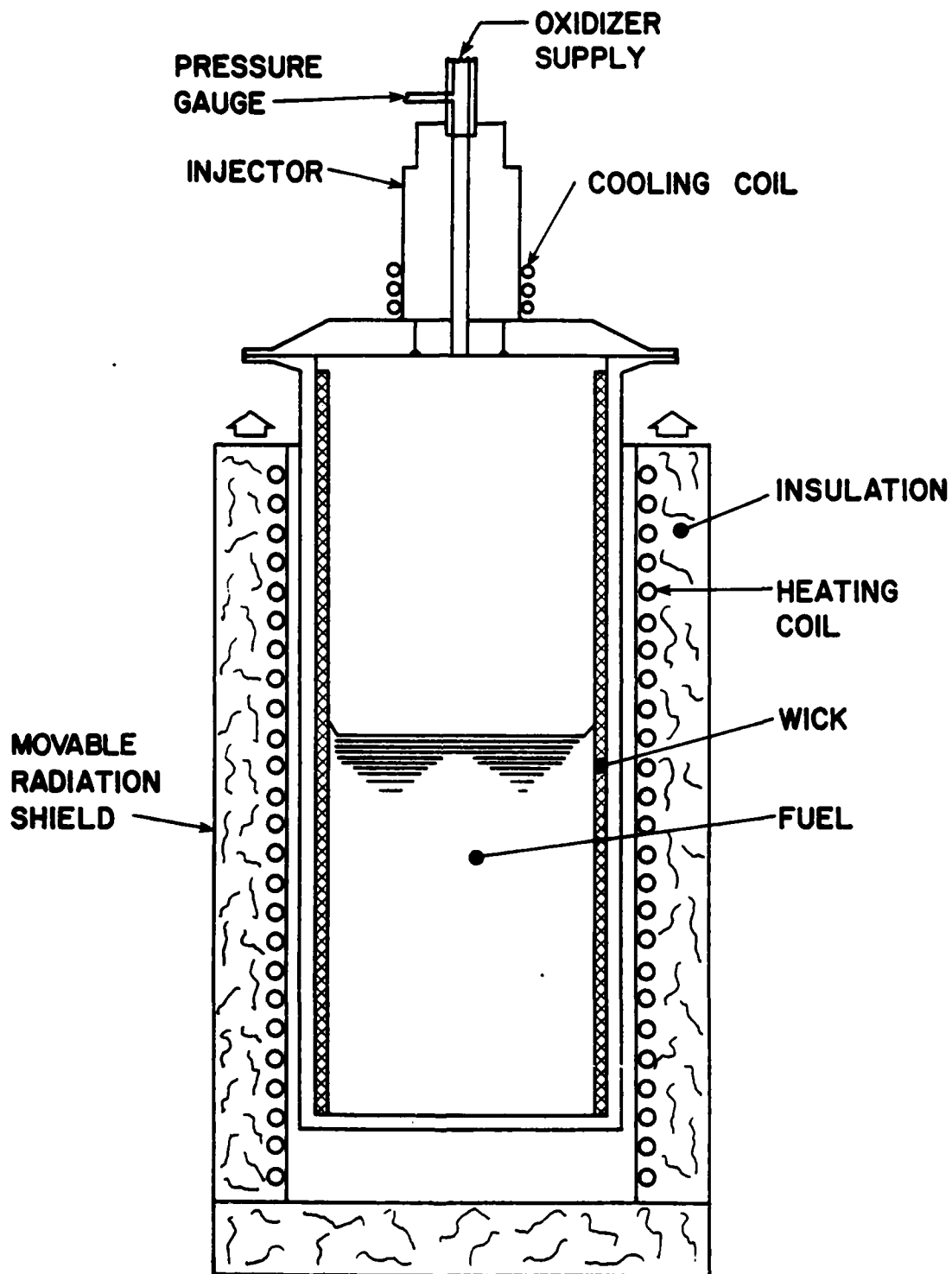


Figure 17 Schematic of Preliminary Wick-Type Combustor

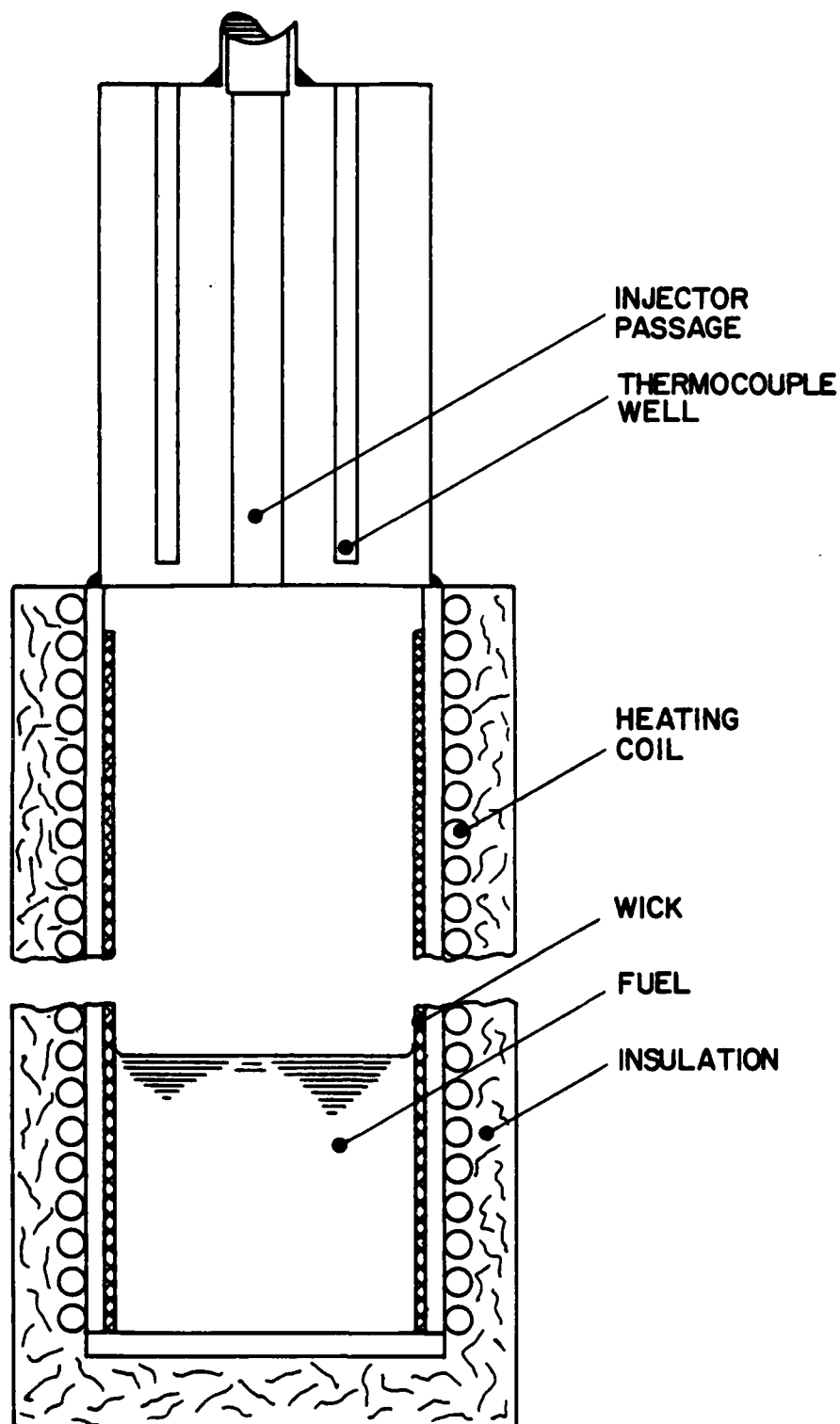


Figure 18 Schematic of Long Length-to-Diameter Wick-Type Combustor

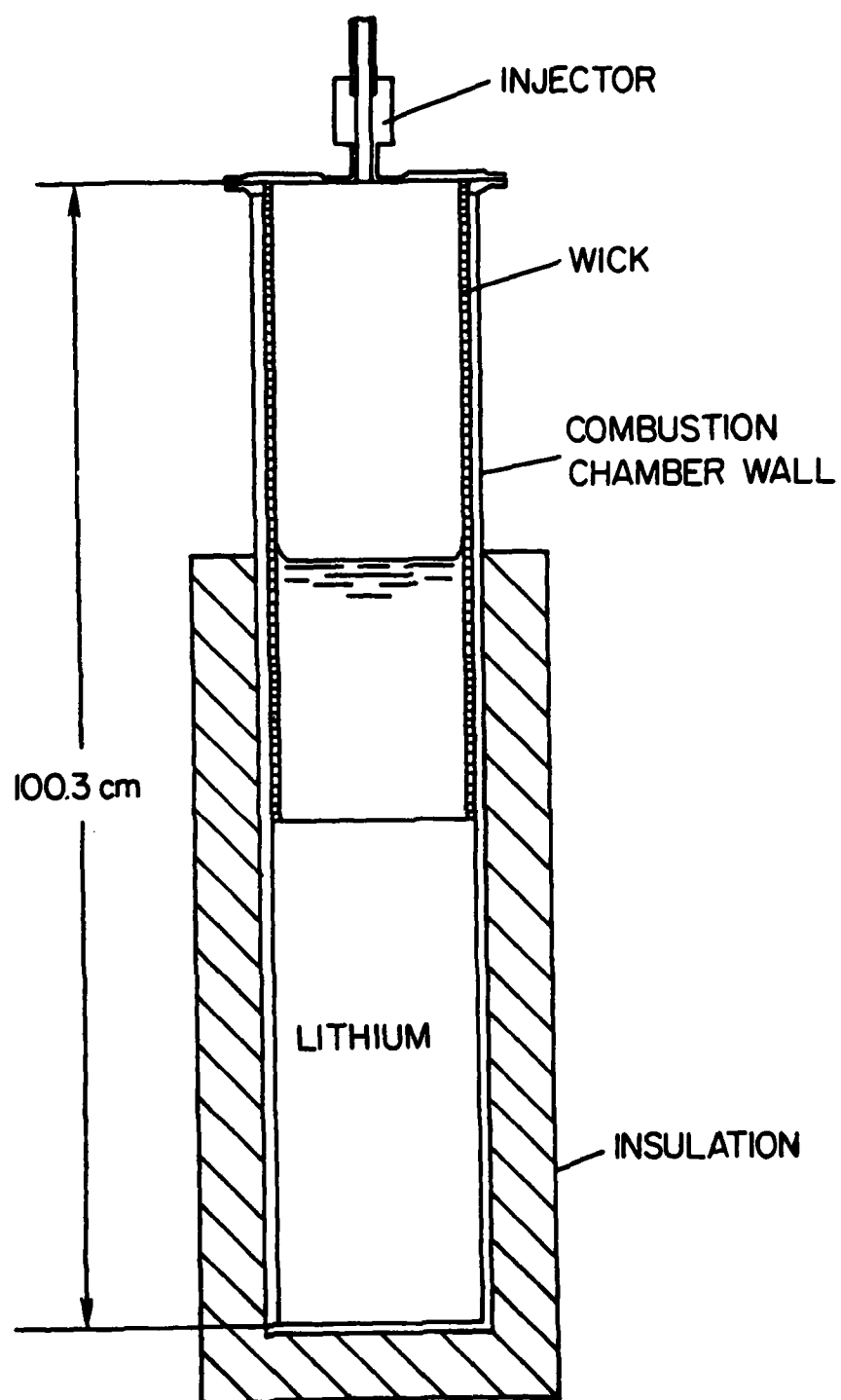


Figure 19 Schematic of Large Wick-Type Combustor

Table 2

Design Summary of Preliminary Wick-Type Combustor

I. Combustor

Material: Type 316 Stainless Steel
Dimensions: 101 mm I.D. x 110 mm O.D. x 233 mm long interior
Head: 12.7 mm plate

II. Wick

Material: Type 316 Stainless Steel Woven Wire Cloth
Composition: 1 layer 630 wires per meter - .58 mm diameter wire
1 layer 1575 wires per meter - .29 mm diameter wire

III. Injector Body

Material: Nickel 200
Dimensions: 10.3 mm I.D. x 44.5 mm O.D. x 66.7 mm long

Table 3

Design Summary of Long Length-to-Diameter Wick-Type Combustor

I. Combustor

Material: Type 316 Stainless Steel

Dimensions: 43 mm I.D. x 48 mm O.D. x 514 mm long

II. Wick

Material: Type 316 Stainless Steel Woven Wire Cloth

Composition: 2 layers 3937 wires per meter - .114 mm
diameter wire

III. Injector Body

Material: Nickel 200

Dimensions: 5.5 mm I.D. x 44.5 O.D. x 66.7 mm long

Table 4

Design Summary of Large Wick-Type Combustor

I. Combustor

Material: Type 316 Stainless Steel

Dimensions: 154 mm I.D. x 168 O.D. x 1003 mm long

II. Wick

Material: Type 316 Stainless Steel Woven Wire Cloth

Composition: 2 layers 3937 wires per meter - .114 mm diameter wire

III. Injector Body

Material: Nickel 200

Dimensions: 5.5 mm I.D. x 19 mm O.D. x 25 mm long

The injector was fabricated from Nickel 200 rod. Nickel 200 was chosen because it has the highest resistance to corrosion by fluorine of all common high-temperature metals (7). Two thermocouple wells were provided into the injector interior in order to monitor temperatures near the injector face.

The combustion process proceeded in a manner similar to that described in Section 2.2.1. Capillary action maintained a supply of fuel to all portions of the wick. The lithium evaporated from the wick into the ullage volume where the reaction with the oxidizer occurred. The heat of reaction was removed by radiative and convective heat transfer from the combustor walls.

The movable radiation shield used in the first combustor tests provided a means of varying the heat flux through the wick by varying the heat load to the combustor. Heat loads could be varied by about 10:1 if desired. Two 1500 W Ni-Chrome beaded heaters were installed in the radiation shield. These heaters were used to raise the combustor to ignition temperature. No movable shield was used for the other two combustors. These combustors were designed to be run at two conditions only--maximum heat flux and minimum heat flux. The heaters used for these tests were wrapped directly on the outside wall of the combustor.

4.1.2 Gas Supply System

A schematic of the gas supply system used for the wick-type combustor tests is presented in Figure 20. The entire system, including the combustor, was welded or brazed wherever possible to reduce the chance of leakage. Those joints which could not be welded or brazed were coated with a silicone-rubber sealant. A VEECO MS-90AB Leak

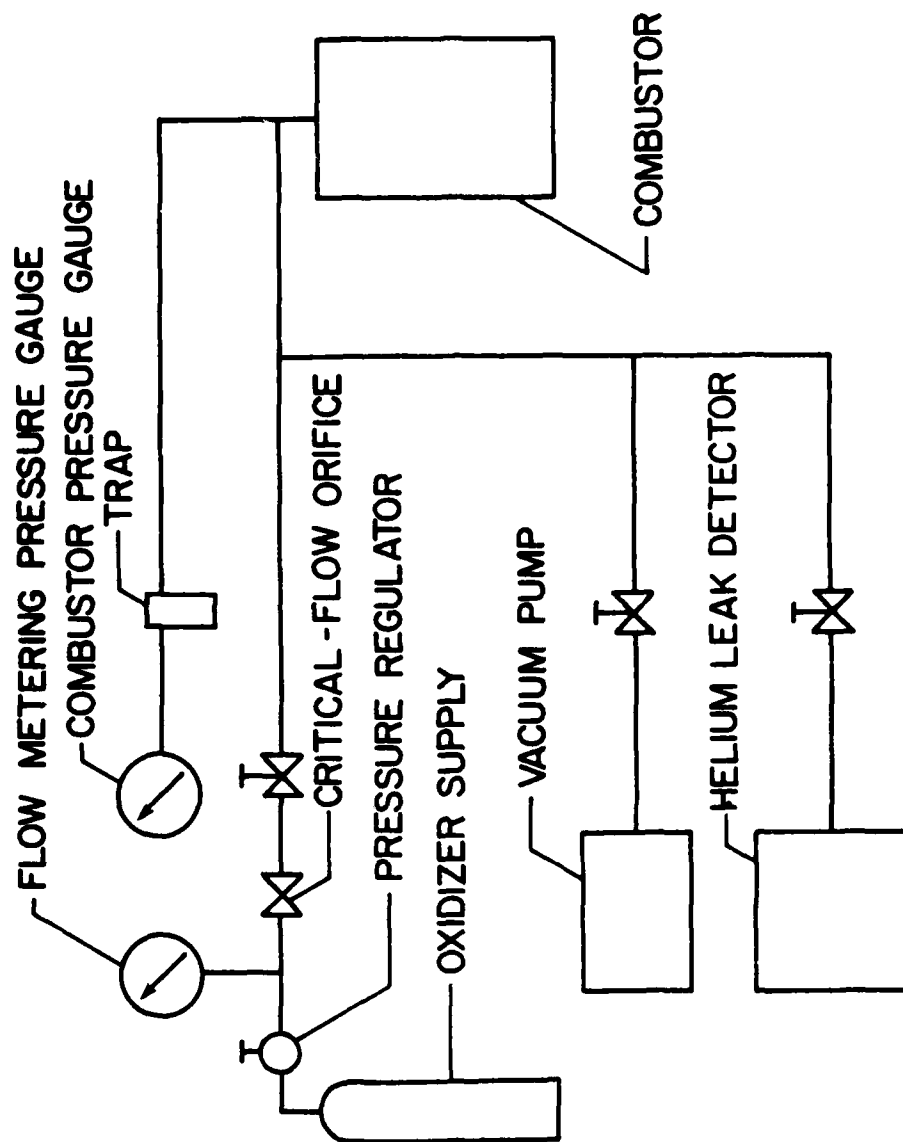


Figure 20 Schematic of Gas Supply System for Wick-Type Combustor Tests

Detector was used to helium leak-check the entire system before each test. The maximum leak rate for all tests, except one, ranged from 0.35×10^{-8} to 10^{-10} standard cc/second of helium. The leak rate for the one exception, WCT - 3, was 0.3×10^{-6} standard cc/second of helium.

4.1.3 Instrumentation

4.1.3.1 Flow Measurement

The oxidizer flow to the system was measured using a calibrated critical-flow orifice-pressure regulator combination. The pressure regulator was a Matheson Model 9 two-stage regulator with 1.6×10^5 - 1.7×10^6 Pa (10-250 psig) output capacity. The pressure upstream of the critical-flow orifice was measured with a Matheson Maxisafe test gauge with 1×10^5 - 2.8×10^6 Pa (0-400 psig) range and 13800 Pa (2 psi) divisions. For the final tests, 10 and 13 the upstream pressure was measured with a Heise 0- 2.1×10^6 Pa (0-300 psia) gauge with 3450 Pa (0.5 psi) divisions. The orifice was calibrated with a Precision Scientific Wet-Test Meter (0.0028 cubic meters/revolution).

4.1.3.2 Temperature Measurement

Temperatures were measured using 26 gauge chromel-alumel (A.N.S.I. Type K) thermocouple wire manufactured by the Thermo-electric Company (G/G-26-K). The wire is manufactured to American National Standards Institute tolerances— $\pm 0.75\%$ in the temperature range of interest. Two thermocouples were placed in the thermocouple wells located in the injector, while an additional 34 thermocouples were spot-welded to the combustor head and side walls. The thermocouples placed on the combustor wall were located in pairs on opposite sides of the combustor at the same axial distance from the injector.

Thermocouple output was recorded on three Leeds and Northrup Speedomax H Type S Multipoint Recorders, using a strip-chart-speed of 1 inch per minute. All the recorders were set for multipoint recording, meaning that each thermocouple was recorded every 18 seconds. The thermocouple extension cables and recorders were calibrated in the same manner as described in Section 2.2.4.

4.1.3.3 Pressure Measurement

Combustor pressures were measured by a Wallace and Tiernan Model FA-129, 0-340 kPa (0-100 in. Hg) absolute pressure gauge with ± 340 Pa (0.1 in. Hg) accuracy. For the last two tests, the combustor was measured by a Miriam absolute pressure mercury manometer with 1 mm divisions. The pressure measurement was made at the inlet to the injector. The bulk flow of the oxidizer prevents lithium vapor and product vapor from diffusing back towards the pressure tap and either clogging the line or damaging the instrument. The oxidizer flows used during the wick-type combustor tests (less than 1.62 kg/hr) were sufficiently low that the pressure drop through the injector was negligible (less than 17 Pa). Therefore, within the accuracy of the instrumentation, the injector pressure was equal to the combustor pressure.

4.1.4 Reactants

The reactants used for the wick-type combustor tests were the same as employed during the lithium combustion tests. No argon was used during the wick-type combustor tests except as a cover gas during periods of storage between tests.

4.2 Procedure

4.2.1 Combustor Preparation

Prior to a test being run in the wick-type combustors, the wick was installed in the combustor as indicated in Section 4.1.1. Both the interior of the combustor and the injector were then rinsed thoroughly with reagent grade methanol. The lithium was cleaned and weighed in a vacuum/glove box under an argon atmosphere. The combustor was then placed in the vacuum/glove box and heated to 525 K to melt the lithium into the bottom of the combustor. The loaded combustor was then allowed to cool.

After the combustor had cooled to room temperature, the injector (or head, for the first and last combustors) was welded in place. A continuous argon purge was maintained into the combustor during welding to avoid excessive contamination of the lithium. The combustor was then immediately evacuated to remove any air which might have entered.

The next process was a combination of de-gassing the fuel and pre-wetting the wick. The combustor was heated under continuous vacuum pumping to about 850 K. The pump was removed and the combustor was heated to 1100 K to wet the wick. The wetting temperature for these tests was higher than the temperature required for the lithium burning rate tests because there was no practical method of sloshing the fuel without badly clogging the injector passage. The vacuum pump was restarted when the combustor had cooled to less than 850 K. After the combustor had cooled to room temperature, the injector line was checked for blockages caused by condensed lithium vapor. Small plugs of condensed lithium had to be removed approximately half of the time.

After all lines were checked and cleaned, the combustor was installed and the system was evacuated. At this point the system was helium leak-checked to the levels indicated in Section 4.1.2.

4.2.2 Test Procedure

A test was begun by heating the combustor under continuous vacuum to about 850 K. The vacuum pump was then shut off, while the heaters were left on. A small amount of oxidizer was bled into the combustor so that combustor pressure was maintained in the range of 6750-20250 Pa. Ignition usually occurred when the combustor wall temperatures were about 950-1000 K. Ignition was generally indicated by a sharp increase in wall temperature (50-100 K in less than a minute) combined with a sudden decrease in combustor pressure. Ignition is defined as that point where an oxidizer flow sufficient to maintain temperature causes no increase in combustor pressure. Oxidizer flow, combustor pressure, and system temperatures were recorded from the ignition point to system shut-down. System shut-down was accomplished by terminating the oxidizer flow and allowing the combustor to cool to room temperature.

System temperatures were controlled in two ways: oxidizer flow to the system, and radiative heat transfer from the system. The system was generally operated to obtain a "saw-tooth" profile in combustor wall temperatures. A slow, steady increase in temperature was followed by a sudden temperature decrease and then repeated. The sudden temperature decreases were obtained by the removal of insulation (or lowering the radiation shield) for a short time, usually 2-3 minutes. Reducing oxidizer flow in order to lower temperatures was done only if a slow temperature decrease or slight temperature adjustment was desired.

Experience showed that a sharp decrease in oxidizer flow could result in an injector clog if the injector were hot enough. During the wick-type combustor tests, it was seen that the lithium would wet the smooth surface of the head when the temperature on the head reached 1150-1200 K. This caused no injector problems unless the oxidizer flow was reduced quickly. The sudden decrease in momentum in the oxidizer flow appeared to permit the lithium to wick into the injector passage and clog it shut. No injector clogging was ever encountered other than in this manner.

This result is significant with respect to the pressure data obtained. A gradual clogging of the injector passage could result in the passage necking down to the point where the oxidizer flow could become choked, invalidating the pressure data. An analysis was performed to determine the minimum flow passage allowable for each test to maintain unchoked oxidizer flow. Inspection of the injector after each test revealed that this phenomenon was never encountered.

4.2.3 Post-Test Procedure

After a test was completed and the combustor had cooled to room temperature, the combustor was cut open for inspection. After all the tests, small droplets of product were found frozen into the wick, indicating that product condenses on the wick structure in an internal wick arrangement, similar to the behavior seen on the external wick surface used in the lithium burning rate tests.

After post-test inspection was completed, the combustor was heated under an argon purge to about 1100 K and the product-fuel bath mixture was poured out into a stainless steel tray. Any remaining lithium was reacted away in water and the remaining product was removed

mechanically. A final inspection of the wick was made after the clean-out was completed. The wick was replaced if any signs of deterioration were found.

CHAPTER V

RESULTS OF THE WICK-TYPE COMBUSTOR TESTS

Appendix C is a summary of the data from the wick-type combustor tests. The average wall heat flux is calculated as the total energy release rate, given by the oxidizer flow rate and the energy release of the reaction per unit mass of oxidizer (4.77 kW-hr/kg of oxidizer from Reference [27]), divided by the area of the wick above the surface of the bath. The wick temperature is calculated from the measured wall temperature plus the temperature drop through the liquid-filled wick and the combustor wall. The temperature drop is calculated using an average wall heat flux and the thermal resistances of the wick (28) and the wall. The average lithium reaction rate is calculated by dividing the oxidizer flow rate by the stoichiometry parameter (2.63 kg of oxidizer/kg of lithium) and the area of the wick above the liquid surface.

Figure 21 is a presentation of the data obtained from a typical test--WCT - 5. The plots show combustor pressure, wall temperature, and average wall heat flux. The sharp decrease in combustor pressure which occurs at ignition can be seen at the beginning of the run. Once the excess oxidizer is burned, the combustor pressure and the wall temperature show a definite relationship, increasing and decreasing together. The pressure rise at the end of the run can be attributed to complete consumption of the lithium.

It is of interest to examine the relationship between the combustor pressure and the temperature at the wick surface in greater

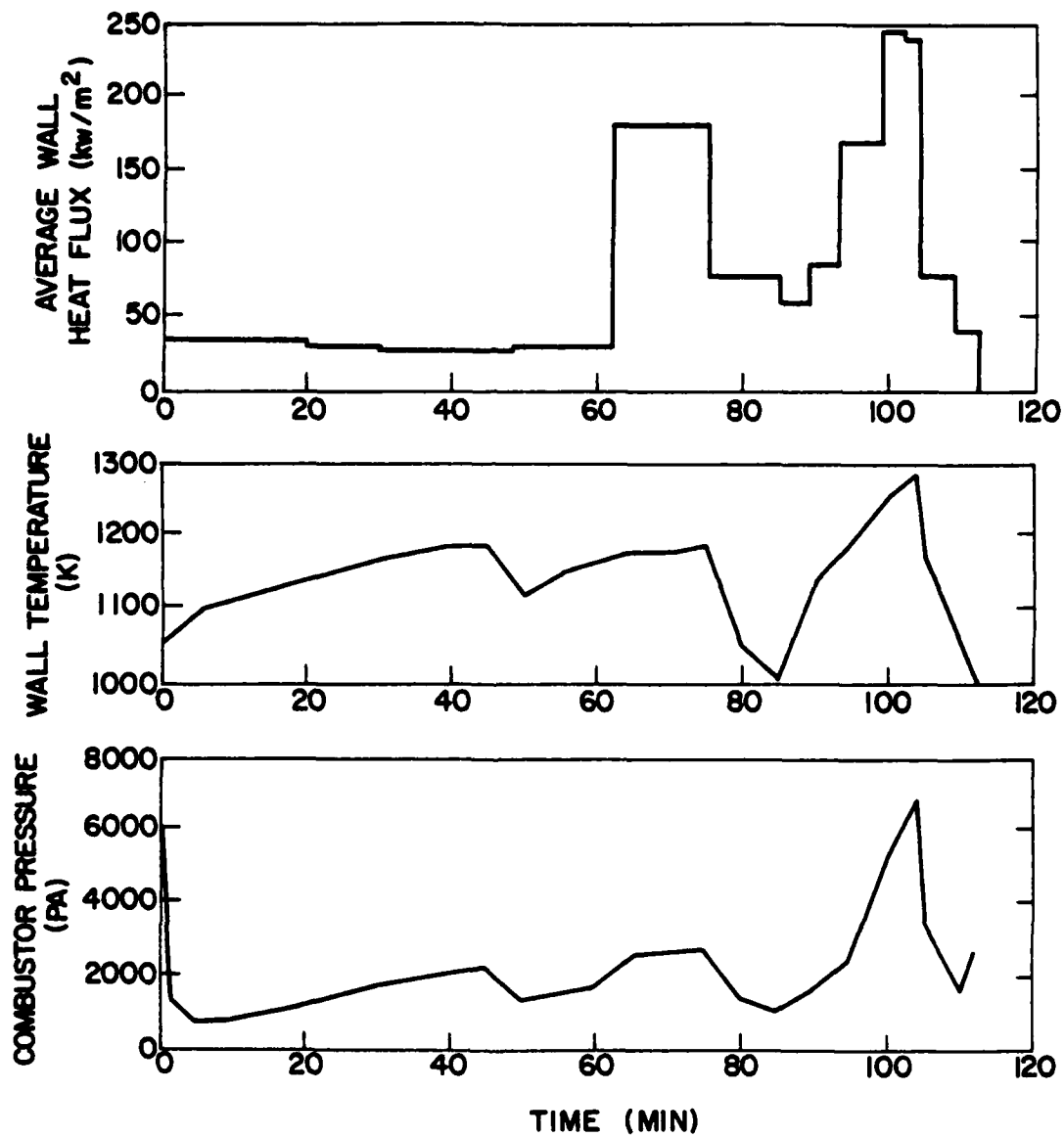


Figure 21 Data from Typical Wick-Type Combustor Test

detail. For the combustion rates observed during both the burning rate tests and the wick-type combustor tests, gas velocities normal to the surface are relatively low, and the pressure in this region is nearly constant. Consequently, pressure variations normal to the wick surface are negligible, similar to an aerodynamic boundary layer. Therefore, the pressure measured in the vacuum chamber during the burning rate tests and the pressure measured within the combustor during the wick-type combustor tests can be taken to be equal to the gas pressure at the wick surface.

If the reaction is occurring near the liquid surface, the pressure at the surface must be comprised of the partial pressure of the lithium vapor, including the monomer and all polymers (29); the partial pressure of the product species, since condensed product was observed on the wick; the partial pressure of the sulfur hexafluoride; and the partial pressures of any reaction intermediates. However, if the reaction is primarily occurring some distance away from the liquid surface, as is the case for a diffusion flame, the concentration of oxidizer and reaction intermediates at the surface is relatively low, and the pressure at the liquid surface would be comprised of the partial pressures of the lithium and the product species only.

The present system is rather unique since condensed phases of both the lithium and the products are observed at the surface. In these circumstances, the assumption of thermodynamic equilibrium in the region near the surface implies that the pressure at the surface would be the sum of the vapor pressures of all these species. Therefore, information on whether the reaction is occurring at the

fuel surface, or some distance from the surface, can be determined by comparing the sum of the predicted partial vapor pressures with the measured total pressure, as a function of the wick temperature.

The thermodynamic analysis of Groff (27) for the lithium-lithium fluoride-lithium sulfide ternary system provides a means of predicting the total vapor pressure as a function of temperature. This analysis is relatively complete in that it allows for the presence of the polymeric species of lithium and lithium fluoride which are likely to exist (30, 31). A remaining problem is to determine the ratio of the concentration of lithium fluoride and its polymers to the concentration of lithium sulfide in the region near the surface. If a very thin diffusion flame is present in the gas phase, then the product species are produced in stoichiometric proportion (six moles of LiF for each mole of Li_2S) within the flame. However, differences in diffusion and condensation rates between the flame and the fuel surface could result in various proportions of the products at the surface. In order to avoid detailed analysis of all the possible diffusion and condensation processes, and keeping in mind that the present exercise is merely to establish whether substantial reaction is occurring at the liquid surface, the following range of possible conditions at the wick surface was considered.

1. Only lithium present at the wick surface.
2. Only lithium and lithium fluoride present at the wick surface.
3. Only lithium and lithium sulfide present at the wick surface.

4. Lithium and stoichiometric proportions of lithium fluoride and lithium sulfide present at the wick surface.

Table 5 summarizes the vapor-pressure predictions of all four cases as a function of temperature in the range of interest. The prediction for the case of pure lithium was taken from Davison (29), while the results for the other three cases were computed using the analyses of Groff (27, 32). Groff's model calculates the vapor pressure of the mixtures assuming a saturated solution of the lithium and the appropriate condensed products at the surface. It should be noted that the observation of condensed product on the liquid surface necessarily eliminates the first case as a viable model. However, this case does represent one bound on the various conditions possible at the wick surface. In fact, lithium vapor provides the major contribution for all cases shown in the table, and the values for the various product proportions are nearly the same.

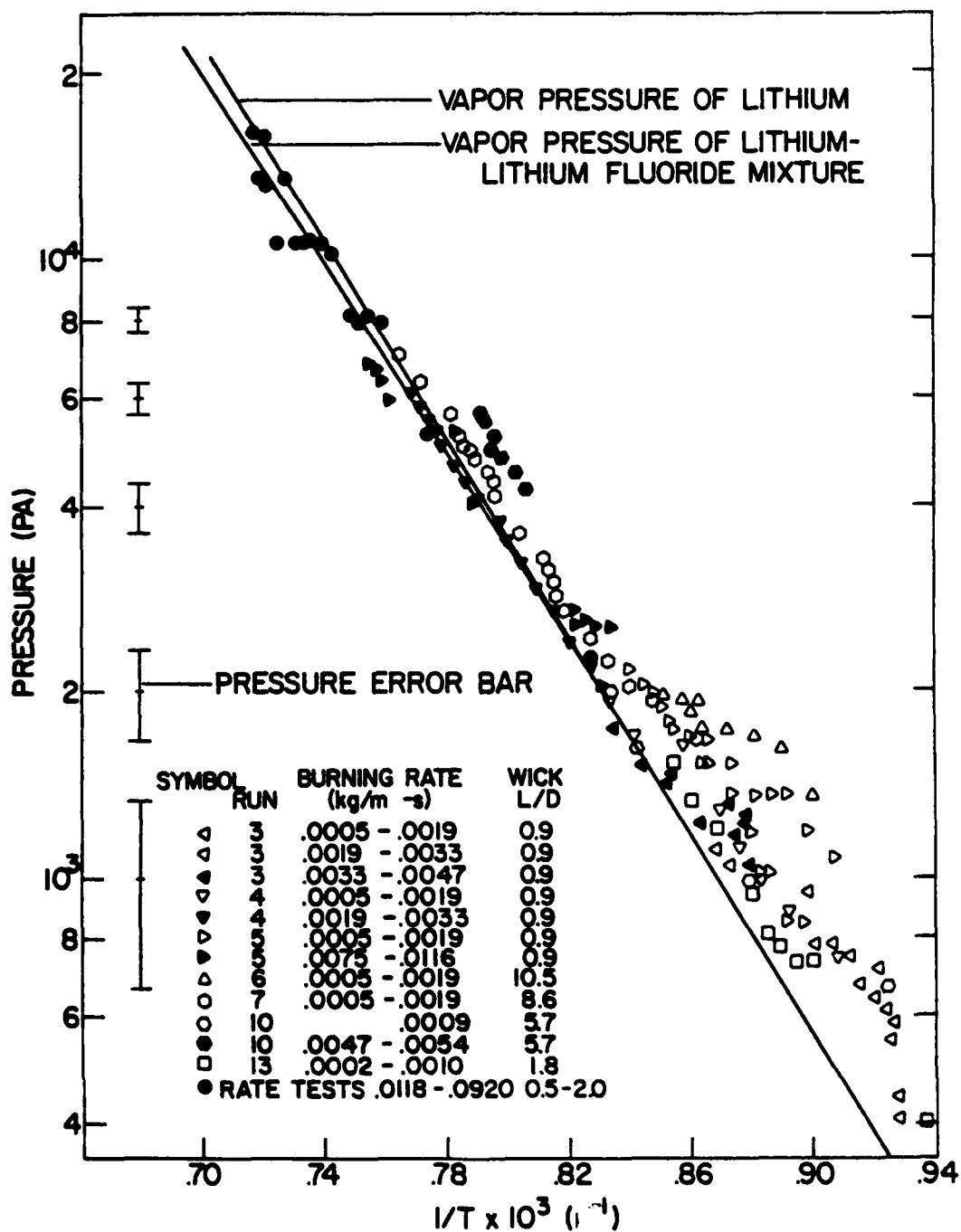
Figure 22 shows the pressure-temperature data obtained from both the wick-type combustor tests and the lithium burning rate tests. The measurements were made for various average rates of lithium reaction, in the range 1-330 kg/m²hr. A variety of wick geometries was also considered, represented by wick length-to-diameter ratios in the range 0.9-10.5

No data were obtained for wick temperatures less than 1066 K. There are two reasons for this. In the beginning of a test, the temperature increased from the ignition point to about 1075 K very rapidly. Wall temperatures usually exceeded 1100 K before the pressure decrease at ignition was completed. Therefore, good data could not be obtained during this transient period. Secondly, the behavior

Table 5

Comparison of Predicted Vapor Pressure of Delimiting Conditions at Wick Surface

Temperature (°K)	Vapor Pressure of Lithium (Pa)	Vapor Pressure of Lithium and Lithium Sulfide (Pa)	Vapor Pressure of Lithium and Lithium Fluoride (Pa)	Vapor Pressure of Ternary Mixture (Pa)
1140	873	871	866	873
1180	1516	1499	1489	1501
1200	1971	1940	1921	1940
1240	3246	3166	3121	3160
1280	5183	5007	4909	4984
1300	6480	6229	6088	6190
1340	9925	9451	9161	9349
1380	14831	13988	13419	13752
1400	17974	16871	16084	16524
1440	25981	24599	22683	23438
1480	36814	33906	31231	32505
1500	43518	39891	36325	37970



of the products precluded testing in this temperature range after the combustor had been operated for a time. If the combustor were allowed to cool below 1073 K (the solidification temperature of the products), some of the condensed product on the wick surface would freeze into the mesh. The frozen area would block the fuel flow, causing a local condition of wick dry-off. Any section of wick not continuously fed with lithium was immediately subjected to corrosion by the sulfur hexafluoride, causing a severe local "hot spot," and resulting in immediate termination of a test. The theoretical pressure-temperature relationships for pure lithium and for a lithium-lithium fluoride mixture are also shown in Figure 22, for comparison with the data. Examination of Table 5 indicates that the two cases that are plotted provide an upper and lower bound for all the predictions. The theoretical predictions are so close to each other and the data shows enough scatter to preclude any conclusion as to the actual composition at the surface. At higher temperatures (pressures), the experimental results generally follow the vapor pressure predictions. This suggests that the pressure at the liquid surface is only composed of the vapor pressures of the fuel and products. The absence of other components, oxidizer, etc., implies that reaction is not occurring at the liquid surface to an appreciable degree. The pressure-temperature data are also not strongly affected by the rate of reaction at high temperatures. If a surface reaction yielding condensed products were occurring, increases in reaction rate at a fixed surface temperature would require an increase in pressure, which was not observed.

In Figure 22, the data increasingly lie above the vapor pressure prediction as the temperature (pressure) is reduced. This could indicate

a more diffuse combustion process yielding increased amounts of reaction intermediates and sulfur hexafluoride right at the liquid surface. Experimental difficulties, however, could also be a contributing factor in this region. At low pressures, even small quantities of noncondensable contaminants present in the system could result in a pressure increase above the predicted vapor pressure, particularly in the small combustors. The relative accuracy of the pressure measurements is also reduced at low pressures, as indicated by the error bars shown in the figure. Experimental problems are also suggested by the fact that for the same surface temperature at low pressures, the measured pressure at low reaction rates is frequently higher than the measured pressure at high reaction rates; a surface reaction would imply the reverse of this behavior.

The data obtained from the test using the large wick-type combustor, Run 13, indicate that noncondensable contaminants are a significant cause of the deviation of the data from the vapor-pressure curve in the low temperature (pressure) range. For this test, the combustor was de-gassed for a period of about 8 hours prior to ignition. Temperatures during this period were slowly increased from 500 K to 810 K. This procedure, combined with the relatively large volume of the combustor, served to reduce the effect of noncondensable contaminants to a minimum.

While the data from Run 13 indicate that noncondensable contaminants are significant, the conclusions about the behavior of lithium-sulfur hexafluoride combustion do not change. It is still possible that a change from a vapor-phase reaction to a surface

reaction is occurring, although probably at lower pressures than indicated by the data from the smaller combustors.

CHAPTER VI

THEORETICAL CONSIDERATIONS

6.1 Introduction

Before choosing a mathematical model to analyze lithium-sulfur hexafluoride combustion, it is worth reviewing briefly what is known from the experimental results. The two characteristics which are important in the functioning of the model are the type of reaction and the behavior of the products. In order to understand the possible choices more closely, we shall separate these two areas.

The four possible general types of reaction are presented in Figure 23. The two extreme cases, a thin diffusion flame (Figure 23a) and a surface reaction (Figure 23d), provide the most straight-forward mathematical solutions. Each of the intermediate cases can be assumed to be represented by the appropriate extreme case, at least in a first approximation. Consequently, the choice of a mathematical model is then narrowed to two cases: a thin diffusion flame or a surface reaction.

Most of the evidence obtained for lithium-sulfur hexafluoride combustion suggests a vapor-phase reaction. The pressure-temperature relationship approximately follows the predicted values of vapor pressure, at least in the higher temperature (pressure) range. Observation of the combustion process (Figures 10 and 11) indicates a fairly thick luminous zone and large amounts of particulate products in the gas phase--sort of a product "smoke." These two characteristics, combined with relatively large burning rates, coincide with the

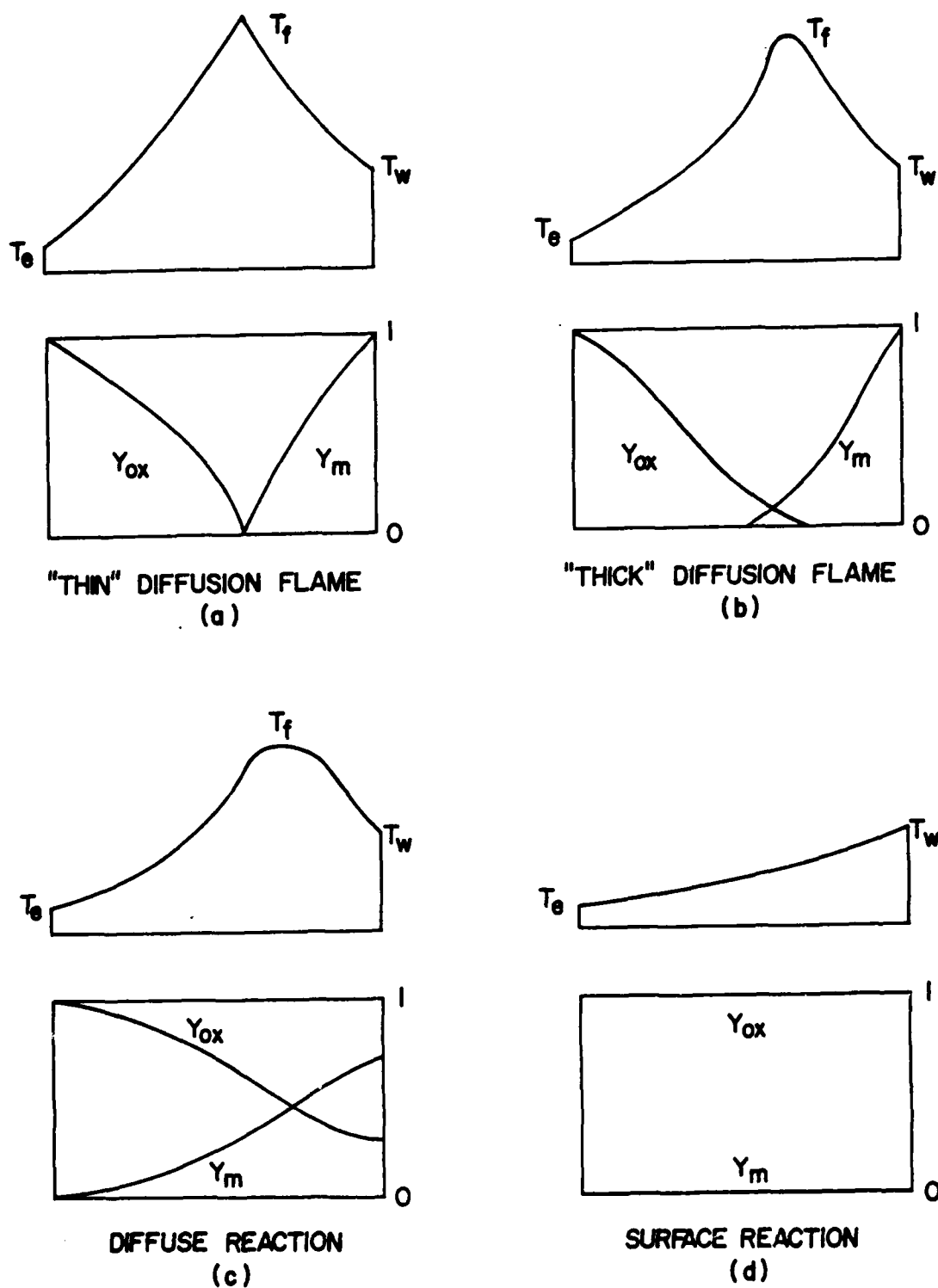


Figure 23 Schematic of Possible Flame Structures for Lithium-Sulfur Hexafluoride

characteristics described by Markstein as indicative of vapor-phase combustion of metals with oxygen (33). Although there are differences between the present study and the work of Markstein, it is reasonable that similar criteria can be used. Brzustowski and Glassman (34) have concluded that a necessary, but not sufficient, condition for vapor-phase combustion is that the boiling point of the products exceed the boiling point of the metal, which is the case in the present study. Finally, the results seen in Figures 12, 13 and 15 indicate that laminar, free convective processes are significant--again pointing to a vapor-phase reaction. However, the behavior shown in Figure 14, concerning the strong effect of pressure on lithium burning rate, is sufficiently unusual, compared to the known behavior of diffusion flames, to preclude a definite conclusion based on experimental observation, that the reaction is occurring entirely in the vapor phase. Nonetheless, a simple model based on a diffusion flame is justifiable in light of what has been seen, as a first step in the analysis of this process.

The behavior of the products presents another area of choice for the model. The products can be assumed to remain as a vapor at all times or to condense in some manner. If the products are assumed to condense, there are a number of choices as models, including:

- (a) all products condense in the flame zone (11, 12, 18);
- (b) some products condense in the flame zone and the remainder condense at infinity or at the fuel surface (13, 15-17);
- (c) products condense only at two condensation fronts, one between the flame and the fuel surface and one outside the flame zone;
- (d) products condense according to equilibrium condensation.

No-condensation models are used where the products are known to remain as a vapor (e.g., typical hydrocarbon combustion), or where condensation of the products can be neglected (e.g., References [35 and 36]). Because of uncertainties in the physical properties for combustion processes, no-condensation models can often provide reasonable estimates of burning rates despite the inherent lack of accuracy in the assumptions.

A brief review of the thermodynamics of the combustion process will provide justification for eliminating one of the condensation models--that of product condensing only in the reaction zone. If a gas-phase reaction is occurring, as in Figure 23a, then the temperature at the flame is the maximum temperature in the boundary layer. Therefore, if the flame temperature is above the boiling point of the products, (for example 1726 K at 13300 Pa), no condensed products can exist in the flame zone. From the work of Avery and Faeth (37), the minimum flame temperature is the saturated vapor temperature of the products at the total pressure of the boundary layer. However, we also know from Avery (9) that the actual flame temperature is on the order of 5000 K if lithium fluoride is the only product. The adiabatic flame temperature of the lithium-sulfur hexafluoride system, reacting according to Equation (1.2), is given in Table 6, assuming the lithium enters at the boiling temperature of the ternary mixture (27) and the oxidizer enters at 298 K. Note that the results are on the same order of magnitude with Avery's results. Obviously, even accounting for dissociation of the products would not yield sufficiently reduced flame temperatures to cause product to condense in the flame zone.

Table 6

Adiabatic Flame Temperature of Lithium-Sulfur Hexafluoride Combustion

Pressure (Pa)	T_w (K)	T_f (K)
2650	1226	4501
4000	1261	4528
5300	1287	4547
6650	1308	4563
7950	1326	4577
9300	1341	4588
10650	1355	4599
11950	1367	4608
13300	1378	4617

The choice of flame temperature only affects the mean transport properties in each region of the boundary layer. Since a complete flame temperature calculation was not undertaken, the no-condensation model was calculated using first the adiabatic flame temperature and then the saturated vapor pressure of the products (32). The intent is merely to provide an upper and lower bound on the predicted burning rates. Obviously, the lower case has no meaning in the condensation-front model. Consequently, only the adiabatic flame temperature will be used in that model.

The complexities introduced by the mathematical solution of a complete equilibrium model (case d) preclude its choice for the present study. Such a model of lithium-sulfur hexafluoride combustion

would necessarily include: dissociation and polymerization of the products; heat transfer from the flame, particularly radiation; effect of condensation on the temperature profiles; multi-component diffusion processes; and two-dimensional effects to account for the gravitationally-induced flow of the condensed products (i.e., buoyancy and settling). Obviously, this involves a far more difficult analysis than can be pursued at present, owing in part to the lack of precise thermodynamic data for lithium sulfide.

Consequently, a reasonable approach is to assume that the products condense in the boundary layer at two fronts, one located between the wick and the flame, and one located outside the flame. Such a model should provide useful insight into the behavior of the lithium-sulfur hexafluoride system and the effects of condensation without becoming unduly tangled in computational complexity.

The theoretical analysis of the present study will be divided into two parts. A no-condensation analysis will be performed to check its applicability to the present system and to provide a base-line comparison with the data. A condensation-front analysis will be performed to account for the effects of product condensation. From Rosner's work (12) we know that accounting for condensation can cause up to a four-fold increase in the predicted burning rate under some conditions. The condensation-front model will provide information as to the potential effect of condensation in the present system without becoming involved in extensive computations that would require thermodynamic and transport properties that are only poorly known for the present reactant system. Discussion and comparison of the two models will be undertaken in the final section of the chapter. This

will permit us to concentrate on each model and then compare the results more effectively.

Both models are film theory models which require some method of estimating δ_e , the total boundary layer thickness. The average value of δ_e was calculated from the formula suggested by Spalding (23) for laminar, free convective combustion from a vertical plane surface:

$$\delta_e = L / .555 (Gr_e Pr_e)^{1/4} \quad (6.1)$$

The transport properties were determined at the mean temperature in each region using the ideal gas law and the method for calculating binary diffusion coefficients developed by Wilke and Lee (38). Values of ϵ/K and σ (force constants for the Lennard-Jones [6-12] Potential) were obtained as follows: (a) argon and sulfur hexafluoride from Hirschfelder, Curtiss and Bird (39); (b) lithium, lithium fluoride and lithium sulfide from the empirical equations suggested by Hirschfelder, Bird and Spotz (40).

$$\frac{\epsilon}{K} = 1.15 T_b$$

$$\sigma = 1.18 V_b^{1/3}$$

The thermodynamic information for the estimates was obtained from JANAF Thermochemical Tables (30) for lithium and lithium fluoride and from Groff (27) for lithium sulfide.

The values of specific heat, thermal conductivity, and viscosity were obtained as follows:

- (a) all properties for sulfur hexafluoride from Brown (41)

- (b) viscosity and thermal conductivity for the lithium vapor and the mixture of product vapor were estimated using the Lennard-Jones (6-12) Potential according to the method outlined by Reid and Sherwood (42)
- (c) specific heat for lithium from Reference (30)
- (d) specific heat for the product from Reference (27).

The average value of viscosity for the mixture was calculated using the method developed by Wilke (43). The average value of thermal conductivity for the mixture was calculated using the Mason and Saxena (44) modification of the Wassiljewa method (45).

The accuracy of the values of viscosity and thermal conductivity obtained in part (b) can only be estimated. Theoretical values of viscosity generally are within 10% of experimental values for a wide variety of polar gases (42). Estimates of thermal conductivity are generally less accurate, with errors sometimes reaching 20%. By inference, it is not unreasonable to conclude that the values from part (b) may approach the same level of accuracy.

6.2 No-Condensation Model

6.2.1 Description and Assumptions

A schematic diagram of the no-condensation model is presented in Figure 24. The assumptions of the model can be summarized as follows:

1. The boundary layer (total thickness equal to δ_e) is divided into two regions by a flame zone of negligible thickness compared to δ_e . (The aerodynamic and concentration boundary layers are assumed to be of equal thickness.) The total pressure is constant throughout the

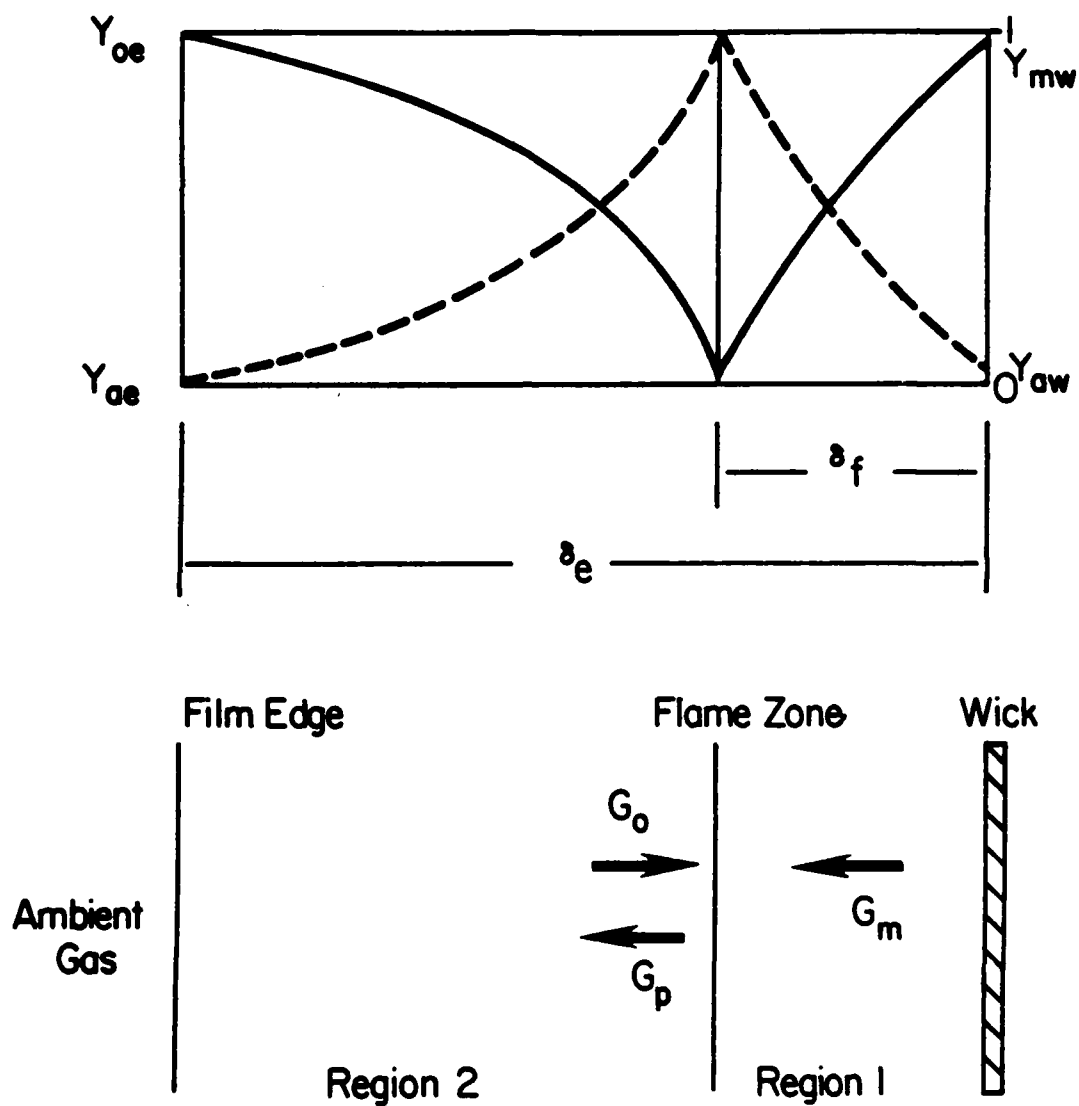


Figure 24 Schematic Diagram of No-Condensation Model

boundary layer and continuous binary diffusion laws are assumed to be valid. The gases in each region are assumed to obey the perfect gas law.

- (1a) Region 1 ($0 \leq y \leq \delta_f$) may contain only metal vapor, product vapor, and any inert diluent gas.
- (1b) Region 2 ($\delta_f \leq y \leq \delta_e$) may contain only oxidizer, product vapor, and any inert diluent gas.
- (2) The flame is assumed to be a thin diffusion flame (cf. Figure 23a), with the concentrations of fuel and oxidizer both equal to zero at the flame.
- (3) Immediately after ignition the liquid at the wick surface is assumed to be a saturated fuel-product solution and the product vapor in Region 1 is assumed to be stagnant. All products formed thereafter flow as a vapor through Region 2 in a direction perpendicular to the liquid surface. All flow parallel to the fuel surface is neglected.
- (4) The products are assumed to exist in stoichiometric proportion (six moles of LiF for each mole of Li_2S) and to behave as a single species with averaged properties throughout the boundary layer.
- (5) The transport properties are calculated by assuming that interactions between the oxidizer and products in Region 2 and the metal vapor and products in Region 1 are dominant. The effect of any superimposed inert gas is neglected as a result of the low ambient concentrations used in the present investigation.

(6) The vapor pressure of the metal at the wall is assumed to be equal to the equilibrium vapor pressure at the wall temperature, predicted by the ternary model of Groff (27), when no superimposed inert gas is present. When argon is present, the vapor pressure of the ternary mixture at the wall equals the total pressure minus the partial pressure of the argon at the wall. The conditions at the wall are then calculated from Groff's model (27).

(7) Transport properties are constant for each region.

6.2.2 Analysis

The analysis in both regions begins with the differential equation for a concentration boundary layer with both diffusion and convection (46)

$$G_y \frac{dY_k}{dy} - \frac{d}{dy} \left[\overline{\rho D} \frac{dY_k}{dy} \right] = \frac{dG_k}{dy} \quad (6.2)$$

G_y is the total mass flux in the region and is a constant for each region. The subscript k indicates the component of interest, i.e., the lithium or the oxidizer, depending on the region. Since the reaction is assumed to occur only at $y = \delta_f$, $\frac{dG_k}{dy} \equiv 0$ for both regions. Consequently, Equation (6.2) can be integrated across each region to yield:

$$G_y Y_k - (\overline{\rho D}) \frac{dY_k}{dy} = G_k = \text{constant} \quad (6.3)$$

In Region 1, this becomes:

$$G_m Y_m - (\overline{\rho D}) \frac{dY_m}{dy} = G_m \quad (6.4)$$

since the total mass flux in the region is comprised only of the metal vapor. The boundary conditions for Equation (6.4) are:

$$Y_m(0) = Y_{mw} \quad (6.5)$$

$$Y_m(\delta_f) = 0 \quad (6.6)$$

With these boundary conditions, Equation (6.4) can be integrated between the wick and the flame to yield:

$$G_m = \frac{(\overline{\rho D})_1}{\delta_f} \ln \left[\frac{1}{1 - Y_{mw}} \right] \quad (6.7)$$

In Region 2, Equation (6.2) becomes:

$$G_y Y_{ox} - (\overline{\rho D})_2 \frac{dY_{ox}}{dy} = G_{ox} \quad (6.8)$$

In this region, the total mass flux is comprised of both the flux of the product away from the flame and the flux of the oxidizer toward the flame. Recalling that*

$$G_y = -G_c \quad G_p = G_m \quad (6.9)$$

and

$$G_{ox} = -rG_m \quad (6.10)$$

Equation (6.8) can be rearranged to yield

$$-G_{ox} Y_{ox} / r - (\overline{\rho D})_2 \frac{dY_{ox}}{dy} = G_{ox} \quad (6.11)$$

*We might also note that the result obtained from Equation (6.9) can be obtained from a mass balance at the flame front. Since all flow is assumed to be in the y-direction only, we know that the total mass flux in Region 2 is equal to the total mass flux in Region 1.

The boundary conditions for Equation (6.11) are:

$$Y_{ox}(\delta_e) = Y_{oxe} \quad (6.12)$$

and

$$Y_{ox}(\delta_f) = 0 \quad (6.13)$$

Integrating Equation (6.11) and applying the boundary conditions results in the following expressions for the oxidizer mass flux:

$$G_{ox} = \frac{(\overline{\rho D})_2}{(\delta_e - \delta_f)} r \ln(1 + Y_{oxe}/r) \quad (6.14)$$

Substituting Equations (6.7) and (6.14) into Equation (6.10) results in the following expression for flame stand-off distance:

$$\frac{\delta_f}{\delta_e} = \left[1 + \frac{(\overline{\rho D})_2}{(\overline{\rho D})_1} \frac{\ln(1 + Y_{oxe}/r)}{\ln(1/(1 - Y_{mw}))} \right]^{-1} \quad (6.15)$$

We now recall that the vaporization rate of the metal into an inert environment can be expressed (cf. Equation [6.7]) as:

$$G_m^o \equiv \frac{(\overline{\rho D})_1}{\delta_e} \ln \left[\frac{1}{1 - Y_{mw}} \right] \quad (6.16)$$

Combining this expression with Equations (6.7) and (6.15) yields the desired prediction for the burning rate:

$$G_m = G_m^o \left[1 + \frac{(\overline{\rho D})_2}{(\overline{\rho D})_1} \frac{\ln(1 + Y_{oxe}/r)}{\ln(1/(1 - Y_{mw}))} \right] \quad (6.17)$$

6.2.3 Results

As indicated in Section 6.1, two sets of predictions were obtained for the no-condensation model, differing in the value of flame temperature used in estimating average physical properties. The

predicted values of lithium burning rates as a function of oxidizer pressure are compared with the data in Figure 25. The no-condensation model predicts that the burning rate is proportional to pressure to the four-tenths power, with the prediction based on a saturated flame having a slightly steeper slope than the prediction based on the adiabatic flame temperature. The data appear to show a similar trend for pressure below 8000 Pa. However, in the range of pressure above 8000 Pa, the measured burning rate increases much more rapidly than the predictions. It appears that the lithium-sulfur hexafluoride combustion process can be described by a diffusion flame model with no condensation at low pressure, but some other process, possibly the condensation of the products, must be included at higher pressures.

Figure 26 shows the variation in burning rate with wick length as predicted by the no-condensation model. As would be expected, the predicted average burning rate varies as $L^{-1/4}$. Since we have, from Equation (6.1):

$$\delta_e \propto L^{1/4} ,$$

it follows that the model will predict:

$$G_m \propto L^{-1/4} .$$

When argon is included in the analysis, the model requires additional information about the conditions at the wick. In particular, a relationship is required between the concentration of argon in the ambient gas and the wick. Some information on this relationship may be obtained from the values of wick temperature measured as a function of mass fraction of ambient argon (included in Table 10).

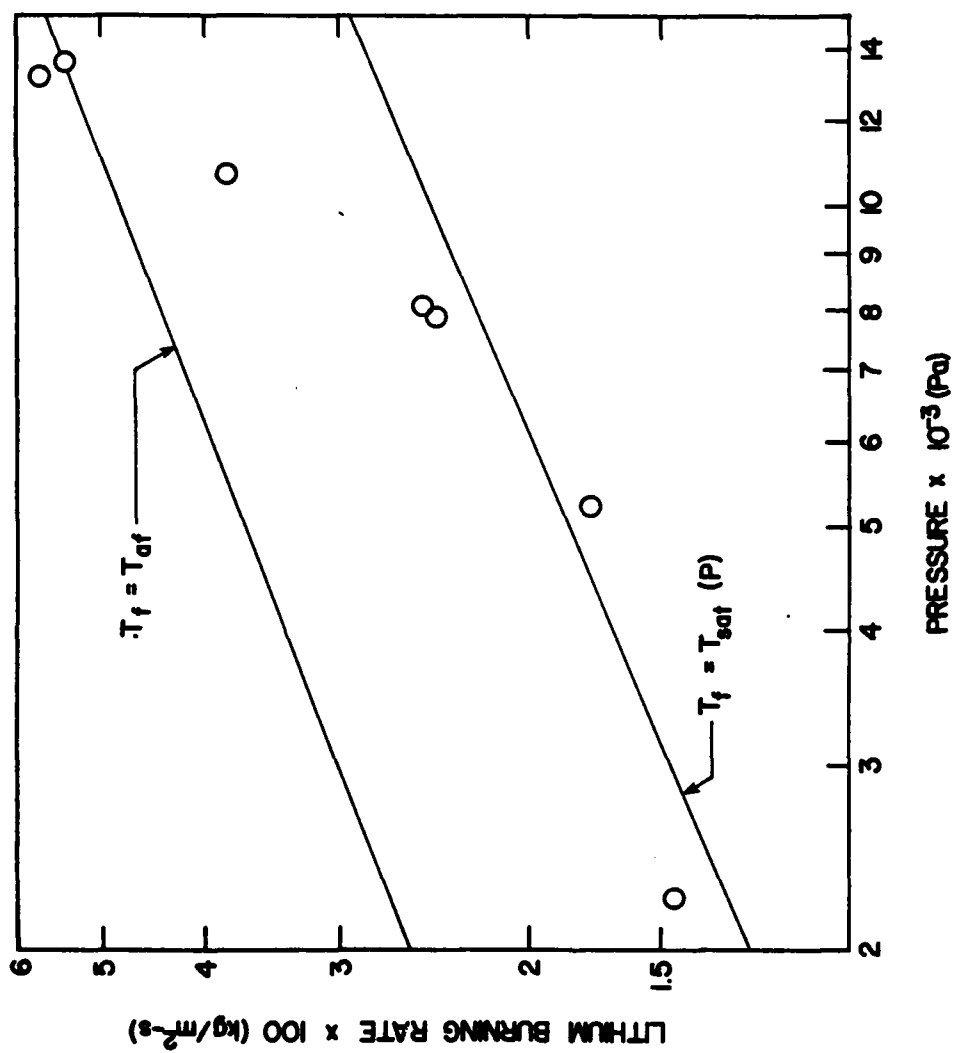


Figure 25 Prediction of the No-Condensation Model for the Effect of Pressure on the Lithium Burning Rate in Sulfur Hexafluoride for a Constant Wick Length (30 mm)

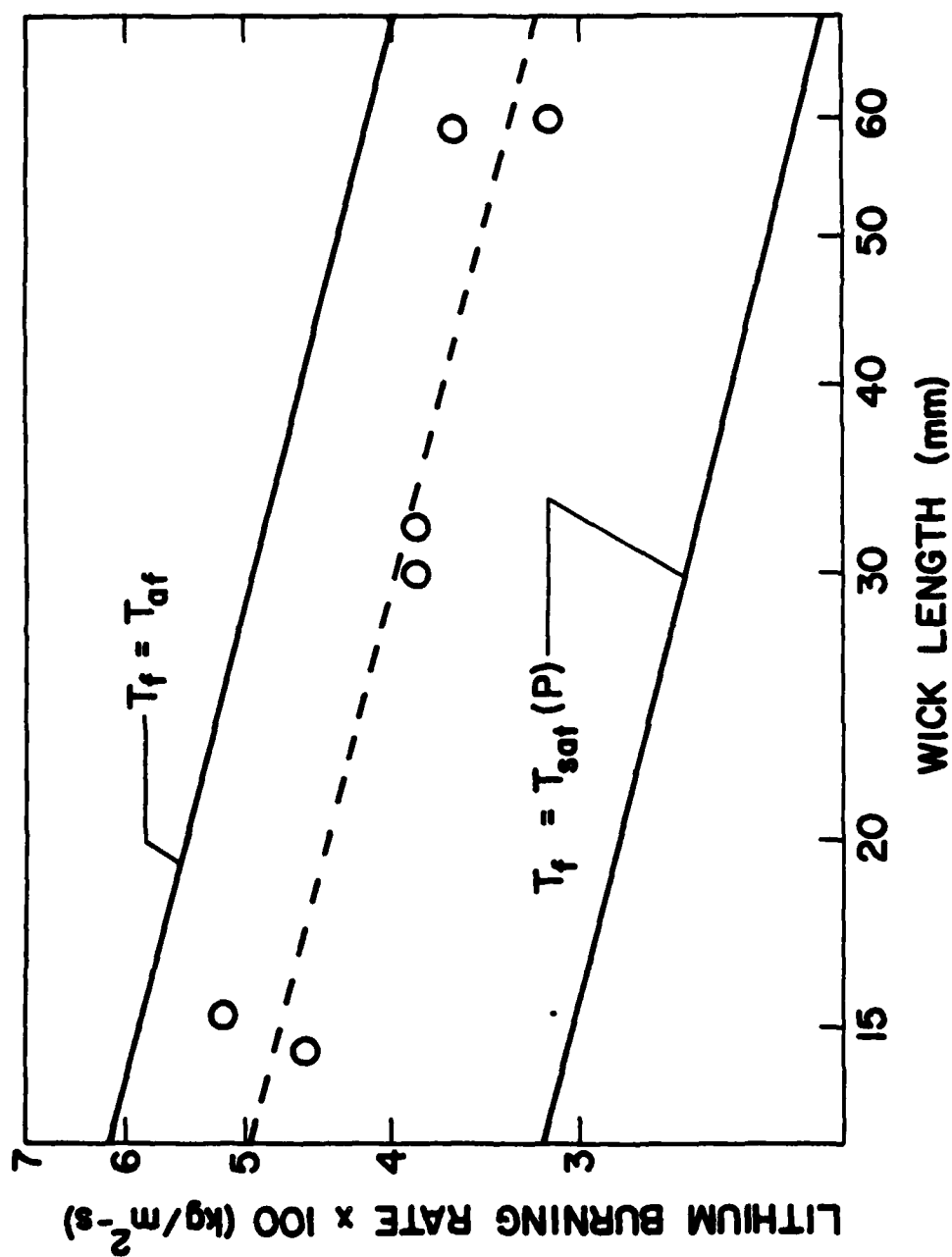


Figure 26 Prediction of the No-Condensation Model for the Effect of Wick Length on the Lithium Burning Rate in Sulfur Hexafluoride for a Constant Pressure (10750 Pa)

A plot of these values is presented in Figure 27, along with a least-squares linear regression of the points. (It is of interest to note that intercept of the regression agrees to within 0.03 K of Groff's prediction for total pressure of 13300 Pa.) (27). While the scatter is large compared to the total temperature change for the range of interest, the data provide the only means of obtaining the relationship between the concentrations of ambient argon and argon at the wick for this model. Examination of Table 7 illustrates the necessity of knowing the conditions at the wick. A small decrease in wick temperature causes a significant increase in argon concentration at the wick. (Since the vapor pressure of the ternary mixture is a direct function of the wick temperature, the argon will move to the wick to bring the pressure at the surface to the total pressure of the system). The significance of this effect can be found by referring to Equation (6.7). The mass flux of lithium is given by the expression:

$$G_m \propto \ln \left[\frac{1}{1 - Y_{mw}} \right]. \quad (6.18)$$

For the range of wick temperature shown in Table 7, the decrease of Y_{mw} results in a 33% decrease in the mass flux of the lithium. Obviously, there is not only a need to know the conditions at the wick, but these conditions must be known precisely if meaningful predictions of burning rates are to be made. As a consequence of the extreme sensitivity of the predictions to the wick temperature, it is unlikely that any method including the energy equation can predict wick temperatures with the accuracy required, even with no argon present. Once argon is present, the overall energy balance of the

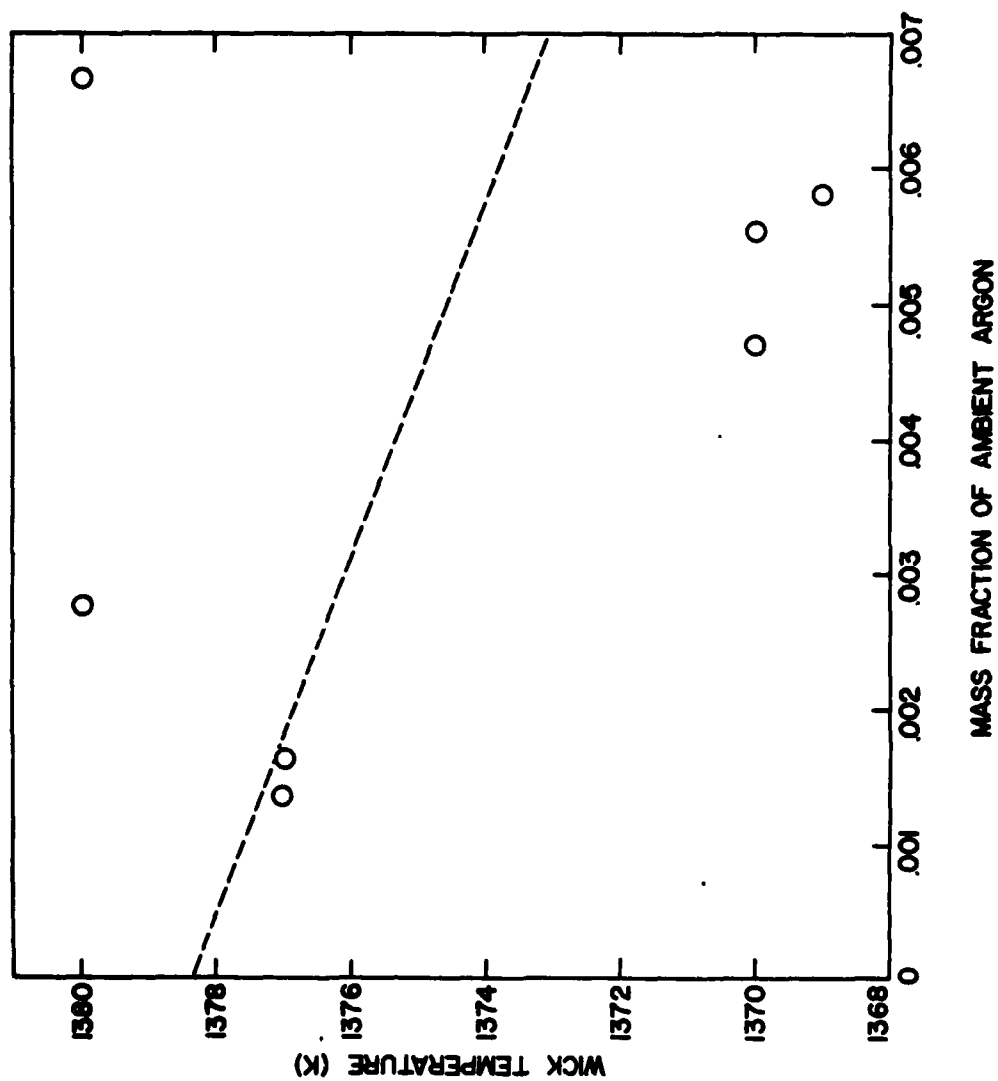


Figure 27 Measured Wall Temperature as a Function
of Mass Fraction of Ambient Argon at a
Constant Total Pressure (13300 Pa)

Table 7

Effect of Wick Temperature on Wick Conditions at a
Total Pressure of 13300 Pa

T_w (K)	Y_m (%)	Y_p (%)	Y_a (%)
1378.34	91.34	8.66	0.00
1378.12	90.37	8.56	1.07
1377.90	89.42	8.47	2.11
1377.45	87.57	8.27	4.16
1377.23	86.66	8.18	5.16
1377.01	85.78	8.09	6.13
1376.79	84.90	8.00	7.10
1376.35	83.20	7.83	8.97
1376.13	82.37	7.74	9.89
1375.57	80.34	7.53	12.13

system becomes much more complicated, resulting in even greater uncertainty. Therefore, for this simple model, it is reasonable to rely on the experimental measured values of wick temperatures and accept the degree of scatter.

The predictions of the no-condensation model for lithium-sulfur hexafluoride combustion in the presence of argon were obtained using a two-step process. For several given values of ambient argon concentration, a variety of wick temperatures were specified, yielding a family of curves of burning rate predictions, shown in Figure 28 as dashed lines. As can be seen, these curves are nearly horizontal, and are very weakly dependent on ambient argon concentration.

The final results are now obtained by combining these preliminary results with the information given in Figure 27. From Figure 27 we can obtain a value of ambient argon concentration corresponding to each value of wick temperature specified. This allows us to find a point along each dashed curve that represents the predicted lithium burning rate for the mass fraction of ambient argon obtained from Figure 27. The loci of these points, shown by solid lines in Figure 28, are the final prediction of the no-condensation model for lithium burning in argon-sulfur hexafluoride mixtures.

The final result seen in Figure 28 (solid lines) is encouraging, predicting the trend of the data quite well. The close agreement between the data and the prediction based on the adiabatic flame temperature is caused primarily by a fortuitous choice of total pressure for the burning rate tests in argon-sulfur hexafluoride

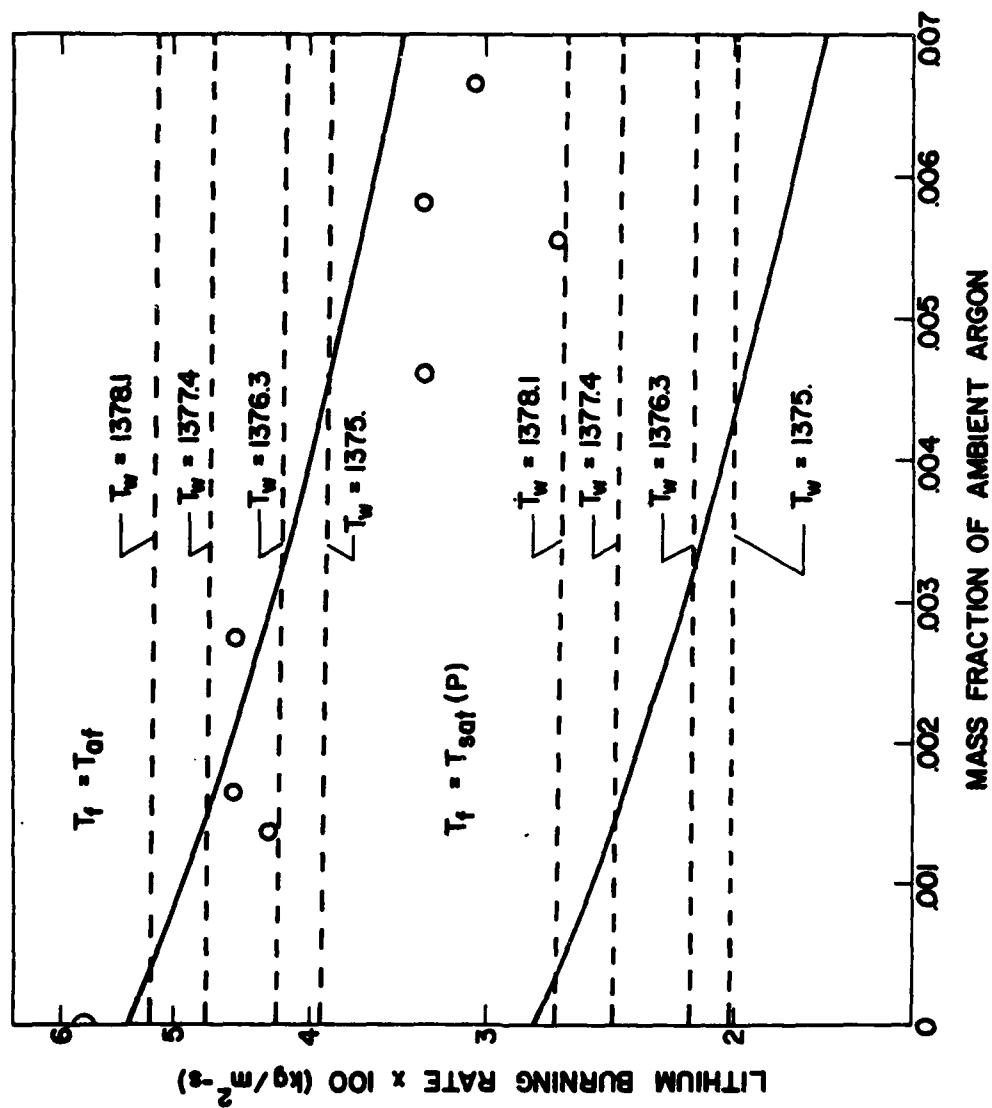


Figure 28 Prediction of the No-Condensation Model for the Effect of Ambient Argon Concentration on the Lithium Burning Rate in Sulfur Hexafluoride for Constant Wick Length (30 mm) and Constant Total Pressure (13300 Pa)

mixtures, since the results of the analysis for pure oxidizer show the best agreement at this pressure.

In general, the no-condensation model of lithium-sulfur hexafluoride combustion agrees reasonably well with the data. The primary shortcoming of the model is the failure to predict the changing slope of the burning rate as a function of oxidizer pressure. Despite this, the predictions are of the right order of magnitude and provide valuable base-line information.

6.3 Condensation - Front Model

6.3.1 Description and Assumptions

A schematic diagram of the condensation-front model is presented in Figure 29. The assumptions of the model can be summarized as follows:

1. The boundary layer (total thickness equal to δ_e) is divided into four regions by a flame zone and two condensation fronts, all of negligible thickness compared to δ_e . (The aerodynamic and concentration boundary layers are assumed to be of equal thickness.) The total pressure is constant throughout the boundary layer and continuous binary diffusion laws are assumed to be valid. The gases in each region are assumed to obey the perfect gas law. No inert diluent gas is present.
 - (1a) Region 1b ($0 \leq y \leq \delta_1$) contains only metal vapor and product vapor.
 - (1b) Region 1a ($\delta_1 \leq y \leq \delta_f$) contains only metal vapor and product vapor.

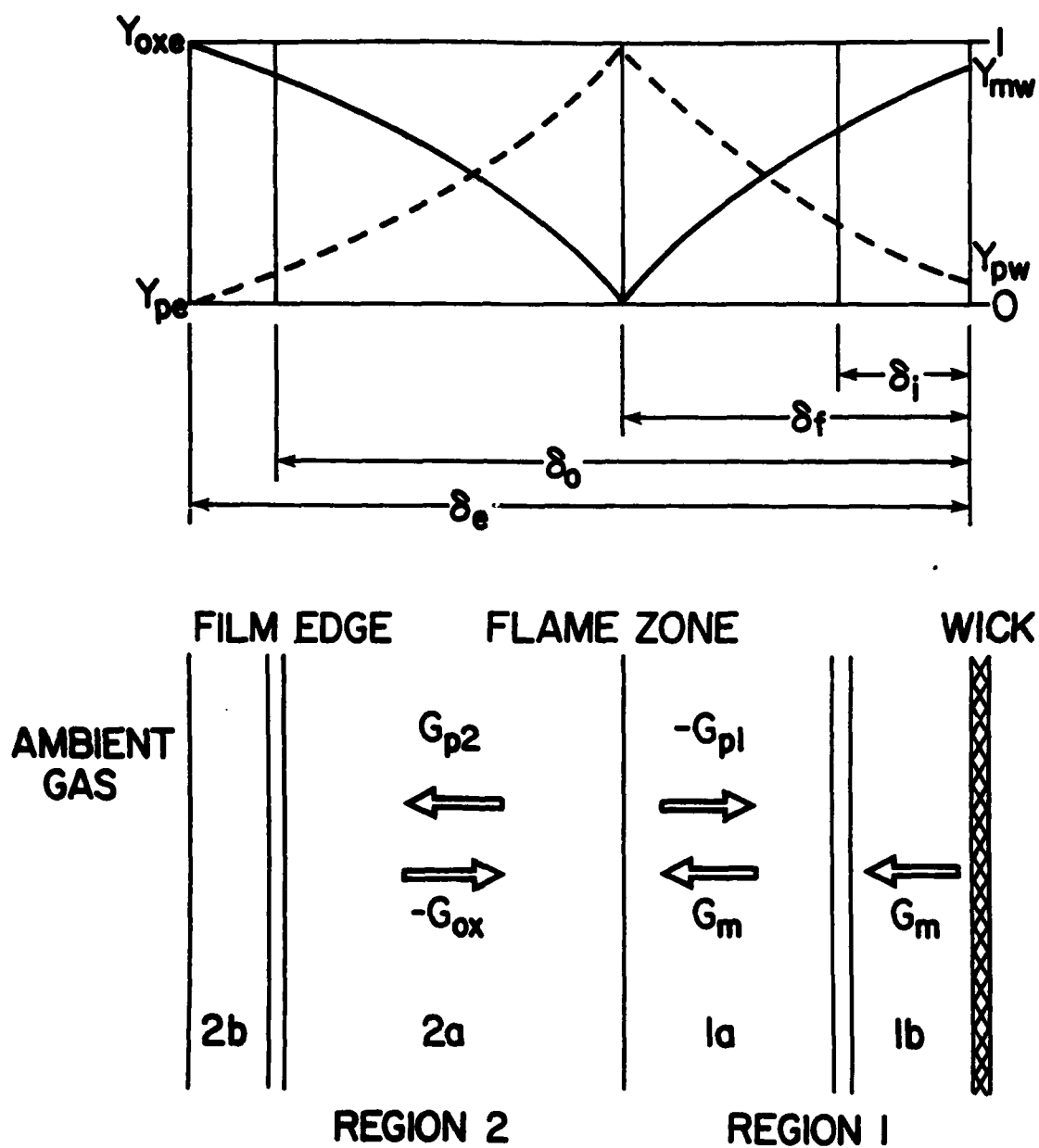


Figure 29 Schematic Diagram of Condensation-Front Model

- (1c) Region 2a ($\delta_f \leq y \leq \delta_o$) contains only oxidizer and product vapor.
- (1d) Region 2b ($\delta_o \leq y \leq \delta_e$) contains only oxidizer and product vapor.
2. The flame is assumed to be a thin diffusion flame (cf. Figure 23a) with the concentrations of fuel and oxidizer both equal to zero at the flame.
 3. Immediately after ignition the liquid at the wick surface is assumed to be a saturated fuel-product solution and the product vapor in Region 1b is assumed to be stagnant. Products flow as a vapor from the flame toward the condensation front. All flow parallel to the fuel surface is neglected.
 4. The vapor pressure of the products at the condensation fronts is determined by the "tangency" condition described in detail in Section 6.3.2, and shown in Figure 30.
 5. The products are assumed to exist in stoichiometric proportion (six moles of LiF for each mole of Li_2S) and to behave as a single species with averaged properties throughout the boundary layer.
 6. The vapor pressures of the metal and products at the wall are assumed to be given by the ternary model of Groff (27).
 7. Condensation is assumed to have a negligible effect upon the temperature profile, and radiation is neglected.
 8. Thermal and transport properties are assumed to be constant in each region.

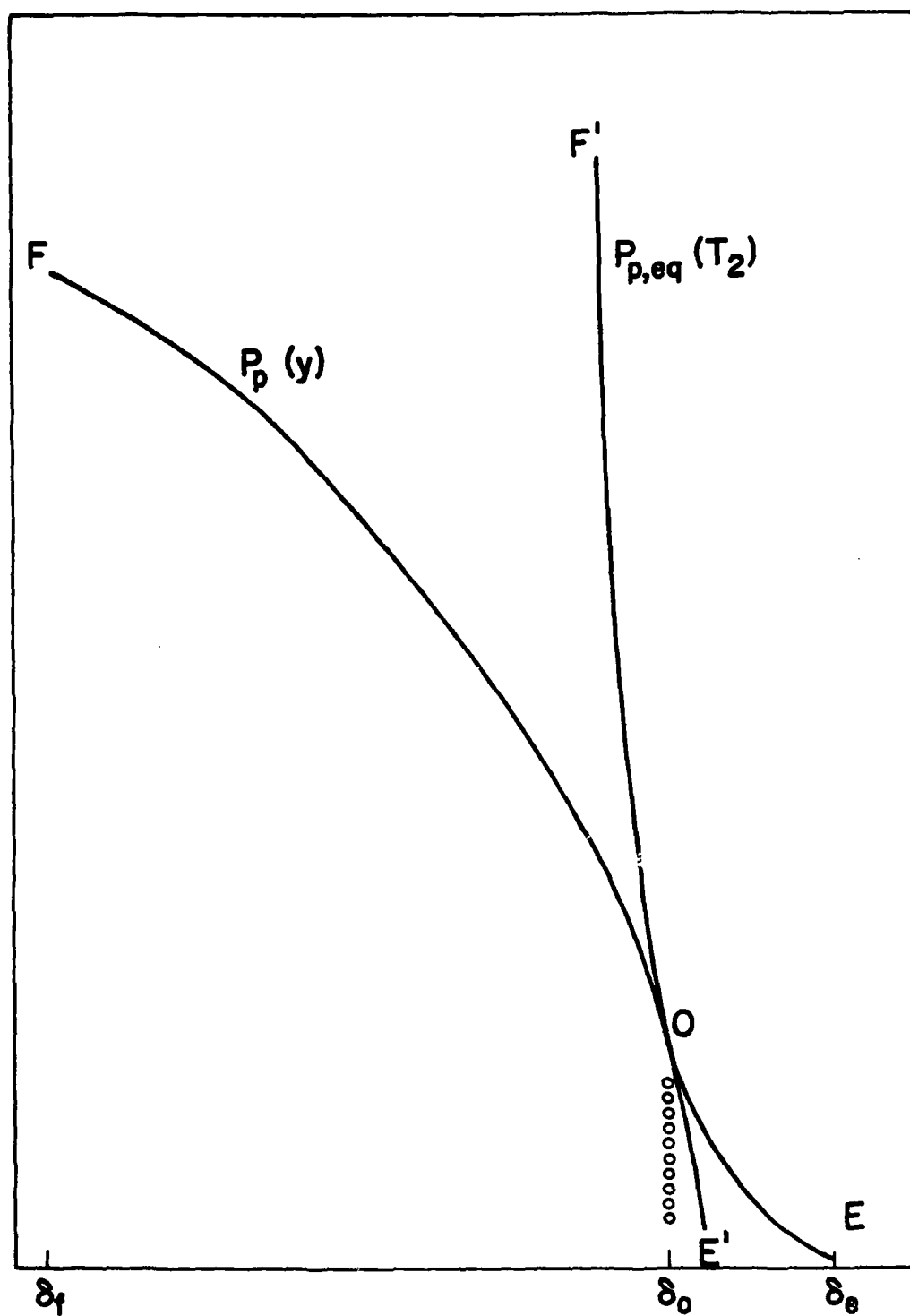


Figure 30 Schematic Diagram of the Tangency Condition at the Outer Condensation Front

9. The flame temperature is given by the adiabatic flame temperature of Equation (1.2) with gaseous products.

No inert gas is included in this analysis because of the difficulty of predicting its behavior throughout the boundary layer, particularly at the condensation fronts. The presence of a noncondensable is known to have significant effects on condensation processes (47-49). In addition, the more significant problem is that of the pure oxidizer with no diluent present.

6.3.2 Analysis

As with the no-condensation model, the analysis begins with the differential equation for a concentration boundary layer with both diffusion and convection (46):

$$G_y \frac{dY_k}{dy} - \frac{d}{dy} \left[\rho D \frac{dY_k}{dy} \right] = \frac{dG_k}{dy} \quad (6.2)$$

Again, G_y is the total mass flux in each region and is a constant throughout each region. The subscript k indicates the component of interest, i.e., the lithium or the oxidizer, depending on the region.

The analysis for Regions 1a and 2a proceeds much as in Section 6.2.2 for Regions 1 and 2, with the only changes being in the boundary conditions and the total mass flux. As in the no-condensation model, the reaction is assumed to occur only at $y = \delta_f$, therefore $\frac{dG_k}{dy} \equiv 0$ for both regions. This permits us to integrate Equation (6.2) as before to yield:

$$G_y Y_k - \rho D \frac{dY_k}{dy} = G_k = \text{constant} \quad (6.3)$$

However, G_y , the total mass flux, is now given by:

$$G_y = G_m + G_{p1} = G_{ox} + G_{p2} . \quad (6.19)$$

In Region 1a, Equation (6.3) becomes:

$$G_y Y_m - (\overline{\rho D})_{1a} \frac{dY_m}{dy} = G_m . \quad (6.20)$$

The boundary conditions in Region 1a are:

$$Y_m(\delta_1) = Y_{m1} \quad (6.21)$$

$$Y_m(\delta_f) = 0 . \quad (6.22)$$

With these boundary conditions, Equation (6.20) can be integrated across Region 1a to yield

$$G_y = \frac{(\overline{\rho D})_{1a}}{(\delta_f - \delta_1)} \ln \left[\frac{1}{1 - \frac{G_y}{G_m} Y_{m1}} \right] . \quad (6.23)$$

As in Region 2 of the no-condensation model, Equation (6.3) becomes, for Region 2a:

$$G_y Y_{ox} - (\overline{\rho D})_{2a} \frac{dY_{ox}}{dy} = G_{ox} . \quad (6.8)$$

The boundary conditions for Region 2a are:

$$Y_{ox}(\delta_o) = Y_{oxo} \quad (6.24)$$

$$Y_{ox}(\delta_f) = 0 . \quad (6.25)$$

Integrating Equation (6.8) with these boundary conditions, and combining the result with Equation (6.10) yields:

$$G_y = \frac{(\overline{\rho D})_{2a}}{(\delta_o - \delta_f)} \ln \left[1 + \frac{G_y}{G_m} \frac{Y_{oxo}}{r} \right] . \quad (6.26)$$

(Note that if δ_i and δ_o are at the wall and the film edge, respectively, and if $G_y = G_m$, the results given by Equation (6.23) and (6.26) agree with the results of the no-condensation model.)

The final mass flux equation comes from consideration of Region 1b. (We shall see later that no analysis of Region 2b is needed.) Since the total mass flux in Region 1b is comprised only of metal vapor, Equation (6.3) becomes:

$$G_m Y_m - (\overline{\rho D})_{1b} \frac{dY_m}{dy} = G_m, \quad (6.27)$$

which is the same form as Equation (6.4). The boundary conditions in Region 1b, are:

$$Y_m(0) = Y_{mw} \quad (6.28)$$

$$Y_m(\delta_i) = Y_{mi} \quad (6.22)$$

With these boundary conditions, Equation (6.27) can be integrated across Region 1b to yield:

$$G_m = \frac{(\overline{\rho D})_{1b}}{\delta_i} \ln \left[\frac{1 - Y_{mi}}{1 - Y_{mw}} \right] \quad (6.29)$$

The temperature profiles can be obtained by considering the one-dimensional energy equation with constant specific heats:

$$G_y \frac{dT}{dy} = \frac{\lambda}{C} \frac{d^2 T}{dy^2} + \frac{1}{C} \frac{dq''}{dy} \quad (6.30)$$

According to assumption (7), Equation (6.30) need only be divided into two regions: Region 1 and 2. Since radiation and condensation are neglected, $q''=0$ in both regions. With this simplification, for Region 2, Equation (6.30) becomes:

$$G_y \frac{dT_2}{dy} = \left[\frac{\lambda}{C} \right]_2 \frac{d^2 T_2}{dy^2} \quad (6.31)$$

The boundary conditions for Equation (6.31) are:

$$T_2(\delta_f) = T_f \quad (6.32)$$

$$T_2(\delta_e) = T_e \quad (6.33)$$

Integrating Equation (6.31) and inserting these boundary conditions yields:

$$T_2 = T_2 + (T_f - T_e) \frac{\exp(y - \delta_e) G_y C_2 / \lambda_2 - 1}{\exp(\delta_f - \delta_e) G_y C_2 / \lambda_2 - 1} \quad (6.34)$$

In Region 1, Equation (6.30) becomes:

$$G_y \frac{dT_1}{dy} = \left[\frac{\lambda}{C} \right]_1 \frac{d^2 T_1}{dy^2} \quad (6.35)$$

The boundary conditions for Region 1 are:

$$T_1(0) = T_w \quad (6.36)$$

$$T_1(\delta_f) = T_f \quad (6.37)$$

Integrating Equation (6.35) and inserting these boundary conditions yields:

$$T_1 = T_w + (T_f - T_w) \frac{\exp(y G_y C_1 / \lambda_1) - 1}{\exp(\delta_f G_y C_1 / \lambda_1) - 1} \quad (6.38)$$

The location of the condensation fronts can be determined by realizing that the equilibrium vapor pressure curve and the actual vapor pressure curve of the products must be tangent at the onset of condensation. (This is the "tangency condition" in assumption [4].)

The slope of the actual vapor pressure curve (curve F-O-E' in Figure 30) at δ_0 , for example, determines the rate at which product vapor flows into δ_0 , and the slope of the equilibrium vapor pressure curve (curve F'-O-E in Figure 30) determines the rate at which product vapor flows from δ_0 toward δ_e . Consequently, we can see that the actual vapor pressure profile across the entire region must follow curve F-O-E in Figure 30. A similar argument can be made for the conditions at δ_1 . Therefore, we can obtain two equations expressing these tangency conditions:

$$\left[\frac{dP_p}{dy} \right]_{\delta_1} = \left[\frac{dP_{p,eq}}{dy} \right]_{\delta_1} \quad (6.39)$$

$$\left[\frac{dP_p}{dy} \right]_{\delta_0} = \left[\frac{dP_{p,eq}}{dy} \right]_{\delta_0} \quad (6.40)$$

The equilibrium vapor pressure of the products is known from Groff's model (31) and is plotted in Figure 31. For the range of interest of the present study, it is evident that the vapor pressure can be expressed by an equation of the form:

$$P_{p,eq} = \exp(A-B/T) \quad (6.41)$$

Using the Chain Rule of Differentiation, we obtain:

$$\left[\frac{dP_{p,eq}}{dy} \right] = \left[\frac{dP_{p,eq}}{dT} \right] \left[\frac{dT}{dy} \right] \quad (6.42)$$

The actual vapor pressure profiles are obtained by rearranging Equations (6.8) and (6.20). Knowing the mass fractions of the various species (fuel, oxidizer and product) in each region, we can obtain an expression, for mole fraction of the products as a function of

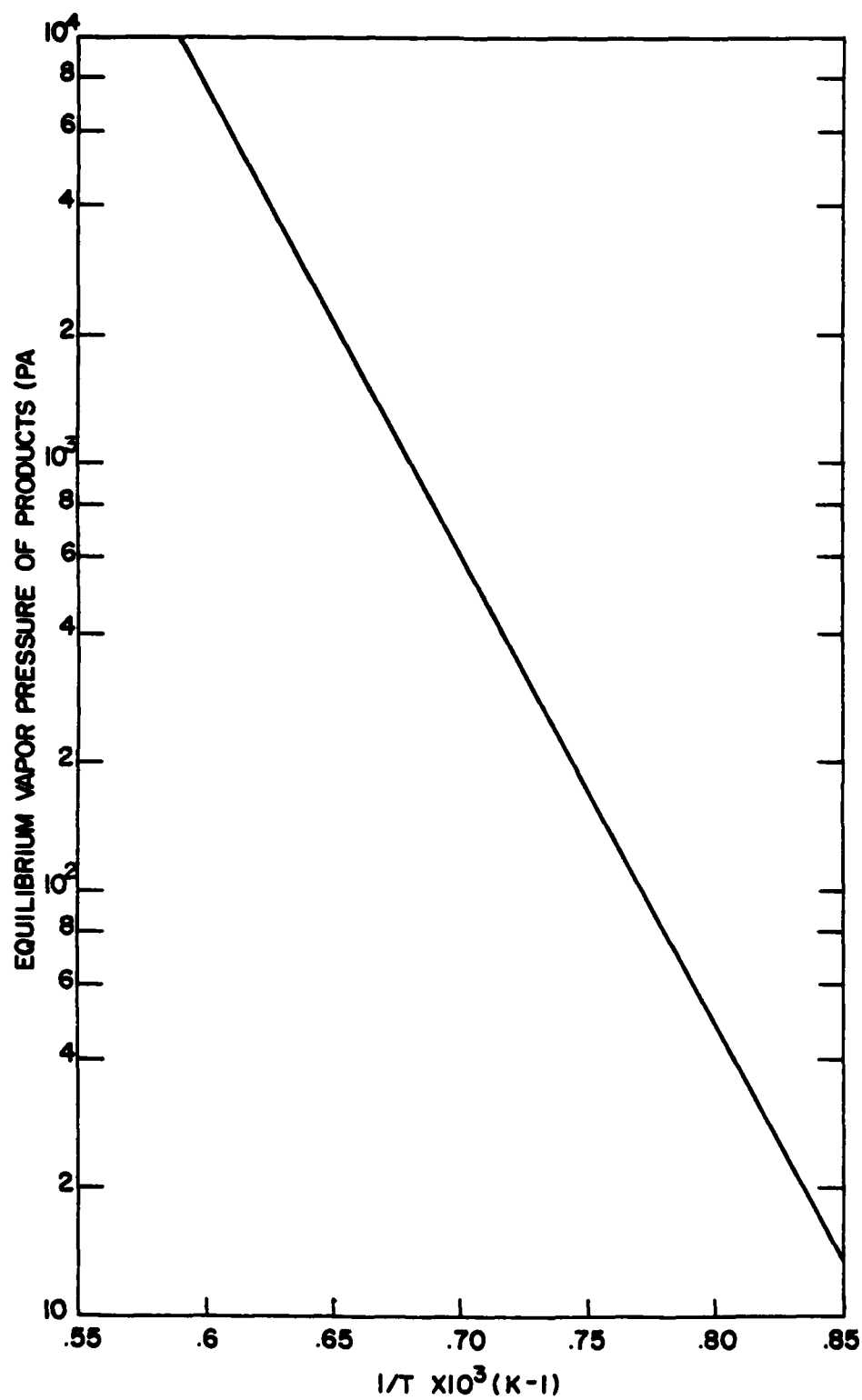


Figure 31 Vapor Pressure of Stoichiometric Products of Lithium-Sulfur Hexafluoride Combustion

location, and, hence, the partial pressure variation with location:

$$P_p = P_T(X_p) . \quad (6.43)$$

Finally, we obtain

$$\frac{dP_p}{dy} = P_T \frac{dX_p}{dy} \quad (6.44)$$

for each region, which, along with Equation (6.42), yields the necessary information to solve Equations (6.39) and (6.40). The set of equations is complete and can be solved by an iterative procedure.

Note that we have not needed any mass-flux equation in Region 2b. One of the advantages of this model is that we need not make any assumptions about the behavior of the mass fluxes in this region. The only assumption made in this region is included in the energy equation.

6.3.3 Results

The variation of lithium burning rate with oxidizer pressure as predicted by the condensation-front model is shown in Figure 32. The predicted variation can be expressed as:

$$G_m \propto p^{.525} . \quad (6.45)$$

The most noticeable effect of including condensation is to increase the influence of pressure by about one-third as compared with the no-condensation model.

As can be seen in Figure 32, the condensation-front model agrees quite well with the data in the lower range—up to about 8000

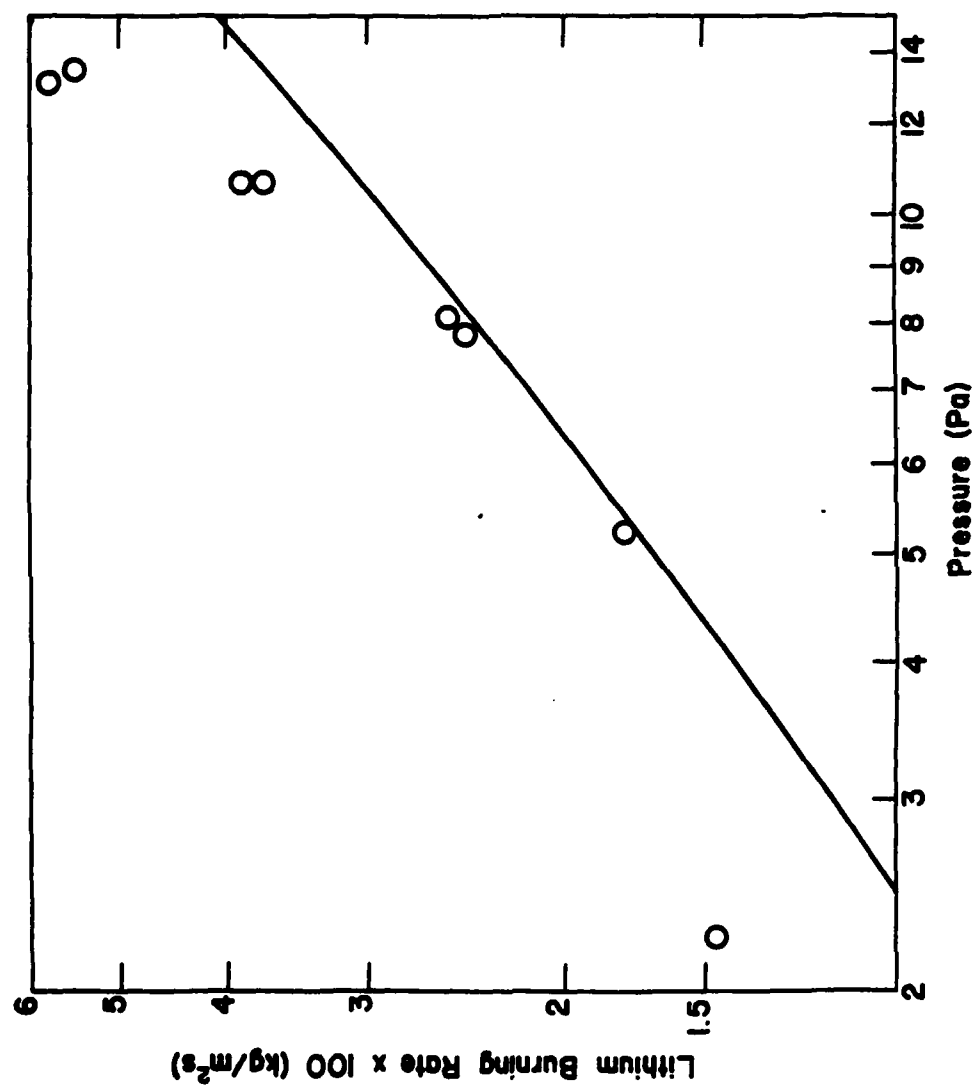


Figure 32 Prediction of the Condensation-Front Model for the Effect of Pressure on the Lithium Burning Rate in Sulfur Hexafluoride for a Constant Wick Length (30 mm)

Pa. Above 8000 Pa, the prediction deviates from the data, failing to account for the steepening of the slope of the data. Possible explanations for this will be discussed in Section 6.4.

The predicted effect of wick length is similar to the no-condensation model, differing only in magnitude. As a consequence of using the formula for δ_e suggested by Spalding, the model predicts:

$$G_m \propto L^{-1/4}.$$

The difference in magnitude is caused by the different prediction for burning rate at 10750 Pa. for a 30 mm wick. The prediction of the condensation-front model is merely a constant multiple of the no-condensation model. There is nothing new to be learned.

6.4 Discussion and Comparison of Theoretical Models

There are several aspects of the results of the models that should be examined in some detail. The most significant of these is the failure of the models to predict completely the variation of the lithium burning rate with oxidizer pressure as exhibited by the data. Related to this is the effect of including condensation in the model.

The condensation-front model demonstrates two significant improvements over the no-condensation model with regard to the burning rate data. The predicted pressure dependence is increased by about one-third, bringing the slope of the model closer to the measurements. In addition, the model predicts the actual values of the data much better, allowing for the fact that the adiabatic flame temperature is a more justifiable choice than the boiling point of the products to model the actual flame temperature.

One other significant improvement in the condensation-front model over the no-condensation model can be seen in the predicted structure of the boundary layer, including the temperature and concentration profiles. These predictions are presented in Figures 33 and 34 for the no-condensation model and the condensation model, respectively. The predictions are shown for the case of no inert diluent gas present, with the oxidizer pressure set at a typical value—7950 Pa. The boundary conditions at the fuel surface, at the flame, and in the ambient are the same for both models.

The most noticeable difference seen between the two predictions presented in Figures 33 and 34 is evident in the location of the flame. The flame stand-off distance predicted by the no-condensation model is almost twice the stand-off distance predicted by the condensation-front model.

With this in mind, it is worth comparing the predictions with the results obtained from the photographs of the burning rate tests. The values of flame stand-off distance predicted by each model are weak functions of Grashof Number, with the average results being, in the range of interest:

$$\left[\frac{\delta_f}{\delta_e} \right]_{\text{NC}} \approx .84 \quad (6.46)$$

$$\left[\frac{\delta_f}{\delta_e} \right]_{\text{CF}} \approx .47 \quad (6.47)$$

From the regression analysis for the data shown in Figures 12 and 13, we can obtain:

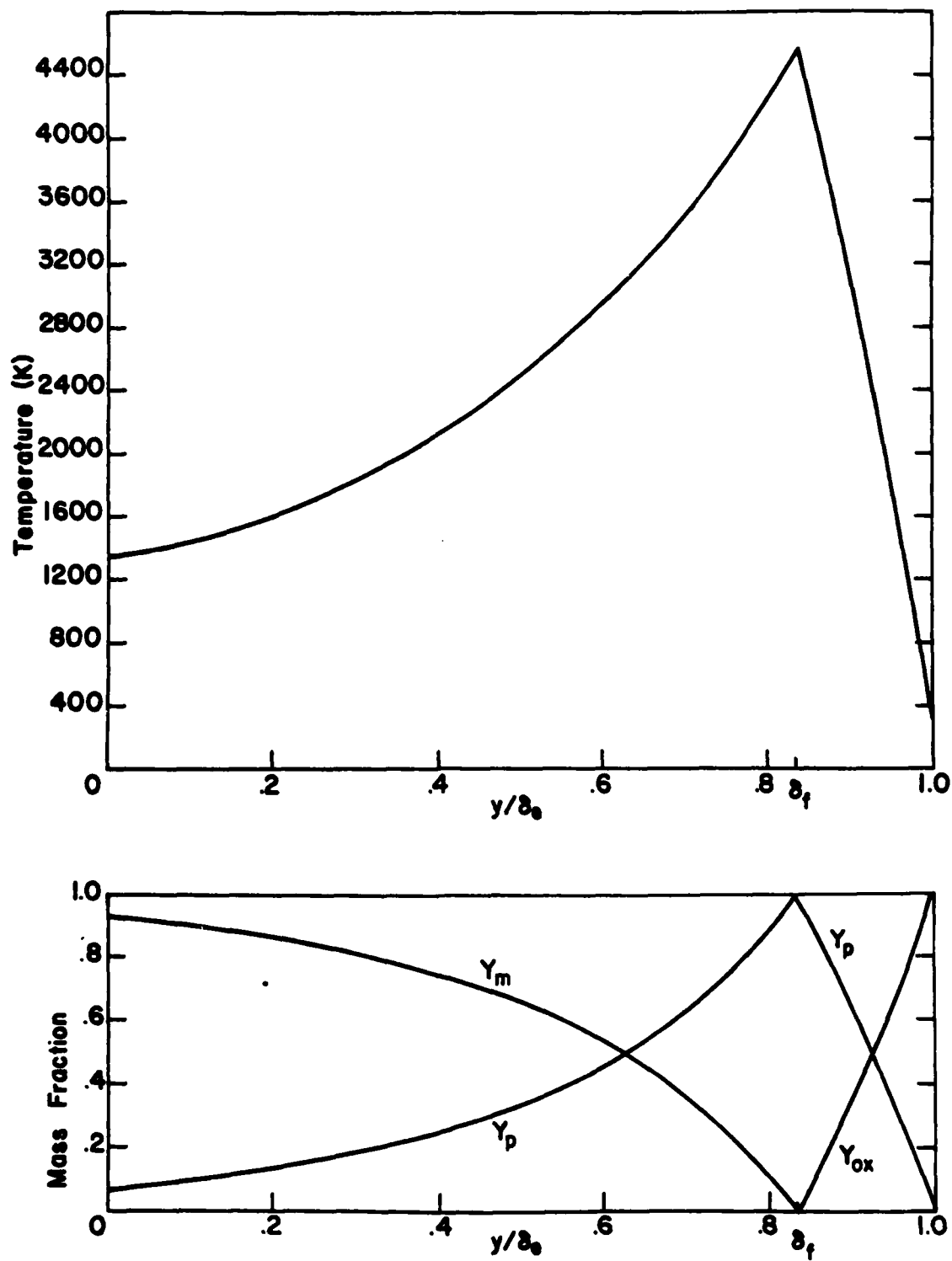


Figure 33 Temperature and Concentration Profiles
in the No-Condensation Model at 8000 Pa

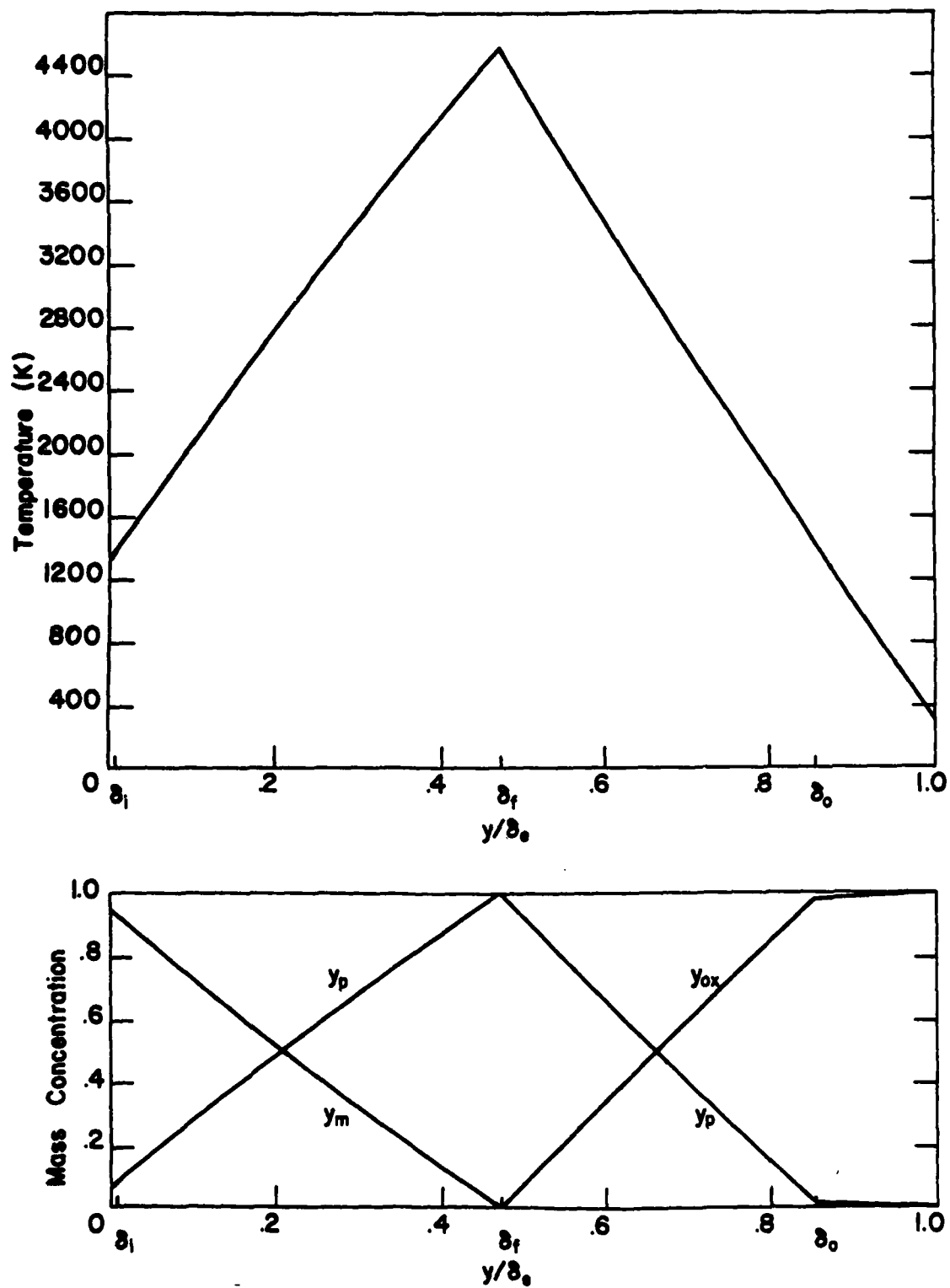


Figure 34 Temperature and Concentration Profiles in the Condensation-Front Model at 8000 Pa

$$\frac{\delta_f}{\delta_{lum}} \approx .35 \quad . \quad (6.48)$$

Because of the sharply decreasing temperature profile, we know that δ_{lum} is fairly close to δ_e . From the condensation-front model, we know that the temperature at δ_o is only slightly above the threshold of visible radiation. We also have that the predicted value of δ_o is given by:

$$\frac{\delta_o}{\delta_f} \approx .85 \quad . \quad (6.49)$$

This ratio is very nearly constant over the range of pressure examined. Consequently, it seems reasonable to assume that:

$$\delta_{lum} \approx \delta_o \quad ,$$

and, therefore, we can conclude from the data:

$$\frac{\delta_f}{\delta_e} \approx .3 \quad . \quad (6.50)$$

Obviously, the condensation-front model is much closer to this value than is the no-condensation model.

The narrower flame stand-off distance predicted by the condensation-front model is easily understood in light of the physical processes included in the model. The product flux toward the surface impedes the flow of metal vapor towards the flame. In addition, less product flows outward to impede the influx of the oxidizer toward the flame. Consequently, the oxidizer penetrates farther into the boundary layer than is predicted by the no-condensation model.

An examination of the shape of the profile also reveals more about the nature of the net mass fluxes predicted by each of the two models. The net mass flux for the no-condensation model is comprised solely of the lithium mass flux, which is directed away from the fuel surface. The effect of this can be seen in the temperature profile. The profile is "bowed out" away from the surface, reflecting the convection of energy away from the wall by the net mass flux.

The net mass flux for the condensation-front model in Regions 1a and 2a is comprised of the fluxes of fuel and oxidizer toward the flame and the flux of product away from the flame. The product flux in Region 1a is slightly greater than the flux of fuel, resulting in a small, negative net mass flux in Region 1a. By continuity, we know the same is true for Region 2a. As a consequence, the predicted profiles are nearly linear, and bowed very slightly toward the surface. (The profiles would be exactly linear if the net mass flux were zero.)

The final observation to be made about the structure of the boundary layer concerns the location of the inner condensation-front as seen in Figure 34. The relative closeness of δ_1 to the wick surface helps to justify assumption (3) in Section 6.3.1. Most of the product will condense at δ_1 , leaving very little product vapor to be considered in Region 1b. Because of this, and since Region 1b is so narrow, it appears a posteriori the assumption that the product vapor is stagnant in this region is acceptable, particularly considering the overall level of complexity of the model.

The results of the present theoretical analysis show that including condensation reduces the overall burning rate, a result which appears to contradict both Rosner (12) and Kuehl and Zwillenberg (15). Rosner indicates that condensation should enhance burning rates by about three to four times. However, it should be recalled that Rosner assumes all the product condenses at the flame, and, consequently, there is no resistance to the flow of oxidizer or fuel caused by the product.

The increased burning rate caused by condensation seen by Kuehl and Zwillenberg (15) is a result of a different treatment of the energy equation. Their analysis included the additional heat input to the surface caused by the heat of condensation of the products, which had been neglected by Brzustowski and Glassman (14). The effect was to cause the fuel to vaporize more rapidly, resulting in an increased burning rate over the earlier work.

Neither of these circumstances is pertinent to the present study. Since the wick surface is considered to be at thermodynamic equilibrium, an increased heat input to the surface will not cause a corresponding increase in fuel vaporization rate (so long as the temperature does not change). The effect seen by Rosner is caused solely by his neglecting the fluxes of the products away from the flame.

The effect of wick length on the burning rate has been discussed chiefly in Section 6.1. The data obtained appear to justify the use of the expression suggested by Spalding (23) to describe the effects of natural convection in the aerodynamic boundary layer

as manifested by the relationship between the overall length of the wick and the measured burning rate.

The data obtained for lithium burning rate in argon-sulfur hexafluoride mixtures and the good agreement of the prediction of the no-condensation model with those data needs to be examined with care. If condensation processes are significant, as they appear to be, then one must question why a no-condensation model can predict the effect of an inert diluent gas so well. The answer lies in the work of Minkoqycz and Sparrow (47) and Othmer (48). Studying the condensation of steam, these workers showed that condensation processes are severely inhibited by the presence of a noncondensable. For example, condensation rates are reduced by about half for mass fractions of noncondensable air as low as 0.5 percent. Work by Kroger and Rohsenow (49) with potassium has shown similar results.

If, in addition to lowering the wick temperature, the presence of an inert gas at the wick surface impedes the condensation of the products, then more of the product must flow outward from the flame. Consequently, the flux of product in Region 1 is reduced, making that region more like the stagnant film assumed for the no-condensation model. In light of this, it is not unlikely that lithium-sulfur hexafluoride combustion in the presence of an inert gas (and other similar cases) can be adequately described by a model which neglects condensation of products in the gas phase.

The failure of either model, particularly the condensation-front model, to completely predict the behavior of the data (particularly with respect to pressure) raises further questions. There are three possible major areas of doubt in the present study. Two parts of the

theory need to be examined: the adiabatic flame temperature, and the omission of the effect of condensation on the temperature profile. The other area of doubt is in the data, particularly in the low pressure range.

The areas of doubt in the model are the easiest, and most straightforward, to understand. Neglecting the effects of dissociation and polymerization of the products and heat lost by radiation in the calculation of the adiabatic flame temperature yields a value that must be greater than the actual flame temperature. From Figure 25 we know the effect of the choice of flame temperature on the predicted burning rate. If, because of the low pressures used during the test program, dissociation of the products is significant, then the actual flame temperature could decrease much more rapidly as the pressure decreases than has been assumed. The predicted burning rate could then decrease from the adiabatic flame temperature prediction at high pressures, toward the saturated flame prediction at low pressures. A variation of this nature would result in a greater variation of burning rate with pressure, yielding a trend similar to that exhibited by the data. For the condensation-front model, the result would be to underpredict the data throughout the entire range of testing since the adiabatic flame temperature assumption yields the maximum prediction. However, while a decrease in the flame temperature is probable, because of greater dissociation at low pressures, no photographic evidence was obtained to indicate that the products condensed in the flame.

Neglecting the effect of condensation on the temperature profiles is the other doubtful area of the model. Inclusion of this effect

would serve to move the fronts closer to the flame. Since condensation is an isothermal process (or nearly so), the temperature profiles would steepen near the flame, flatten for a short distance through the condensation fronts, then drop to the values at the extremes of the boundary layer. Based on the results seen thus far, including this effect should steepen the slope of the predicted dependence on oxidizer pressure and increase the predicted burning rates. Combining this effect with an improved flame temperature in the model would tend to negate the lowering of the prediction resulting from the lower flame temperature. It is possible that a model including both of these effects could predict the behavior of the data.

The previous discussion has been based on the premise that the data are correct. While a more complete model must include the modifications suggested, it is possible that the present model is being compared to data that are, at least, somewhat faulty, particularly in the low pressure region. From the agreement of the data gathered at the higher pressures, 10750 Pa (wick length tests) and 13300 Pa. (argon-sulfur hexafluoride mixtures), there is little cause to doubt the results in the higher pressure region. However, the difficulties encountered in obtaining any data in the low pressure region raise questions. Since no duplication of the points was obtained, it is possible that the data in the low pressure region are deceptive particularly at the lowest pressure, causing us to attempt to predict behavior in the data that does not really exist (if the point is high). If a non-condensable contaminant was present during a test, then the measured burning rate will be lower than it should be.

For the sake of argument, assume that some noncondensable was present at the wick surface as a result of impurities present in either the lithium or sulfur hexafluoride. Instead of assuming that the wick temperature was specified by Groff's model (27) at a given pressure, the wick temperature was obtained from the pressure-temperature data shown in Figure 22. The divergence between the predicted and measured temperatures in Figure 22 is not great, being less than 2% for a pressure of 1000 Pa (i.e., the data indicate a lower temperature than predicted by Groff's model), and approximately zero at 15000 Pa. Table 8 compares some of the values predicted by Groff (27) with the corresponding data from Figure 22.

The no-condensation model was used to calculate this effect since, as noted previously, the condensation-front model is not designed to handle noncondensables. The result of this modification is presented in Figure 35, using only the adiabatic flame temperature procedure for estimating properties. Note the markedly steeper slope of the prediction and the comparatively good agreement with the data. Obviously, the possibility of the presence of noncondensable contaminants cannot be ignored as an explanation of the data.

Three sources of doubt in the present study have been examined. The existence of noncondensable contaminants appears to be quite likely the cause of the unusual variation of the lithium burning rate with pressure. However, the evidence is not conclusive and more data should be obtained over a wider range of pressure before firm conclusions can be obtained. For this to be accomplished, ignition difficulties must be overcome at low pressure. To extend the data to higher

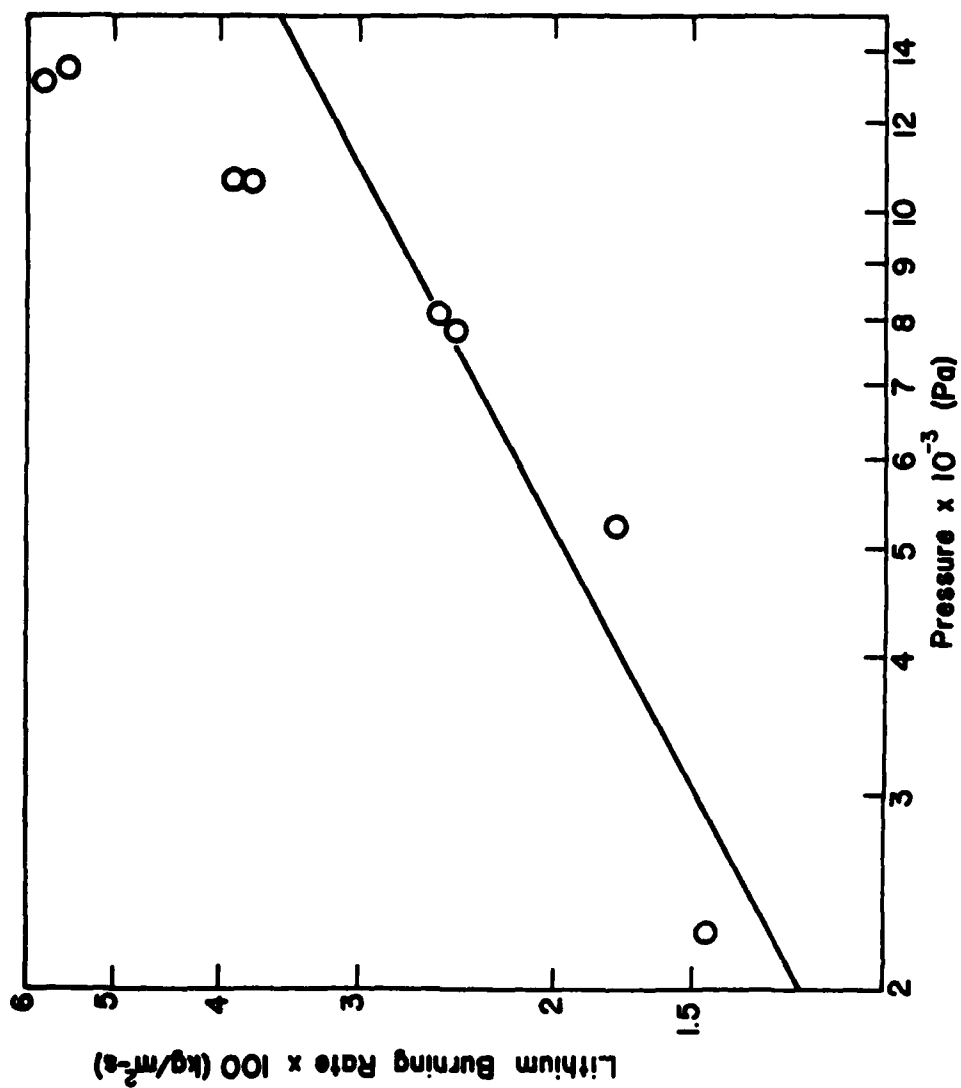


Figure 35 Prediction of the No-Condensation Model for the Effect of Noncondensable Contaminants Using Experimental Data to Specify Wick Conditions

Table 8

Comparison of Temperatures Predicted by Groff (27) with
Data Obtained from the Wick-Type Combustor Tests

Pressure (Pa)	Temperature from Groff (K)	Temperature from Tests (K)
12500	1370	1370
8800	1331	1330
7700	1319	1316
5500	1287	1282
3900	1257	1250
2800	1230	1220

pressure a material must be found for the sample cylinders that will withstand the high corrosive attack by the oxidizer seen during the present study.

If more data show that the behavior of the data is not caused by noncondensable contaminants, then the theory should be modified to account for the effects of condensation on the temperature profile and the effects of dissociation on the flame temperature. It should also be noted that, in order to generalize the model to combustion systems other than lithium-sulfur hexafluoride (where thermodynamic models such as Groff's are not available), more complete consideration of the energy equation would be needed. This would include such effects as heat loss by radiation and increased fuel vaporization caused by the heat of condensation (e.g., see the results of Kuehl and Zwillenberg [15]).

CHAPTER VII

SUMMARY AND CONCLUSIONS

7.1 Summary

The overall objectives of the present study were to experimentally analyze the combustion process of a liquid metal burning from a vertical wick and to develop a theoretical model to describe the process. The work was limited to the combustion of lithium with sulfur hexafluoride because of the technological importance of this reactant combination.

Two types of experiments were performed. The first type of test involved the combustion of lithium from a vertical wick. Photographs were obtained to study the nature of the combustion (i.e., surface or vapor-phase, flame stand-off distance, etc.). Burning rates as a function of ambient pressure, total wick length, and concentration of inert diluent in the ambient gas were also obtained from these tests. A limited range of pressure (2250-13300 Pa) was used because of experimental difficulties. Ignition reliability was poor below 7000 Pa, limiting data in this region: above 14000 Pa, the wick and support suffered rapid corrosive attack by the oxidizer (because of the high combustion temperature encountered), precluding testing in this range.

The second type of experiment involved the use of wick-type combustor tests to determine the relationship between wick surface temperatures and combustor pressure. The data compared favorably

with Groff's thermodynamic model (27), with the difference increasing slowly as the temperature (pressure) was decreased. These results, combined with the observations made during the burning rate tests, justified modelling the combustion process as a thin diffusion flame.

Two theoretical models were developed, using a film-theory approximation for convection. A model neglecting the condensation of the products, the no-condensation model, was developed to ascertain its applicability to the present system and to provide base-line results. The no-condensation model predicted the effect of the inert diluent in the ambient gas quite well. The predicted effect of oxidizer pressure was substantially less than demonstrated by the data.

A model allowing for condensation to occur within the boundary layer, the condensation-front model, was developed to consider some of the physical processes actually occurring for combustion in the absence of an inert diluent in the ambient gas. The predicted dependence on oxidizer pressure was one-third higher than the no-condensation model, but still somewhat less than demonstrated by the data. This model also provided better predictions for flame position than the no-condensation model. Both models provided an adequate correlation of the effect of wick height on the burning rate.

An analysis was performed to determine the effect of the presence of noncondensable contaminants on the data. Using the experimentally-obtained pressure-temperature relationship (rather than the thermodynamic model of Reference [27]), it was found that the presence of noncondensable contaminants could cause the observed strong

variation in the burning rate with pressure because of the increasing importance of small quantities of noncondensable contaminants as pressure is decreased.

7.2 Conclusions

The major conclusions of the present study are:

- (1) Lithium-sulfur hexafluoride combustion occurs in the vapor phase. Some product condenses on the fuel surface, but this does not appear to inhibit the evaporation of the fuel from the surface. Product can also be seen to condense in the gas phase, but not in the flame zone.
- (2) Natural convection effects are significant and can be correlated using the procedure suggested by Spalding (23).
- (3) The inclusion of condensation effects in a theoretical model increases the predicted variation of burning rate with pressure. The effect of including condensation in the model is to provide a more realistic prediction of the structure of the boundary layer. However, the no-condensation model does provide reasonable estimates of the burning rates, particularly in light of the uncertainties in the transport properties.
- (4) The effect of condensation on the combustion process is significantly reduced when a noncondensable is present, much like the effect of a noncondensable present in normal condensation processes, such as steam condensation.
- (5) The presence of noncondensable contaminants may have very significant effects on low-pressure combustion processes involving condensable products. In particular,

the strong variation of burning rate with pressure seen in the present study could be a result of the greater influence of low levels of contamination at low pressure.

7.3 Recommendations for Further Study

The present study, while providing useful information on the combustion of metals in pure, and nearly pure, oxidizing atmospheres, leaves several areas that should be examined in more detail. In particular, these are:

- (1) More experimental data must be obtained concerning the dependence of lithium burning rate on pressure. This will serve to clarify the behavior seen in the present study and resolve more thoroughly questions concerning the possible effect of noncondensable contaminants.
- (2) If the behavior of the data seen in the present study is confirmed, the theoretical model should be modified to include dissociation effects on flame temperature and condensation effects on the temperature profiles across the boundary layer. Radiation losses caused by the presence of condensed particles at high temperature should also be considered.

REFERENCES

1. Uhlemann, H., Spigt, C. L., and Hermans, M. L., "The Combination of a Stirling Engine with a Remotely Placed Heat Source," Ninth Intersociety Energy Conversion Engineering Conference, The Institute of Electrical and Electronics Engineers, Inc., New York, New York, 1974, p. 620-629.
2. Mattavi, J. N., Heffner, F. E., and Miklos, A. A., "The Stirling Engine for Underwater Vehicle Applications," Society of Automotive Engineers, National Powerplant Meeting, Cleveland, Ohio, Paper No. 690731, October 27-29, 1969.
3. "Metal-Combustion Energy Drives Stirling Engines Under the Sea," Product Engineering, Vol. 40, No. 25, 1969, p. 104-106.
4. van der Sluijs, W. L. N., "A Lithium/Sodium/Sulfurhexafluoride Heat Source in Combination with a Stirling Engine as a Propulsion System for Small Submersibles," Tenth Intersociety Energy Conversion Engineering Conference, The Institute of Electrical and Electronics Engineers, Inc., New York, New York, 1975, p. 1031-1036.
5. Biermann, U. K. P., "The Lithium/Sulfurhexafluoride Heat Source in Combination with a Stirling Engine as an Environmental Independent Underwater Propulsion System," Tenth Intersociety Energy Conversion Engineering Conference, The Institute of Electrical and Electronics Engineers, Inc., New York, New York, 1975, p. 1023-1030.
6. Blakeslee, T. III, Groff, E., Faeth, G. M., Olson, D. R., "A Study of a Liquid Metal Thermal Energy Source, Annual Report: September 1, 1973 to August 31, 1974," Contract No. N00600-74-C-0033, Advanced Research Projects Agency, ARPA Order No. 2150, Program Code No. 2N10, Mechanical Engineering Department, The Pennsylvania State University, September 1974.
7. Schmidt, H. W., Handling and Use of Fluorine and Fluorine-Oxygen Mixtures in Rocket Systems. Office of Technology Utilization, National Aeronautics and Space Administration, Washington, D.C. 1967.
8. Blakeslee, T. III, Groff, E., Faeth, G. M., Olson, D. R., "A Study of a Liquid Metal Thermal Energy Source, Quarterly Technical Report: June 1, 1975 to August 31, 1975," Contract No. N00600-74-C-0033, Advanced Research Projects Agency, ARPA Order No. 2150, Program Code No. 2N10, Mechanical Engineering Department, The Pennsylvania State University, October, 1975.

9. Avery, J. F., "Combustion of a Submerged Turbulent Oxidizer Jet in a Liquid Metal," Ph.D. Thesis - The Pennsylvania State University, 1974.
10. Weimer, J. C., "Investigation of a Submerged High Velocity Vapor Jet," M.S. Thesis - The Pennsylvania State University, 1972.
11. Turkdogan, E. T., Grieveson, P., and Darken, L. S., "Enhancement of Diffusion-Limited Rates of Vaporization of Metals," Journal of Physical Chemistry, Vol. 67, August, 1963, p. 1647-1654.
12. Rosner, D. E., "Effects of Product Condensation on Reaction-Enhanced Vaporization Rates and on the Transition from Homogeneous to Heterogeneous Reaction in High-Temperature Metal Oxidation," Oxidation of Metals, Vol. 4, No. 1, 1972, p. 1-25.
13. Brzustowski, T. A. and Glassman, I., "Vapor-Phase Diffusion Flames in the Combustion of Magnesium and Aluminum: I. Analytical Developments," Heterogeneous Combustion - Progress in Astronautics and Aeronautics, Vol. 15, Academic Press, New York, New York, 1964, p. 75-115.
14. Grosse, A. V. and Conway, J. B., "Combustion of Metals in Oxygen," Industrial and Engineering Chemistry, Vol. 50, No. 4, April, 1958, p. 663-672.
15. Kuehl, D. K. and Zwillenberg, M. L., "Predictions of Burning Times of Metal Particles," AIAA Paper No. 68-494, 1968.
16. Klyachko, L. A., "Combustion of a Stationary Particle of Low-Boiling Metal," Combustion, Explosion, and Shock Waves, Vol. 5, No. 3, 1969, p. 279-284.
17. Law, C. K., "A Simplified Theoretical Model for the Vapor-Phase Combustion of Metal Particles," Combustion Science and Technology, Vol. 7, No. 5, p. 383-405.
18. Law, R. K., and Williams, F. A., "Combustion of Magnesium Particles in Oxygen-Inert Atmosphere," Combustion and Flame, Vol. 22, No. 3, June, 1974, p. 383-405.
19. Darken, L. S., and Gurry, R. W., "The System Iron-Oxygen, II. Equilibrium and Thermodynamics of Liquid Oxide and Other Phases," Journal of the American Chemical Society, Vol. 68, May, 1946, p. 798-816.
20. Brzustowski, T. A. and Glassman, I., "Vapor-Phase Diffusion Flames in the Combustion of Magnesium and Aluminum: II. Experimental Observations in Oxygen Atmospheres." Heterogeneous Combustion-Progress in Astronautics and Aeronautics, Vol. 15, Academic Press, New York, New York, 1969, p. 117-158.

21. Coffin, K. P., "Some Physical Aspects of the Combustion of Magnesium Ribbons," Fifth Symposium (International) on Combustion, Reinhold Publishing Corp., New York, New York, 1955. p. 267-276.
22. Richard, J. R., Delbourgo, R., and Laffitte, P., "Spontaneous Ignition and Combustion of Sodium Droplets in Various Oxidizing Atmospheres at Atmospheric Pressure," Twelfth Symposium (International) on Combustion, The Combustion Institute, Pittsburgh, Pennsylvania, 1969, p. 39-48.
23. Spalding, D. B., "The Combustion of Liquid Fuels," Fourth Symposium (International) on Combustion, The Williams and Wilkins Co., Baltimore, Maryland, 1953, p. 847-864.
24. Kim, J. S., DeRis, J., and Kroesser, F. W., "Laminar Free Convective Burning of Fuel Surfaces," Thirteenth Symposium (International) on Combustion, the Combustion Institute, Pittsburgh, Pennsylvania, 1971, p. 949-961.
25. Feldman, K. T., Scott Heat Pipe Analysis, Design and Experiments, Scott-Engineering Sciences, Pompano Beach, Florida, December, 1968.
26. Ferrell, J. K., Winston, H., and Davis, R., Heat Pipe Properties and Performance, Report: Department of Chemical Engineering, North Carolina State University, Raleigh, North Carolina, October, 1973.
27. Groff, E. G., "Characteristics of a Steadily Operating Metal Combustor," Ph.D. Thesis, The Pennsylvania State University, 1976.
28. Alexander, E. G., "Structure-Property Relationship in Heat Pipe Wicking Materials," Ph.D. Thesis, North Carolina State University, 1972.
29. Davison, Harry W., "Compilation of Thermophysical Properties of Liquid Lithium," NASA Technical Note, NASA TN D-4650, National Aeronautics and Space Administration, Washington, D.C., July, 1968.
30. Stull, D. R. and Prophet, H., Project Directors, JANAF Thermochemical Tables, NSRDS-NBS 37, U.S. Government Printing Office, Washington, D.C., June, 1971.
31. Berkowitz, J., and Chupka, W. A., "Composition of Vapors in Equilibrium with Salts at High Temperatures," Annals of the New York Academy of Sciences, Vol. 79, 1960, p. 1073-1078.
32. Groff, E. G., Personal Correspondence, 1976.
33. Markstein, G. H., "Combustion of Metals," AIAA Journal, Vol. 1, No. 3, March, 1963, p. 550-562.

34. Brzustowski, T. A., and Glassman, I., "Spectroscopic Investigation of Metal Combustion," Heterogeneous Combustion - Progress in Astronautics and Aeronautics, Vol. 15, Academic Press, New York, New York, 1964, p. 41-73.
35. Clarke, J. F., "On the Structure of a Hydrogen-Oxygen Diffusion Flame," Proceedings of the Royal Society of London - Series A, Vol. 307, October 15, 1968, p. 283-302.
36. Agrawal, D. D. and Gupta, C. D., "Computer Program for Constant Pressure or Constant Volume Combustion Calculations in Hydrocarbon-Air Systems," ASME Paper No. 76-DGP-2, 1976.
37. Avery, J. F. and Faeth, G. M., "Combustion of a Submerged Gaseous Oxidizer Jet in a Liquid Metal," Fifteenth Symposium (International) on Combustion, The Combustion Institute, Pittsburgh, Pennsylvania, 1974, p. 501-512.
38. Wilke, G. R., and Lee, C. Y., "Estimation of Diffusion Coefficients for Gases and Vapors," Industrial and Engineering Chemistry, Vol. 47, No. 6, June, 1955, p. 1253-57.
39. Hirschfelder, J. O., Curtiss, C. F., and Bird, R. B., Molecular Theory of Gases and Liquids, John Wiley and Sons, Inc., New York, New York, 1954.
40. Hirschfelder, J. O., Bird, R. D., and Spotz, E. L., "Viscosity and Other Physical Properties of Gases and Gas Mixtures," Transactions of the American Society of Mechanical Engineers, Vol. 71, No. 8, November, 1949, p. 921-937.
41. Brown, J. A., "Sulfur Fluorides," Kirk-Othmer: Encyclopedia of Chemical Technology, Vol. 9, Interscience Publishers, John Wiley and Sons, Inc., New York, New York, 1966.
42. Reid, R. C. and Sherwood, T. K., The Properties of Gases and Liquids - Their Estimation and Correlation, McGraw-Hill Book Co., New York, New York, 1966.
43. Wilke, C. R., "A Viscosity Equation for Gas Mixtures," Journal of Chemical Physics, Vol. 18, No. 4, April, 1950, p. 517-519.
44. Mason, E. A., and Saxena, S. C., "Approximate Formula for the Thermal Conductivity of Gas Mixtures," The Physics of Fluids, Vol. 1, No. 5, 1958, p. 361-369.
45. Wassiljewa, A., Theorie der Wärmeleitung in Anwendung auf Gasgemische, Physikalische Zeitschrift 5 Jahrgang, No. 22, 1904, p. 737-742.
46. Bird, R. B., Stewart, W. E., and Lightfoot, E. N., Transport Phenomena, John Wiley and Sons, Inc., New York, New York, 1960.

47. Minkowycz, W. J. and Sparrow, E. M., "Condensation Heat Transfer in the Presence of Non-condensibles, Interfacial Resistance, Superheating, Variable Properties and Diffusion," International Journal of Heat and Mass Transfer, Vol. 9, No. 10, October, 1966, p. 1125-1144.
48. Othmer, D. F., "The Condensation of Steam," Industrial and Engineering Chemistry, Vol. 21, No. 6, June, 1929, p. 576-583.
49. Kroger, D. G. and Rohsenow, W. M., "Condensation Heat Transfer in the Presence of a Non-Condensable Gas," International Journal of Heat and Mass Transfer, Vol. 11, No. 1, January, 1968, p. 15-26.

APPENDIX A

DETERMINATION OF UNBURNED LITHIUM FOR LITHIUM BURNING RATE TESTS

Prior to calculating the lithium burning rate, it was necessary to determine the amount of unburned lithium remaining at the end of a test. Most of the unburned lithium remaining was collected in a cup located below the test sample. The cup was fabricated from a short piece of heavy-walled pipe welded to a piece of plate. The cup was made sufficiently massive to cool the lithium drops quickly, to a temperature below the ignition temperature. In this way, little, or no, lithium was allowed to burn in the cup. The bottom of the chamber was covered with stainless steel sheet to catch any spattered fuel that did not fall into the cup.

After the vacuum chamber had been back-filled with argon, the chamber was opened and the sample removed. The remnants of a test were divided into three general categories: (a) "pure" products, which were discarded, (b) "pure" lithium, and (c) pieces of mixed product and lithium. This procedure was used to reduce potential errors in the wet-test analysis introduced by the presence of the lithium sulfide in the product material. The significance of the presence of the lithium sulfide will be discussed later.

The reactions of interest in the determination of the amount of unburned lithium are as follows:



and



Equation (A.1) represents the reaction which occurs between lithium and water to create a basic solution. Equation (A.2) represents the reaction occurring during the titration analysis. This set of reactions are the only ones needed to analyze the pieces of "pure" lithium found after a test.

The remnants which consisted of mixed products and lithium were treated in a similar manner. However, the presence of lithium sulfide in the product adds one additional reaction which must be considered:



The LiOH produced by this reaction was an obvious source of significant error, depending on the amount of product in the remnants.

Since all the analysis was done at room temperature, a test was performed to determine if the production of lithium hydroxide from the lithium sulfide in the products were sufficiently rapid to require a more complex wet-test analysis than outlined by Equations (A.1) and (A.2). Several samples of products (about one gm) were placed in about 200 ml of distilled water containing phenolphthalien indicator. The solution normally took about one hour (and sometimes longer) before the solution was sufficiently basic to turn uniformly pink. Several more hours were required before any significant depth of color was seen. The first tinge of pink could be made to disappear, and, hence, neutralize the solution, with less than 0.1 ml

of titration solution (about 2.3-2.4 M HCl). One-tenth ml of titration solution was a potential error of less than three percent in the amount of unburned lithium for all the tests. It was concluded that the solid solution formed by the products severely inhibits the rate at which the lithium sulfide could react with the water. The lithium sulfide must be leached out of the solution before it can react, and this process takes some time.

Regardless of the apparently very slow reaction rate of the lithium sulfide contained in the products all the test solutions containing products mixed with the lithium were titrated as quickly as possible (usually within fifteen minutes) to reduce the potential errors introduced by the lithium sulfide. For any one test, if the solutions made from the mixed products and lithium reacting with water were condensed to be made entirely from product, the maximum error in the lithium burning rate calculations would be about 12%, with the average error about 6%. Since this supposes that no lithium was present in these mixtures, and that the product reacted faster than was observed in the test described above, the probable error in the titration analysis was probably about half of the maximum, or about 3-6%. In view of other sources of potential error in the test procedure, it was not deemed justifiable to devote significant effort to separating the products prior to the wet-test analysis.

The amount of unburned lithium remaining after a test was determined as follows:

- (1) The remnants of a test were reacted in three of four beakers containing about 150 ml of distilled water. The extra number of samples were used to prevent an excessive

temperature increase in the water by the heat released by the lithium-water reaction. Keeping the solutions cool also served to slow the rate of the lithium sulfide-water reaction.

- (2) About four drops of phenolphthalien solution in reagent-grade methanol were added to each beaker.
- (3) The solution in each beaker was titrated by a solution of HCL. (about 2.3-2.4 M) until the pink color disappeared.
- (4) The total amount of HCL solution used was measured.
- (5) The amount of unburned lithium was calculated assuming the only reaction occurring was as given by (A.1). Knowing the number of moles of HCL necessary to neutralize the solution yielded the number of moles of lithium which did not burn. Combining this with the amount of lithium originally in the sample and the burning time yielded the average lithium burning rate.

APPENDIX B

EXPERIMENTAL DATA FROM LITHIUM BURNING RATE TESTS

Table 9

Summary of Lithium Burning Rate Tests in Sulfur Hexafluoride

Test	L (mm)	D (mm)	Pressure (Pa)	Wick Temperature (K)	Average Burning Rate (kg/m ² S)
1	30	32	7950	1328	—
3	30	32	8100	1333	.0251
6	30	31	7900	1316	.0245
7	30	32	16350	1394	—
8	30	32	13600	1372	—
9	30	32	10350	1344	—
10	30	32	10750	1350	.0383
11	32	32	5250	1291	.0175
14	32.5	32	10750	1350	.0384
16	31.5	32	13600	1389	.0542
17	30	31	15950	1386	—
34	60	31	10750	1354	.0313
35	59	31	2250	1208	.0124
36	59.5	31	8050	1322	—
38	59	30.5	10750	1377	.0367
42	7.9	31	10750	1358	—
43	13.6	31	10750	1366	—

Table 9 (Continued)

Test	L (mm)	D (mm)	Pressure (Pa)	Wick Temperature (K)	Average Burning Rate (kg/m ² s)
45	29	31	13300	1386	.0574
47	14.2	31	10750	--	--
50	14.5	31.5	10750	1364	.0452
52	16.2	31	10750	--	--
53	15.2	31	10750	1354	.0512
54	16.5	31	10750	1350	--

Table 10

Summary of Lithium Burning Rate Tests in Argon-Sulfur Hexafluoride
Mixtures at a Constant Total Pressure of 13300 Pa

Test	L (mm)	D (mm)	Y_{ae} (%)	Wick Temperature (K)	Average Burning Rate (kg/m ² s)
30	30.5	31	.555	1372	.0267
31	30	30.5	.2755	1380	.0452
39	21	31.5	.4707	1372	.0332
40-a	30.5	30	.668	1380	.0305
46	29	31	.137	--	--
48-a	30.5	30	.583	1369	.0332
49-a	30.5	31	.165	1377	.0452
51	29.7	30	.137	1377	.0427

APPENDIX C

SUMMARY OF DATA OBTAINED DURING WICK-TYPE COMBUSTOR TESTS

Time (min)	Wick Temperature (K)	Combined Pressure (Pa)	Heat Flux (kw/m ²)
Test 3			
20	1078	400	24
22	1078	440	24
24	1079	570	24
26	1081	610	24
28	1086	640	24
30	1093	670	24
32	1110	780	59
34	1125	950	59
36	1137	1010	59
38	1145	1050	59
40	1151	1110	59
42	1158	1210	72
44	1173	1420	72
46	1183	1520	72
56	1080	540	35
58	1080	570	35
60	1080	570	35
62	1080	710	53
64	1085	740	53
66	1096	780	53
68	1103	780	53
70	1107	780	53
72	1109	1050	74
74	1136	1210	74
76	1143	1210	74
78	1144	1180	74
80	1141	1180	74
82	1139	1250	80
84	1146	1320	80
86	1171	1450	93
88	1196	1720	93
Test 4			
6	1101	740	39
8	1121	880	39
10	1132	980	39

Time (min)	Wick Temperature (K)	Combined Pressure (Pa)	Heat Flux (kw/m ²)
---------------	----------------------------	------------------------------	-----------------------------------

Test 4 (Continued)

12	1141	1110	39
14	1149	1280	39
16	1165	1620	39
18	1187	1690	39
20	1198	1920	39
22	1207	2200	47
24	1219	2400	47
26	1224	2700	47
28	1234	2930	47
30	1242	3210	47
32	1249	3480	47
34	1252	3780	47
36	1264	4050	51
38	1271	4350	51
40	1277	4620	48
42	1283	4960	48
44	1285	5260	48
46	1289	5430	54
48	1294	5800	54
50	1298	6110	54

Test 5

8	1112	780	33
10	1115	840	33
12	1122	840	33
14	1129	1010	33
16	1132	1010	33
18	1138	1180	33
20	1142	1180	29
22	1146	1350	29
24	1155	1520	29
26	1159	1520	29
28	1164	1690	29
30	1170	1720	27
32	1172	1790	27
34	1175	1860	27
36	1179	1990	27
38	1180	2020	27
40	1184	2020	27
42	1186	2020	27
44	1190	2160	27
48	1102	1080	29
49	1114	1180	29
50	1123	1350	29
51	1129	1350	29

Time (min)	Wick Temperature (K)	Combined Pressure (Pa)	Heat Flux (kw/m ²)
---------------	----------------------------	------------------------------	-----------------------------------

Test 5 (Continued)

52	1135	1350	29
54	1146	1520	29
56	1155	1650	29
58	1161	1690	29
60	1164	1690	29
62	1203	2030	180
64	1199	2530	180
66	1207	2530	180
68	1207	2560	180
70	1210	2600	180
72	1212	2630	180
74	1215	2700	180
94	1216	2560	169
95	1215	2560	169
96	1216	2560	169
98	1217	2670	169
99	1266	4050	245
100	1275	5230	245
101	1312	5900	245
102	1317	6380	241
103	1320	6680	241
104	1324	6820	238

Test 6

15	1124	1620	32
15.5	1135	1690	32
16	1147	1720	32
16.5	1156	1760	32
17	1162	1860	32
17.5	1166	1920	32
18	1175	1960	32
20.5	1111	1350	32
21	1124	1620	32
21.5	1135	1690	32
22	1147	1760	32
22.5	1156	1790	32
23	1159	1920	32

Test 7

3.5	1160	1690	30
5.0	1171	1790	30
6.5	1179	1960	30
8.0	1190	2020	30
9.5	1199	2230	30
11.0	1207	2450	30

Time (min)	Wick Temperature (K)	Combined Pressure (Pa)	Heat Flux (kw/m ²)
---------------	----------------------------	------------------------------	-----------------------------------

Test 7 (Continued)

12.5	1215	2630	30
14.0	1221	2730	30
15.5	1224	2870	30
17.0	1226	3000	30
18.5	1229	3140	30
20.0	1232	3270	30
21.5	1242	3610	36
23.0	1255	4150	36
24.5	1266	4760	36
26.0	1274	5230	36
27.5	1268	4860	28
29.0	1262	4690	28
30.5	1259	4520	28
32.0	1256	4420	28
33.5	1254	4350	28
35.0	1254	4290	28
36.5	1254	4290	28
38.0	1251	4250	28
39.5	1251	4220	28
41.0	1270	4960	36
42.5	1277	5640	36
44.0	1294	6380	36
45.5	1305	7020	36

Test 10

2	1082	660	19
4	1138	1000	19
6	1186	1620	19
8	1199	1970	19
10	1208	2260	19
12	1254	5180	112
14	1239	4220	112
16	1246	4520	112
18	1256	4940	112
20	1252	4850	103
22	1252	4810	103
24	1252	4850	103
26	1254	4920	103
28	1255	4980	103
30	1257	5050	103
32	1257	5150	103
34	1258	5210	103
36	1260	5420	103
38	1261	5550	103

Time (min)	Wick Temperature (K)	Combined Pressure (Pa)	Heat Flux (kw/m ²)
Test 13			
40	1066	410	6
80	1111	730	15
85	1119	730	18
90	1125	770	18
95	1130	810	18
100	1136	930	18
110	1151	1200	18
115	1161	1330	18
120	1169	1530	18

Distribution and Addressee Listing

<u>Addressee</u>	<u>Copies</u>
Director Advanced Research Projects Agency Architect Building 1400 Wilson Blvd. Arlington, VA 22209	3/0
Officer in Charge David W. Taylor Naval Ship Research and Development Center Annapolis Laboratory Annapolis, Maryland 21402 Attn: Mr. S. Cox, Code 2724	9/1
CDR C. E. Moore, OPNAV 233 Chief of Naval Operations, Off of the Room 5E577 Pentagon Washington, D.C. 20301	1/0
TACTEC Battelle Columbus Laboratories 505 King Avenue Columbus, Ohio 43201	1/0
Dr. Eugene C. Gritton The Rand Corporation 1700 Main Street Santa Monica, CA 90406	5/0